Computationally exploring ultrafast molecular ionization

by

Youliang Yu

B.S., Nanjing Normal University, China, 2011

_____

AN ABSTRACT OF A DISSERTATION

submitted in partial fulfillment of the requirements for the degree

DOCTOR OF PHILOSOPHY

Department of Physics
College of Arts and Sciences

KANSAS STATE UNIVERSITY
Manhattan, Kansas

2018

Abstract

Strong-field ionization plays a central role in molecules interacting with an intense laser field since it is an essential step in high-order harmonic generation thus in attosecond pulse generation and serving as a probe for molecular dynamics through either the sensitivity of ionization to the internuclear separation or the laser-induced electron scattering. Strong-field molecular ionization has been studied both theoretically and experimentally, dominantly through the Born-Oppenheimer approximation and at equilibrium or small reaction distances. We have extended the theoretical studies of molecular ionization to a much broader extent. Specifically, due to the difficulty of treating ionization in Born-Oppenheimer representation especially for molecular dynamics involving strongly-correlated electron-nuclear motion, we have investigated an alternative time-independent — adiabatic hyperspherical — picture for a one-dimensional model of the hydrogen molecule. In the adiabatic hyperspherical representation, all the reaction channels — including ionization — for the hydrogen molecule have been identified in a single set of potential curves, showing the advantage of studying molecular dynamics involving multiple breakup channels coupled with each other. We have thus proposed a good candidate to study strongly-correlated molecular dynamics, such as autoionization and dissociative recombination. Moving to a time-dependent picture by numerically solving the time-dependent Schrdinger equation (TDSE), we have explored two extreme classes of strong-field ionization of hydrogen molecule ion: at large internuclear distance ($R > 30$ a.u.) and for long-wavelength laser fields. Remarkably, we have found strong-field two-center effects in molecular ionization beyond the long-standing one-photon two-center interference as a manifestation of the double-slit interference. In particular, the total ionization probability at large internuclear distances shows strongly symmetry-dependent two-center dynamics in homonuclear diatomic molecules and two-center induced carrier-envelope phase effect in heteronuclear diatomic molecules. Such two-center effects are expected to generalize to other diatomic systems and could potentially be used to explain phenomena in multi-center strong-field physics. Moreover, we have theoretically confirmed, for the first time, the existence of low energy structure in molecular ionization in long-wavelength laser fields by solving the three-dimensional TDSE. Finally, we have performed a pump-probe study of the hydrogen molecular ion where a pump pulse first dissociates the molecule followed by a probe pulse which ionizes the dissociating wave packet, and surprisingly found a pronounced broad ionization peak at large R or large pump-probe delay ($\sim$150 fs). Numerically, we have developed and implemented new theoretical frameworks to more accurately and efficiently calculate quantum mechanical processes for small molecules — hydrogen molecule and its ion — which could readily be adapted to heavier diatomic systems.

Computationally exploring ultrafast molecular ionization

by

Youliang Yu

B.S., Nanjing Normal University, China, 2011

———————————

A DISSERTATION

submitted in partial fulfillment of the requirements for the degree

DOCTOR OF PHILOSOPHY

Department of Physics
College of Arts and Sciences

KANSAS STATE UNIVERSITY
Manhattan, Kansas

2018

Approved by:

Major Professor
Brett D. Esry

Copyright

Abstract

Strong-field ionization plays a central role in molecules interacting with an intense laser field since it is an essential step in high-order harmonic generation thus in attosecond pulse generation and serving as a probe for molecular dynamics through either the sensitivity of ionization to the internuclear separation or the laser-induced electron scattering. Strong-field molecular ionization has been studied both theoretically and experimentally, dominantly through the Born-Oppenheimer approximation and at equilibrium or small reaction distances. We have extended the theoretical studies of molecular ionization to a much broader extent. Specifically, due to the difficulty of treating ionization in Born-Oppenheimer representation especially for molecular dynamics involving strongly-correlated electron-nuclear motion, we have investigated an alternative time-independent — adiabatic hyperspherical — picture for a one-dimensional model of the hydrogen molecule. In the adiabatic hyperspherical representation, all the reaction channels — including ionization — for the hydrogen molecule have been identified in a single set of potential curves, showing the advantage of studying molecular dynamics involving multiple breakup channels coupled with each other. We have thus proposed a good candidate to study strongly-correlated molecular dynamics, such as autoionization and dissociative recombination. Moving to a time-dependent picture by numerically solving the time-dependent Schrdinger equation (TDSE), we have explored two extreme classes of strong-field ionization of hydrogen molecule ion: at large internuclear distance ($R>30$ a.u.) and for long-wavelength laser fields. Remarkably, we have found strong-field two-center effects in molecular ionization beyond the long-standing one-photon two-center interference as a manifestation of the double-slit interference. In particular, the total ionization probability at large internuclear distances shows strongly symmetry-dependent two-center dynamics in homonuclear diatomic molecules and two-center induced carrier-envelope phase effect in heteronuclear diatomic molecules. Such two-center effects are expected to generalize to other diatomic systems and could potentially be used to explain phenomena in multi-center strong-field physics. Moreover, we have theoretically confirmed, for the first time, the existence of low energy structure in molecular ionization in long-wavelength laser fields by solving the three-dimensional TDSE. Finally, we have performed a pump-probe study of the hydrogen molecular ion where a pump pulse first dissociates the molecule followed by a probe pulse which ionizes the dissociating wave packet, and surprisingly found a pronounced broad ionization peak at large R or large pump-probe delay ($\sim$150 fs). Numerically, we have developed and implemented new theoretical frameworks to more accurately and efficiently calculate quantum mechanical processes for small molecules — hydrogen molecule and its ion — which could readily be adapted to heavier diatomic systems.

Table of Contents

List of Figures

List of Tables

Acknowledgments

First and foremost I would like to sincerely thank my advisor Dr. Brett Esry for his patient guidance. I would not have gone this far without his encouragement and stimulation. It has been a great experience to work with him, not only because of his expert knowledge in atomic, molecular, and optical physics but also because he is a very open-minded person and has always been supportive during my PhD studies. His rigorous attitude to research, sharp advices to obscure physical and numerical details, creative and critical thinking have always been inspiring and deeply influenced my mindset. Brett has been a great mentor for me and will for sure positively impact my future career.

During my time in Brett's research group, I have been greatly benefited from other members. I am grateful to Dr. Yujun Wang, who like my big brother guided me on various projects at the early stage of my PhD studies. The discussions we had have always been constructive and helped me resolve various challenging questions, both physically and numerically. I would like to thank Dr. Nicolais Guevara who gave me a detailed introduction to the three-body B-splines code which has accelerated my early studies. I would like to acknowledge Dr. Christian Madsen for valuable discussions on the project of one-dimensional H_2. I also want to acknowledge Dr. Greg Armstrong for providing details of the time-independent two-center spheroidal code, which I adapted to solve the ionization problem of hydrogen molecular ion. The collaboration we had on the molecular two-center effects has been a pleasure. A special thank goes to Dr. Shuo Zeng, who helped me a lot in many detailed aspects, in research or in life, during our four-year overlap. Thanks to Dustin Ursrey for reading my thesis and providing helpful suggestions. I also want to thank all other members: Dr. Jens Svensmark, Dr. Edmund Meyer, Brandon Rigsbee, Russ Averin for all the discussions from physics to basically everything during our countless group meetings.

I would like to acknowledge my collaborators on the experimental side: Dr. Itzik Ben-Itzhak and his group. Part of my work was originated from experiments. Informative discussions we had in our theory-experiment joint meetings have largely benefited my research.

Thanks to my teachers: Dr. Chi-Dong Lin, Dr. Andrew Ivanov, Dr. Uwe Thumm for those informative classes which built the foundation for my research thereafter. I am also grateful to Larry McFeeters and other PCSC staff for providing in-time supports on computer technical issues so that I can focus on physics.

Last but certainly not the least, I would like to express my deep gratitude to my family for their unconditionally supports throughout my PhD study. I owe them more than thanks. In particular, I want to thank my wife, Haoyu Zhang, for standing beside me throughout my PhD study. She has been my motivation and inspiration to continue to improve my knowledge and my career. I also want to thank my parents for always being there whenever I need them.

Dedication

To my loving wife and my dear parents.

Chapter 1

Introduction

Over the last three decades, as laser technology and fragment imaging techniques flourished, interactions of atoms and molecules with short, intense laser pulses have been an active and growing area of research. One reason is that electrons in atoms and molecules are typically driven by a force induced by the electric field of laser pulses that can easily compete against the binding force from the system itself, thus triggering complicated electronic dynamics such as the widely-known above threshold ionization [1–3]. Strong-field molecular ionization, due to its intrinsic multi-center nature, has shown various intriguing dynamical phenomena, such as enhanced ionization at critical internuclear distances [4, 5], suppressed ionization for some molecules [6, 7], sensitivity of the ionization to molecular orbitals [8–10], and interference effects in molecular high-order harmonic generation (HHG) [11, 12]. These phenomena have made molecular ionization a revealing probe for electronic and nuclear dynamics in strong-field processes, therefore providing a means to control molecular dynamics, and ultimately to control chemical reactions.

To theoretically describe such highly nonperturbative processes in a fully quantitative manner, the best option is to numerically solve the time-dependent Schrödinger equation (TDSE). Although there are a number of notable approximate treatments, such the strong-field approximation (SFA) [13–15], Keldysh-Faisal-Reiss (KFR) theory [16–18], and molecular ADK [19], the TDSE is still a gold standard to which they are compared. Solving the multi-dimensional TDSE, however, is typically challenging and unfavorably time-consuming. Fortunately, due to the advances of the modern high-performance computing architecture and the development of computational methods, the contradiction between numerical accuracy and demanding computational resources is being reconciled. Nowadays, due to rising interests in circular and elliptical polarized light and their interactions with atoms and molecules, people start to solve three-dimensional (3D) TDSE involving strong fields within the single-active-electron (SAE) approximation, which typically reduces to 3D or — more commonly — coupled-2D differential equations. For molecular ionizations in this case, the nuclei are normally fixed at equilibrium or small internuclear distances, thus computationally reducing the molecular ionization to the atomic ionization. However, at large internuclear distances in molecular ionization, the multi-center Coulomb singularities might cause numerical problems, which could be either in solving the TDSE or analyzing the wave

function. Thus special care needs to be taken. For strong-field ionization beyond the SAE approximation, there are many attempts [20–27] at solving the full-dimensional TDSE for helium — the simplest multi-electron system — which in principle is a six dimensional problem except it reduces to coupled-2D differential equations after expanding the electronic wave function into coupled spheroidal harmonics bases. Most of these works [20–22, 24–26], however, focus on the perturbative or few-photon regimes. When it comes to strong field, the number of partial waves exponentially increases therefore making the calculation nearly unfeasible. To our knowledge, such strong-field (800 nm, 10^{14} W/cm^2) multi-electron ionization can only be done either through a huge amount of computational resources, which is about a factor of 1000 heavier than a perturbative calculation for a 40 nm XUV pulse with the same accuracy [23] — or by sacrificing accuracy of observables [27].

Molecular hydrogen (H$_2$) and its isotopes(HD/D$_2$) or ions (H$_2^+$/HD$^+$/D$_2^+$) as benchmark systems, have been extensively studied both theoretically and experimentally [28–38], due to their significant roles in understanding ultrafast molecular dynamics. Such benchmark systems will be our focus in this dissertation.

1.1 One-dimensional H$_2$ in adiabatic hyperspherical representation

In studies of dissociative ionization of H$_2$ in ultrafast laser field, a multi-step Born-Oppenheimer (BO) picture is often used to understand the dynamics. The first step is ionization. From the H$_2$ ground state, the H$_2^+$ nuclear wavepacket is created as a coherent superposition of H$_2^+$ vibrational states or as an incoherent Franck-Condon distribution of the vibrational levels. This picture is based on the fact that ionization occurs on a time scale much shorter than that of the nuclear vibrations, thus an instantaneous electronic transition occurs between the H$_2$ ground state and the H$_2^+$ vibrational levels. In such a picture, electronic correlations are neglected in the first ionization step, which is necessary due to the difficulties of treating ionization in BO representation. Recently, however, as ultrashort laser pulses become available on the electronic (sub-femtosecond) timescales, the electronic correlations have been found to be significant in electronic dynamics. For instance, G. Sansone *et al.* [33] and A. Fischer *et al.* [34] found that doubly excited states cause a coherent superposition of two different pathways, which leads to asymmetric ejection of the ionic fragment in the dissociative ionization of H$_2$. So, to fully understand molecular dynamics, one needs to go beyond the Born-Oppenheimer approximation.

The hyperspherical coordinates, since first introduced to study atomic problems in the late 1950s [39], have been widely used in atomic and molecular physics [40–59]. In atomic physics, for instance, the electronic correlations and doubly excited states for He atom and H$^-$ ion have been successfully described in the adiabatic hyperspherical representation [40, 41, 45, 49]. In molecular physics, the hyperspherical approach has been applied to study molecular vibrations (see Ref. [48] for example) and various scattering processes [47, 56] for three-body systems. In the field of ultracold collisions, the adiabatic hyperspherical representation has been particularly successful in studies of three-body recombination [54,

55, 60] and Efimov physics [50, 61–63].

Although the adiabatic hyperspherical representation has been proven very useful, it has not yet been applied to the electronic and nuclear degrees of freedom for molecules more complicated than H_2^+ [43, 64]. In Chapter 2, we will present such calculations for the first time for a one-dimensional (1D) model of H_2. This model, however, is chosen to exactly reproduce the three-dimensional (3D) H_2 and H_2^+ ground Born-Oppenheimer (BO) potentials. We, therefore, expect the calculations to reproduce quantities like ionization thresholds, nuclear vibrational energies, and to give — at least — qualitative predictions for relevant observables, such as the ATI spectrum. Since recent studies [33, 34] have shown the significance of doubly excited states in strong-field and attosecond processes, one of our goals here is to identify and understand doubly-excited states [29, 30] in the adiabatic hyperspherical representation. We also want to take advantage of the fact that the adiabatic hyperspherical representation produces well defined and uniquely discretized effective potentials in the ionization channels to help understand processes such as weak-field dissociative ionization.

1.2 Strong-field two-center effects in diatomic molecular ionization

Since the prediction of molecular two-center interference by Howard Cohen and Ugo Fano [65] in 1966, a considerable amount of theoretical and experimental effort [66–76] has been dedicated to the molecular double-slit interference. Resembling Young's double-slit experiments, which is regarded as the simplest manifestation of the wave nature of particles, the molecular double-slit is further intertwined with the fundamental characteristics of quantum mechanics in the microscopic length scale, such as quantum coherence.

In molecular double-slit experiments, to observe the interference pattern — in the photo-electron spectrum — the internuclear distance must be comparable to the central wavelength of the electronic wavepacket, as is similar in classical Young's double-slit experiments. The distinction, however, arises from the fact that in molecular double-slit, the electronic wave packet emitted from one center could interfere with the wavepacket emitted from the other center or it could interact with the other nuclei with assistance from the laser field, producing two-center interference or two-center dynamics thus leading to complications in observables. Molecular double-slit interferences, however, have been directly or indirectly seen in measurements for the smallest diatomic molecule—H_2 [66, 68, 69, 71]—and for heavier systems [67, 70, 72, 74, 76], providing explanations for emerging phenomena in photoelectron spectroscopy.

Cohen and Fano's theory [65] predicts interference pattern for the photoelectron spectrum in photoionization of homonuclear diatomic molecules. However, for the integral quantity—the total ionization yield—it predicts no interference pattern. Given that Cohen and Fano's theory effectively assumes one-photon processes, one might question what happens if the photoionization moves to the multiphoton or tunneling regime? Does two-center effect play a role in the total ionization yield?

Previously, studies of diatomic molecular ionization revealed that the ionization probability could be surprisingly enhanced at critical distances [4, 5]. Such sensitivity of molecular ionization to the internuclear distance (R) stimulates a series of studies on the time-resolved molecular fragmentation and ionization [77–81]. It even provides an explanation for experimental discoveries in atomic clusters [82], suggesting phenomena discovered in small molecules do affect dynamics in large systems. Despite these, almost all previous studies focus on the molecular ionization around equilibrium or critical distance. There is essentially no investigation on strong-field ionization for diatomic molecules at large R(>30 a.u.). One reason is the non-triviality of the exact *ab initio* calculations due to the Coulomb singularity at the nuclei. More importantly, such a regime of R is conceptually neglected. Normally, one would expect the molecular ionization to reduce to the atomic ionization at such large R, with no interesting molecular physics involved.

In Chapter 3, we will present, for the first time, the study of strong-field molecular ionization at large internuclear distances. The H_2^+, as a benchmark system, is chosen in this study due to its simplicity for understanding in both theory and experiments. We focus on the total ionization probability at large R where the Cohen and Fano's theory [65] predicts no two-center effects. Surprisingly, we find the strong-field two-center effects in molecular ionization beyond the one-photon two-center interference. Furthermore, to deepen our understanding, we examine the low energy photoelectron spectrum as a function of large R and observe a clear interference pattern. We do expect that the molecular two-center effects presented here will generalize to other diatomic molecules and could potentially be used to explain phenomena in multi-center physics. Additionally, to understand how the strong-field two-center effects behave in practical experiments, in Chapter 5, we will present a pump-probe study of dissociative ionization of full-dimensional H_2^+/HD^+, where a pump pulse first dissociates the molecule followed by a probe pulse which ionizes the dissociating wavepacket. The strong-field two center effects at large R are thus convoluted to the large pump-probe delay.

1.3 Low energy structure in strong-field ionization

Atoms and molecules exposed to an intense laser field might absorb a number of photons larger than required to ionize the electron, thus showing the photoelectron energy distribution with peaks separated by one photon energy. This so-called above-threshold ionization (ATI) was first measured in 1979 [1]. Since then, extensive theoretical and experimental studies have revealed various features of the ATI spectrum, e.g. plateau and cut-offs [83, 84], and carrier-envelope phase dependence of the ATI spectrum. (See, for example, Refs. [2, 3] for reviews.) More recently, a pronounced low energy structure (LES) — peak-like structure at low energy in the ATI spectrum — was reported by Blaga et al. [85]. Such unexpected LES, however, could not be reproduced by the widely-used SFA, which has been successful in qualitatively predicting high-energy ATI and HHG spectra [2, 3, 15]. Given that the SFA neglects the effect of the ion core of the system on the photoelectron, one would expect effects of the Coulomb potential to play a role in LES. Moreover, the LES cannot

be reproduced with a circularly polarized pulse [85], showing the LES is a laser ellipticity-dependent phenomenon. Even though the atomic LES has been extensively studied both theoretically and experimentally, theoretical studies of molecular LES — especially through *ab initio* calculations — are rare.

1.4 Prologue for the work relavant to this dissertation

Before presenting our work for ionization-related studies in diatomic molecules, I will summarize the contributions I made during my Ph.D. studies.

- Numerical computation

  I have implemented or adapted various numerical methods to solve the Schrödinger equation. The work of one-dimensional (1D) H_2 in adiabatical hyperspherical representation was done in the B-splines representation (see Appendix C.1 for details) where large banded matrices in the eigenvalue problem were diagonalized using the `ARPACK` package [86], which is based on the Lanczos algorithm [87]. In studies of photoionization of three-dimensional (3D) H_2^+, I implemented an iterative short-time propagator for solving the TDSE, where the exponentials were evaluated via a Padé approximation and a sparse-direct method called `PARDISO` [88] was used for the linear solve. The calculations of dissociative ionization of 1D H_2^+ were performed in the finite elements discrete variable representation (FEDVR, see Appendix C.2 for details) where exponential terms in the short-time propagator were evaluated with the Lanczos algorithm [89]. The solutions of the Schrödinger equation were analyzed by projecting them to the energy-normalized scattering states which were solved using the eigenchannel R-matrix method [90]. The results of these works will be discussed in details in the following chapters and can be found in my following works [91–94]. Among these studies, I have distributed large-scale computations up to 50,000 CPU hours to calculate the adiabatic hyperspherical potentials for 1D H_2 and the ionization probability for 3D H_2^+. In studies of 1D H_2, I have performed hundreds of calculations to resolve — sharp — avoided crossings and all the reaction channels with each calculation compromised of a non-trivial eigenvalue problem for a 2D differential equation. In studies of the ionization of H_2^+, the majority of the computational effort was used to do hundreds of linear solve for a 2D differential equation compromised of large matrices due to extremely large internuclear distances. The numerical details will be discussed in Sec. 2.1.4 and Sec. 3.1.5.

- Structure of 1D H_2.

  We studied the molecular structure of the 1D H_2 in an alternative adiabatic representation other than the widely-used Born-Oppenheimer. In the adiabatic hyperspherical picture, we have identified all the breakup channels in a single picture, making it intrinsically convenient for studying molecular dynamics in 1D H_2. The details will be presented in Chapter 2.

- Photoionization of 3D H_2^+.

  We studied the photoionization of three-dimensional H_2^+ with nuclei fixed, where we developed and implemented a sparse-direct TDSE solver in prolate spheroidal coordinates using the B-splines representation. This work could generalize to other two-center systems within the single-active electron framework. To obtain the momentum and energy distribution, we developed a formalism to solve for the two-center scattering states for a single active electron in prolate spheroidal coordinates. They will be presented in Chapter 3 and 5 and in my following work [92].

- Photodissociation of full-dimensional H_2^+.

  We have investigated the influence of the initial nuclear angular distribution on strong-field molecular dissociation. Specifically, we examined the dependence of the final angular distribution, the kinetic energy release spectrum, and the total dissociation yield on the initial nuclear angular distribution. Numerically, we took advantage of the linearity of the TDSE by solving it for individual initial angular momentum states independently and superposing the final states with coefficients defined by the initial molecular alignment. This way calculations could be perfectly parallelizable. Similar studies of photodissociation of H_2^+ can be found in my works [95]

- Dissociative ionization of 1D H_2^+.

  In a one dimensional model of H_2^+ with both electronic and nuclear motions included, we have studied the electron-nuclear correlation and coherence by examing the energy sharing between the two. The multiphoton electronic-nuclear coherence can be attributed to the energy-space overlap of the wavepackets generated from each half cycle. Additionally, we have found that increasing the laser intensity and wavelength complicates the electronic-nuclear correlation. They will be presented in my following work [94].

- Complex absorbing potentials.

  To handle the boundary reflection and increase the efficiency in solving the TDSE, we have developed optimized, yet general, complex absorbing potentials (CAP) for ultrafast, strong-field problems, where a factor of 3–4 reductions in absorption range was achieved, compared to other widely used CAPs. They will be presented in Chapter 6 and can be found in my following work [96].

- Studies generalizable to different systems and to predict experiments.

  The methods we used in ionization of hydrogen molecular ion can be readily generalized to other two-center systems, e.g. a diatomic system with short-range potentials, as will be discussed in Sec. 3.2.1. Our theoretical work can be appropriately adapted to predict practical experiments, as will be discussed in Chapter 5.

Chapter 2

One-dimensional hydrogen molecule in adiabatic hyperspherical representation

2.1 Theory

To solve the four-body Schrödinger equation for one-dimensional H_2 in the adiabatic hyperspherical representation, the first and also the most important step is to solve the adiabatic equation. Specifically, we calculate the eigenfunctions and eigenvalues of the adiabatic Hamiltonian in order to extract information about doubly excited states and ionization for 1D H_2.

2.1.1 Hyperspherical coordinates

In hyperspherical coordinates, one coordinate called the hyperradius is in units of distance and all other coordinates are angles or so-called hyperangles [51–53]. The hyperradius, which is treated as an adiabatic parameter in the adiabatic hyperspherical representation, controls the overall size of the system. The hyperangles can be defined by spatial angles, relative distance, and momentum of inertia. For 1D H_2, four aligned particles can be described by four coordinates. One of them is for the center of mass motion. The remaining three internal coordinates can be represented by the hyperradius R and two hyperangles θ and ϕ. The effect of the permutation operations on the hyperangles depends critically on the choice of the Jacobi vectors. To connect two pairs of identical particles directly by a Jacobi vector so that the permutation operators become simple, we choose the "H"-type Jacobi vectors $(\vec{\rho}_N, \vec{\rho}_e, \vec{\rho})$. As illustrated in Fig. 2.1, coordinate ρ_N is the inter-nuclear displacement, ρ_e is the inter-electronic displacement, and ρ is the displacement between the center of nuclei and the center of electrons. In 1D, they can be positive or negative.

The hyperspherical coordinates (R, θ, ϕ), which maps on to three-dimensional (3D)
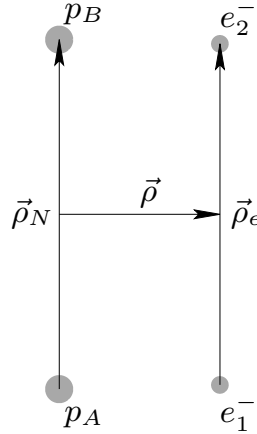
Figure 2.1: *Solid arrows ($\vec{\rho}_N$, $\vec{\rho}_e$, $\vec{\rho}$) are "H"-type Jacobi vectors for our 1D H$_2$ system. Two of them connect pairs of identical particles, the other one starts from the nuclear center of mass and ends at the electronic center of mass. All coordinates associated with these vectors can be positive or negative.*

spherical coordinates, for 1D H$_2$ are defined as

$$\sqrt{\frac{\mu_e}{\mu}}\rho_e = R\sin\theta\sin\phi$$

$$\sqrt{\frac{\mu_N}{\mu}}\rho_N = R\sin\theta\cos\phi$$

$$\sqrt{\frac{\mu_\rho}{\mu}}\rho = R\cos\theta \tag{2.1}$$

where μ_N, μ_e and μ_ρ are reduced masses for the three corresponding coordinates, defined as $\mu_N = m_N/2$, $\mu_e = m_e/2$, $\mu_\rho = 2m_N m_e/(m_N+m_e)$ (m_e is the mass of the electron, m_N is the mass of a proton), and the four-body reduced mass μ is an arbitrary scaling factor which we choose to be μ_N for the convenience of comparing adiabatic hyperspherical potentials to BO potentials. The hyperangle θ ranges from 0 to π, and ϕ from 0 to 2π.

2.1.2 Time-dependent Schrödinger equation

We write the Schrödinger equation in terms of the scaled wave function $\Psi(R,\theta,\phi)$, which is related to the unscaled solution $\psi(R,\theta,\phi)$ by $\Psi(R,\theta,\phi) = R\psi(R,\theta,\phi)$. The volume element for the scaled wave function is $dR\sin\theta d\theta d\phi$. The Schrödinger equation for 1D H$_2$ is written as (atomic units are used throughout)

$$i\frac{\partial}{\partial t}\Psi = [H_0 - \boldsymbol{d} \cdot \boldsymbol{\mathcal{E}}(t)]\Psi \tag{2.2}$$

with the dipole operator $\boldsymbol{d}$ and laser field $\boldsymbol{\mathcal{E}}(t)$, where we use dipole approximation in the length gauge. The field-free Hamiltonian is

$$H_0 = -\frac{1}{2\mu}\frac{\partial^2}{\partial R^2} + H_{\text{ad}} \tag{2.3}$$

$$H_{\text{ad}} = \frac{\Lambda^2}{2\mu R^2} + V(R, \theta, \phi)$$

where Λ^2 denotes the grand angular momentum operator [49]

$$\Lambda^2 = -\left[\frac{1}{\sin\theta}\frac{\partial}{\partial\theta}\left(\sin\theta\frac{\partial}{\partial\theta}\right) + \frac{1}{\sin^2\theta}\frac{\partial^2}{\partial\phi^2}\right] \tag{2.4}$$

and $V(R, \theta, \phi) = V$ is the Coulomb interaction between all particles

$$V = \frac{1}{|\rho_N|} + \frac{1}{\sqrt{\rho_e{}^2 + b^2(\rho_N)}} + V_1 + V_2 \tag{2.5}$$

with

$$V_i = -\frac{1}{\sqrt{r_{Ai}^2 + a^2(\rho_N)}} - \frac{1}{\sqrt{r_{Bi}^2 + a^2(\rho_N)}}, \; i = 1, 2 \tag{2.6}$$

where r_{Ai}, r_{Bi} are inter-particle distance between nuclei and electrons, and a, b are softcore parameters. The soft-core parameters $a(\rho_N)$ [97] and $b(\rho_N)$ vary with the internuclear distance $|\rho_N|$ in our calculations (see Fig. 2.2). We adjust soft-core parameter $a(\rho_N)$ to reproduce the 3D $1s\sigma_g$ BO potential of H_2^+ and adjust $b(\rho_N)$ to reproduce the 3D $X^1\Sigma_g^+$ BO potential of H_2. By doing this, we can extract energetic information from these potentials quantitatively, such as the nuclear vibrational levels and the single ionization threshold. Using soft-core potentials avoids numerical difficulties and unphysical collapse caused by Coulomb singularities in 1D. In addition, it allows the electrons to bypass the nuclei, as is allowed in 3D.

In the adiabatic hyperspherical representation, the total wave function $\Psi(R, \theta, \phi, t)$ is rigorously represented in the adiabatic basis as

$$\Psi = \sum_\nu F_\nu(R, t)\Phi_\nu(R; \theta, \phi), \tag{2.7}$$

where $F_\nu(R, t)$ is the time-dependent hyperradial wave function, and the orthogonal adiabatic basis $\Phi_\nu(R; \theta, \phi)$ together with the adiabatic potentials $U_\nu(R)$ are obtained by fixing
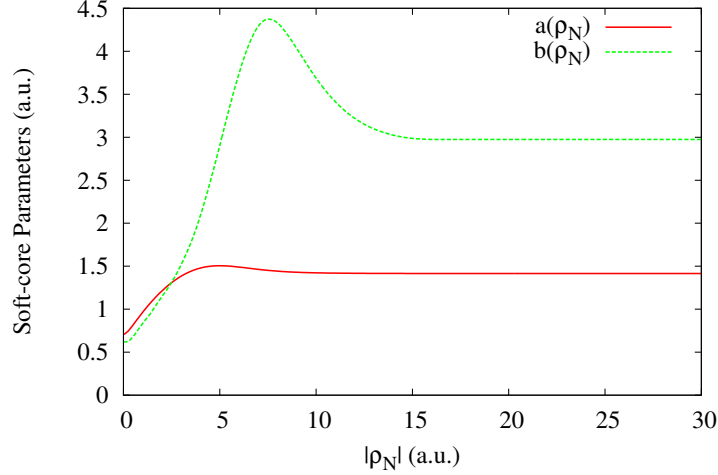
Figure 2.2: *Parameters $a(\rho_N)$ and $b(\rho_N)$ used in the model Coulomb potentials [Eq. (2.5)] are shown. (see text for details)*

R and solving the adiabatic eigenvalue equation

$$H_{\text{ad}}\Phi_\nu\left(R;\theta,\phi\right) = U_\nu\left(R\right)\Phi_\nu\left(R;\theta,\phi\right). \tag{2.8}$$

Substituting Eq. (2.7) into Eq. (2.2), the Schrödinger equation reduces to a set of coupled 1D equations

$$\left(-\frac{1}{2\mu}\frac{d^2}{dR^2} + U_\nu\right)F_\nu(R,t)$$
$$-\sum_{\nu'}\left[\frac{1}{2\mu}\left(P_{\nu\nu'}\frac{d}{dR} + \frac{d}{dR}P_{\nu\nu'} + Q_{\nu\nu'}\right) - \boldsymbol{\mathcal{E}}(t)\cdot < \Phi_\nu|\boldsymbol{d}|\Phi_{\nu'} > \right]F_{\nu'}(R,t) = i\frac{\partial}{\partial t}F_\nu(R,t) \tag{2.9}$$

where P and Q are matrices of non-adiabatic couplings [59]. Since the dynamics of a system are often primarily determined by the adiabatic potentials U, we will focus our following discussions on these potentials only.

2.1.3 Symmetries

It's useful at this point to describe symmetries for the four-body system. We notice that the hyperradius is invariant under identical particle permutations and total parity operation. Thereby all these symmetries can be carried by the hyperangles. Since these symmetries are often associated with the symmetry properties of the interaction potentials, we show the coalescence lines (with zero distance) in the $\theta - \phi$ plane in Fig. 2.3. The potentials around the straight coalescence lines are repulsive whereas those around the curves are attractive.

10
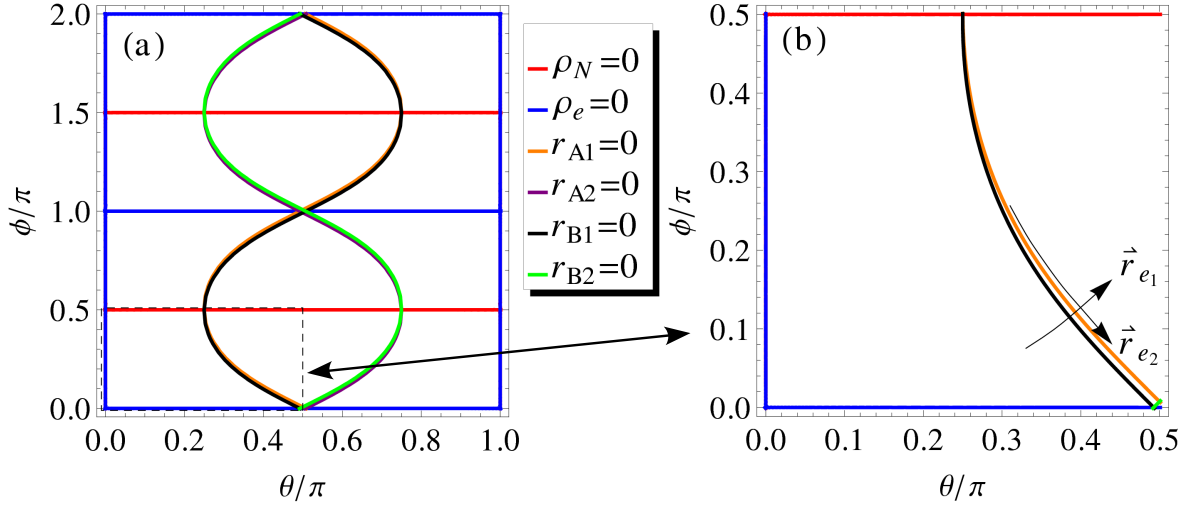
Figure 2.3: *The coalescence lines for the potentials in the hyperangular space with fixed hyperradius. (see text for details)*

Table 2.1: *Table with boundary conditions (BC) and symmetry operators.*

operators	BC(symmetric)	BC(anti-symmetric)
P_N	$\left.\frac{\partial \Phi}{\partial \phi}\right|_{\phi=\frac{\pi}{2}} = 0$	$\Phi(\phi = \frac{\pi}{2}) = 0$
P_e	$\left.\frac{\partial \Phi}{\partial \phi}\right|_{\phi=0} = 0$	$\Phi(\phi = 0) = 0$
$\Pi \cdot P_N \cdot P_e$	$\left.\frac{\partial \Phi}{\partial \theta}\right|_{\theta=\frac{\pi}{2}} = 0$	$\Phi(\theta = \frac{\pi}{2}) = 0$

One can notice that Fig. 2.3(a) can be symmetrically reduced to one eighth of the whole space, which is inherently due to the symmetries of the two-electron, two-proton system. These symmetries correspond to the conserved quantities including permutation symmetries (P_N, P_e) and total parity (Π). For singlet/triplet nuclear spin (I), the wave function is symmetric/anti-symmetric with respect to $\phi = \pi/2$, and for singlet/triplet electronic spin (S), the wave function is symmetric/anti-symmetric with respect to $\phi = 0$. The symmetry with respect to $\theta = \pi/2$ is the result of the product of three symmetry operators, $P_N \cdot P_e \cdot \Pi$. See Table 2.1 for boundary conditions and the corresponding symmetry operators. We then reduce the range of the hyperangles to one octant of the whole space, indicated by dashed line in Fig. 2.3(a), and do calculations with less computational effort.

In general, the channel functions Φ_ν usually contain the majority of the physical characteristics in the total wave function. We thus can use them to obtain qualitative information before doing time-consuming time-dependent calculations that also involve the hyperradial motion. In the work, we solve Eq. (2.8) for singlet nuclear spin ($I = 0$), singlet electronic spin ($S = 0$), and even/odd parity ($\Pi = +1/-1$), which is the focus of this chapter.

11

2.1.4 Numerical discussion

We use the basis splines (B-splines) method to solve Eq. (2.8). The B-splines method expresses an unknown wave function as a linear combination of locally defined polynomials. (See Appendix C.1 for more details.) In our calculation,we use about 900 B-splines in ϕ-direction and about 600 B-splines in θ-direction at $R = 20$ a.u. for solving Eq. (2.8) for up to 200 states. The B-spline number, peak memory and cpu hours all roughly scale linearly with the value of R. The resulting adiabatic hyperspherical potentials are converged to more than 6 significant digits for 200 states in the range of R from 0.55 to 20 a.u.. Here we use the `ARPACK` subroutine [86] to solve the eigenvalue problem in the adiabatic equation, which is efficient enough when we diagonalize small matrices, such as those with 100 or smaller B-spline numbers. However, since we apply the direct product basis to construct the channel function, each sub-matrix within the big matrix is still banded. So in practice, the big banded matrix that we solve still carries large number of zeros. In this case, the sparse matrix method should be a better choice, where we expect a factor of 3 or 4 speed-up.

2.2 Adiabatic hyperspherical potentials

In this section, we will analyze the adiabatic hyperspherical potential curves together with the channel functions, and compare to those in the BO representation. The hyperradius is a quantity that describes the overall size of our four-body system, so at large R, the solutions to the adiabatic eigenvalue equation include all possible fragmentation channels (not considering $p + p + e^- + e^-$ channel):

$$
\text{H}_2 + \hbar\omega \longrightarrow \begin{cases} \text{H}(n) + \text{H}(n') \\ \text{H}^- + \text{H}^+ \\ \text{H}_2^+(v) + e^- \\ \text{H}(n) + \text{p} + e^- \end{cases}
$$

See Table 2.2 for the corresponding threshold energies with our softcore interactions.

2.2.1 Adiabatic hyperspherical potentials similar to Born-Oppenheimer

The adiabatic hyperspherical representation is similar in spirit to the BO representation. Therefore these adiabatic potentials bear many BO characteristics. We show in Fig. 2.4 the adiabatic hyperspherical potentials for $I = 0$, $S = 0$ and $\Pi = +1$. In Fig. 2.4(a), the lowest curve at large R asymptotes to the binding energy of two ground hydrogen atoms, which corresponds to $X^1\Sigma_g^+$ in the 3D BO notation. The first excited channel possesses a double minimum, which is closely connected to 3D $E + F^1\Sigma_g^+$ BO channel [98]. In terms of channel function, the $1g2g$ (1D notation without angular momentum and the mirror-reflection symmetry with respect to the internuclear axes) configuration is the major one on the plateau right beyond the inner minimum, while the ionic $\text{H}^- + \text{H}^+$ configuration

Table 2.2: *Atomic energies and molecular vibrational levels in our 1D model. H^- has two bound states compared to one bound state in 3D. All these energies are converged to at least 5 digits. The zero of energies are defined as the thresholds of compete breakup ($p+e^-$ for H and $p+p+e^-$/$p+e^-+e^-$ for H_2^+/H^-.*

	energies (a.u.)		energies (a.u.)
H($n=1$)	-0.5000000	H($n=2$)	-0.2329033
H($n=3$)	-0.1338289	H($n=4$)	-0.08477790
H^-(ground)	-0.7079575	H^-(excited)	-0.5058103
$H_2^+(v=0)$	-0.5973959	$H_2^+(v=1)$	-0.5874083
$H_2^+(v=2)$	-0.5780009	$H_2^+(v=3)$	-0.5691544
$H_2^+(v=4)$	-0.5608526	$H_2^+(v=5)$	-0.5530821
$H_2^+(v=6)$	-0.5458325	$H_2^+(v=7)$	-0.5390963
$H_2^+(v=8)$	-0.5328689	$H_2^+(v=9)$	-0.5271488
$H_2^+(v=10)$	-0.5219378	$H_2^+(v=11)$	-0.5172411
$H_2^+(v=12)$	-0.5130679	$H_2^+(v=13)$	-0.5094315
$H_2^+(v=14)$	-0.5063502	$H_2^+(v=15)$	-0.5038476
$H_2^+(v=16)$	-0.5019532	$H_2^+(v=17)$	-0.5007002
$H_2^+(v=18)$	-0.5001067	$H_2^+(v=19)$	-0.5000030

dominates on the Coulomb tail of the outer minimum, which asymptotes to the energy of H^-, -0.7079575 a.u.. The ionic contribution to the configuration decreases at large R due to an avoided crossing between channel $H^- + H^+$ and channel H($n = 1$)+H($n = 2$), see Table 2.2 for the energy details. One can also identify higher Rydberg channels asymptotically according to the thresholds.

A comparison between adiabatic hyperspherical potentials and BO potentials is shown in Fig. 2.5. All the potentials shown in Fig. 2.5 converge to 6 digits or more. We notice the adiabatic hyperspherical potentials match the BO ones quite well for the low lying channels, which is expected since the hyperradius is essentially the same as the inter-nuclear distance in these channels.

2.2.2 Adiabatic hyperspherical potentials beyond Born-Oppenheimer

Ionization channels in the adiabatic hyperspherical representation

The adiabatic hyperspherical potentials can represent more than Rydberg channels and the ionic $H^- + H^+$ channels. Beyond the BO approximation, in Fig. 2.4(a), ionization (dissociative or non-dissociative) channels can also be identified. Their details are shown in Fig. 2.4(b) and (c). In Fig. 2.4(b), a set of channels with Coulomb tails at large R converge to the energies of $H_2^+(v) + e^-$ states. These are non-dissociative ionization channels for 1D H_2. Specifically, around $R = 20$ a.u., $H_2^+(v) + e^-$ channels can be identified for up to $v = 18$
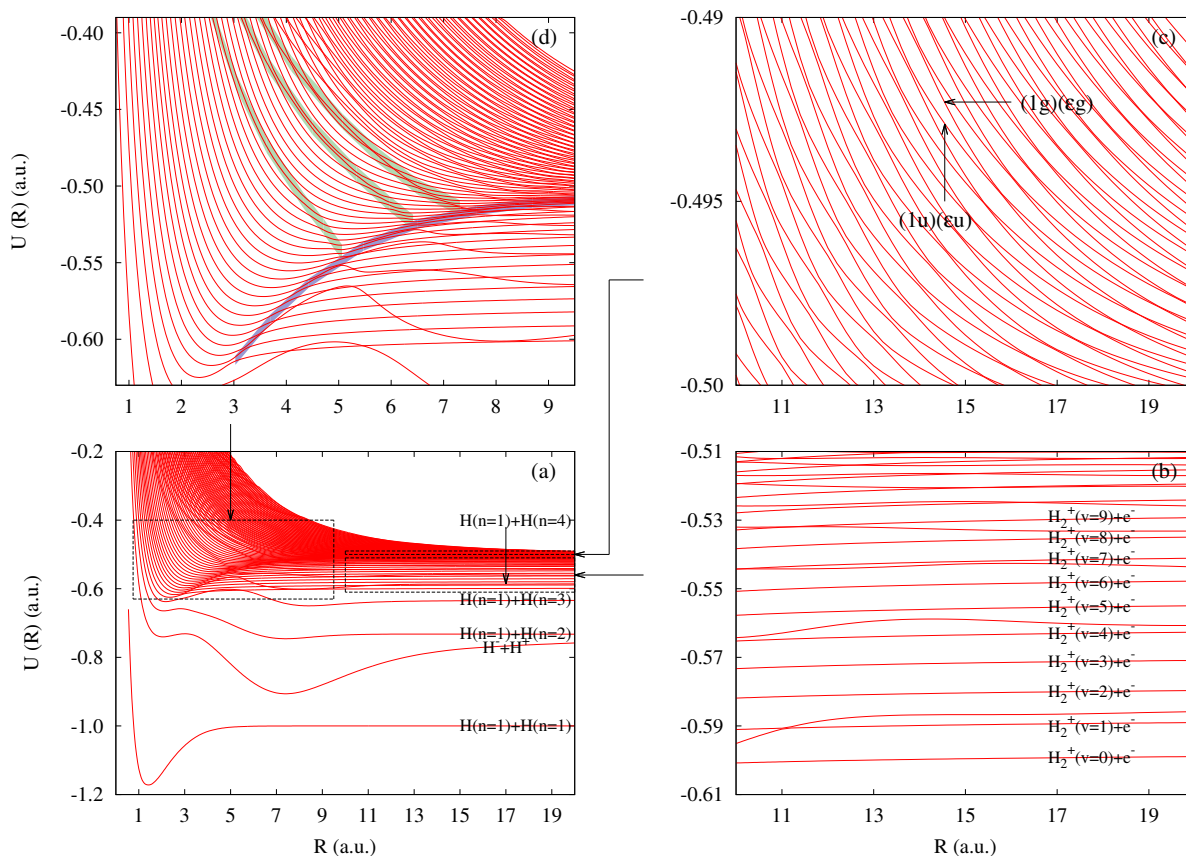
Figure 2.4: *The adiabatic hyperspherical potential curves for $S = 0$ $I = 0$ $\Pi = +1$ in terms of hyperradius R (see text for details).*

(See Table 2.2 for energies).

In Fig. 2.4(c), it's not difficult to notice that there are two families of potential curves above the single ionization threshold (-0.5 a.u.). To identify these adiabatic hyperspherical potential curves, we analyze the channel functions Φ_ν, shown in Fig. 2.6. We can readily see that the wave function localizes in one electronic coordinate but spreads in the other electronic coordinate. We thus conclude that these two families of states are $(1g)(\epsilon g)$ and $(2u)(\epsilon u)$ channels where the ionized electron has energy ϵ.

Avoided crossings and doubly excited states

Interestingly but not surprisingly, in Fig. 2.4(a), there are different sets of avoided crossings, especially at small hyperradii (< 10 a.u. or so) where couplings between different channels are strong. Transitions between different channels occur through these avoided crossings. Among all these avoided crossings, two families particularly draw our attention. We emphasize them in Fig. 2.4(d) by adding green and blue backgrounds and thus producing
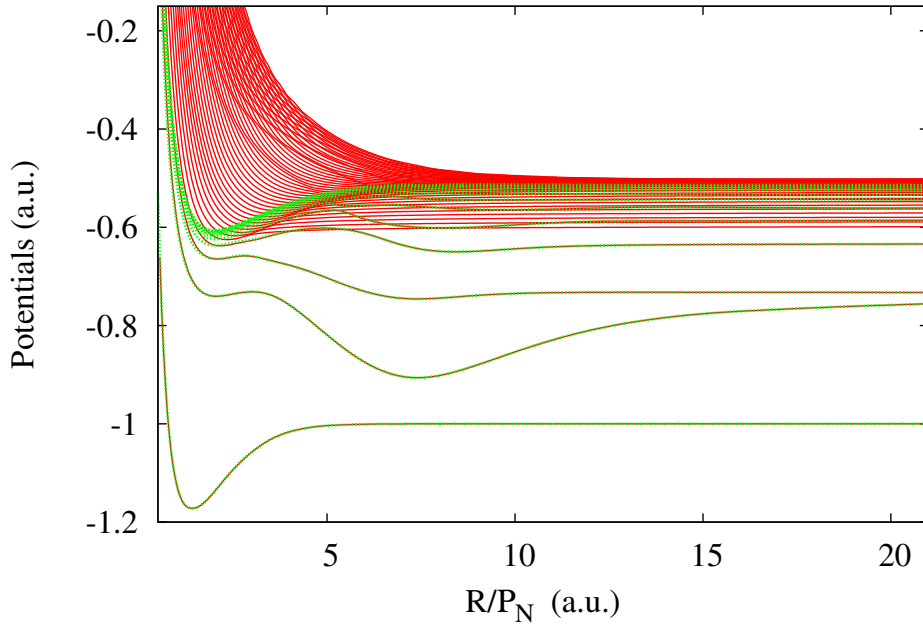
Figure 2.5: *The BO potentials (green dots) plot on top of the adiabatic hyperspherical potentials (red curves).*

"diabatic" channels. One family of the avoided crossings with blue background involves non-dissociative single ionizations. The other with green background indicates autoionization (see details below).

First, we focus on the blue "diabatic" channel, which we call dissociative single ionization channel for 1D H_2. It is essentially the ground H_2^+ $1g$ channel in the four-body representation. The energy of this potential is a little lower than the H_2^+ $1g$ potential due to the Coulomb interaction between the ionizing electron and the H_2^+. To have a better understanding of the role of this "diabatic" channel in molecular dynamics, we sketch the wavepacket dynamics scheme in Fig. 2.7. Assuming a wavepacket with high enough energy is created and propagates on one of the adiabatic hyperspherical potential curves, and comes across an avoided crossing in the dissociative single ionization channel, it will either go to the $H_2^+(v) + e^-$ channel through a non-adiabatic transition and non-dissociatively ionize, or remain in a four-body complex and "climb" the "diabatic" channel. Also in the neighborhood of this "diabatic" channel, there are some avoided crossings between the non-dissociative ionization channel and the Rydberg channel, which lead part of the wavepacket to populate the Rydberg channel and to dissociate. Finally, each time the wavepacket goes through an avoided crossing, it will have similar pathways until it goes higher than the $v = 19$ $H_2^+ + e^-$ vibrational level, where the wavepacket either dissociates to a Rydberg channel or dissociatively ionizes, if energetically allowed.

Next, we discuss the green "diabatic" curves in Fig. 2.4(d). We notice that these curves
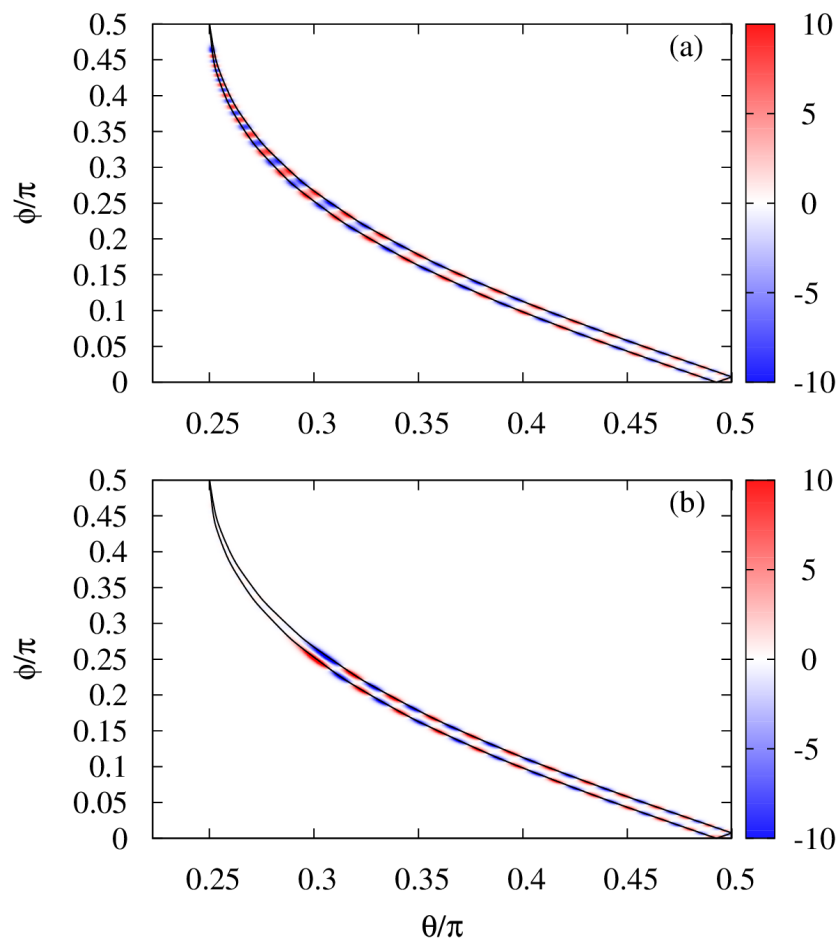
Figure 2.6: *Wave function for continuum states at $R = 15$. (a) is corresponding to $(1g)(\epsilon g)$ channel and (b) is corresponding to $(2u)(\epsilon u)$.*
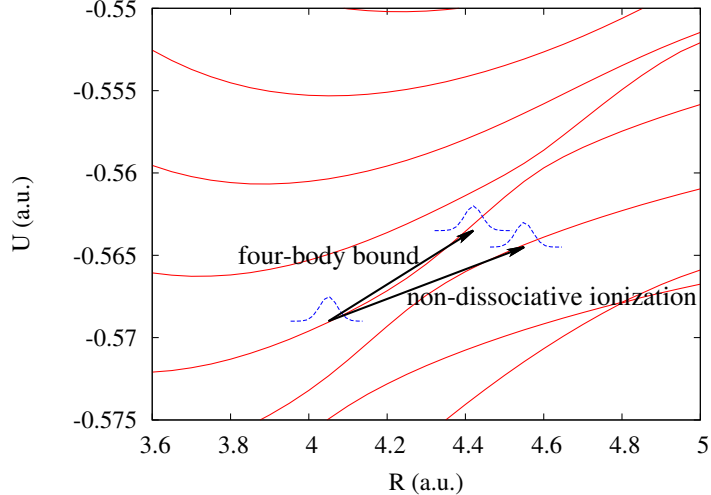
Figure 2.7: *Wavepacket dynamics scheme in dissociative single ionization channel.*

are quite similar to the potentials of doubly excited states in the BO picture [30]. These curves cross the $(1g)(\epsilon g)$ channels, stay below the $(2u)(\epsilon u)$ channels, and asymptote to the Rydberg channels. At small R (< 5 a.u. or so), these curves connect to the doubly excited states. We thus call them doubly excited state channels. For the lowest set of doubly excited states, the configurations are $(2u)(nu)$ (connected to $(2p\sigma_u)(nl\sigma_u)$ in 3D notation, where l is the angular momentum of the emitted electron) in the the molecular basis, where the principle quantum number $n \geq 2$ and the total parity is even. To study the role of the avoided crossings in doubly excited state channels, we again analyze relevant channel functions, shown in Fig. 2.8. First, we show a channel function Φ_ν of the doubly excited state channel in Fig. 2.8(a). It's readily verified that the channel function is relatively localized and is doubly excited in both electronic coordinates. That's exactly what we would expect for doubly excited state channels. When R gets larger, such doubly excited state channels connect to Rydberg channels, $H(n) + H(n')$. In the range of energies in Fig. 2.8, there is another family of curves, the $H_2^+(v) + e^-$, for which we show a channel function in Fig. 2.8(b). Now assuming a wavepacket on the doubly excited state channel, where the channel function is shown in Fig. 2.8(a), propagates on the adiabatic potentials and goes across an avoided crossing, it will either stay in the adiabatic channel and autoionize to the $H_2^+(\nu) + e^-$ continuum, or keep on the "diabatic" doubly excited state channel through non-adiabatic coupling, with channel function shown in Fig. 2.8(c). Each time the wavepacket goes through such avoided crossings, it will face the same situation, autoionizing or being doubly excited. When the system trace down the doubly excited state channels, it will cross the dissociative single ionization channel (blue "diabatic" one) like we sketch in Fig. 2.7.

Furthermore, two points should be made for these potentials. First, the doubly excited state channels together with higher break-up channels in the $(1u)(\epsilon u)$ configuration, which belong to the same family, connect to the Rydberg channels asymptotically by non-adiabatic transitions. These "diabatic" channels are expected to be seen as real channels in a diabatic
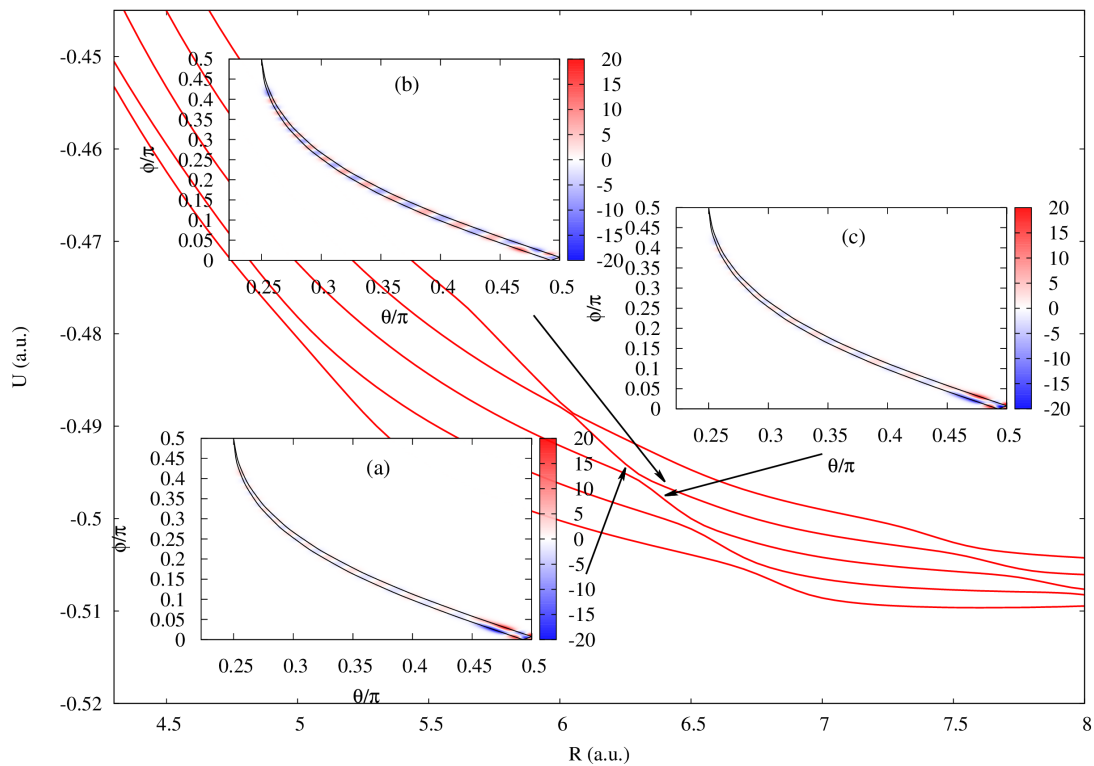
Figure 2.8: *We show part of the adiabatic hyperspherical potential curves, emphasizing the series of avoided crossings on the doubly excited state channel. (a) and (c) show the relevant channel functions bearing doubly excited characteristics in both electronic coordinates. (b) is the channel function cooresponding to $H_2^+(v) + e^-$ configuration.*

picture. Thus the ionizations/continuum states we are discussing here only exist for a specific range of hyperradii. Second, even though we can, in principle, perform hyperradial calculations that solve Eq. (2.9) to get quantitative results, special care needs to be taken to deal with sharp avoided crossings. In 1D H_2 system, the emergence of sharp avoided crossings can be understood by the fact that the geometric configuration of the four-body system is not likely to change abruptly. This makes it possible to treat the shape of the system as a slow-varying parameter to produce a diabatic representation, which is called the shape-diabatic representation [58]. Such a diabatic basis could possibly remove the sharp avoided crossings, thus has some advantage in the hyperradial calculation. In our hyperspherical coordinates, specifically, the hyperangle θ characterizes such geometric configurations. Therefore one can treat both R and θ as adiabatic parameters and solve 1D equations consecutively to construct a shape-diabatic basis.

2.2.3 Autoionization for hydrogen molecule

The mostly commonly used theoretical method for dealing with the hydrogenic diatomic molecules is the BO approach. In the BO representation, one treatment for autoionization or doubly excited states is based on the Feshbach formalism [29, 30, 99–101]. For instance, Martin *et al* use B-spline basis in a box to describe the electronic continuum of two-electron diatomic molecules [29, 30, 101] and expand the total wave function in terms of two orthogonal complementary bases, the non-resonant space P and resonance space Q, together with the ground state. The couplings between these basis functions are included in the time-dependent Schrödinger equation. The coupling between P and Q leads to decay from the bound states to the continuum states, which is autoionization of a single electron.

In the hyperspherical representation, we obtain "diabatic" channels that characterize doubly excited states directly by solving the adiabatic equation. To understand the doubly excited state channel, we again analyze the channel function Φ_ν. We find the doubly excited state channel functions tend to localize in the right bottom corner around the attractive coalescence lines in Fig. 2.3(b), where configuration is like $H(n) + H(n')$. The $H_2^+ + e^-$ channel functions, however, localize on the other side of the same coalescence lines. It seems that some effective barrier is keeping Φ_ν from populating the area in between. To get some insights into this "barrier", one could solve the effective potential along the "r_2" axis by fixing hyperradius and r_1. However, in the "K"-type Jacobi coordinates, where the hyperspherical coordinates are defined as

$$\sqrt{\frac{\mu_N}{\mu}}\rho_N = R\sin\theta\sin\phi$$

$$\sqrt{\frac{\mu_2}{\mu}}r_2 = R\sin\theta\cos\phi$$

$$\sqrt{\frac{\mu_1}{\mu}}r_1 = R\cos\theta,$$
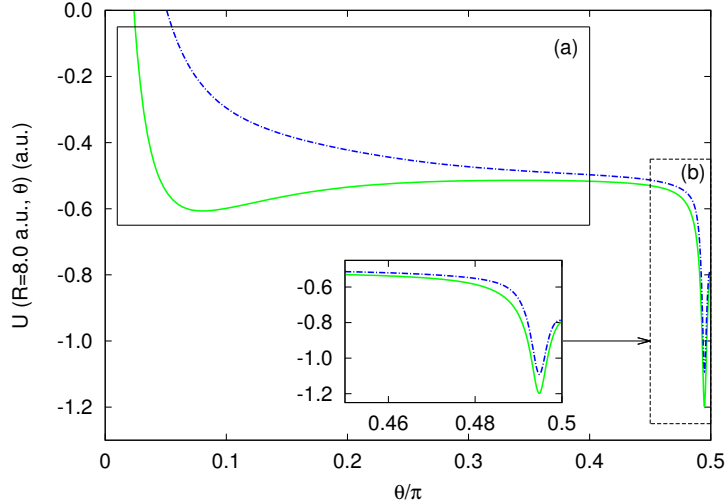
Figure 2.9: *Effective potentials $U(R, \theta)$ in θ for $R = 8$. Inset (a) shows H_2^+ electronic channels, $1s\sigma_g$ and $2p\sigma_u$. Inset (b) shows the region of Rydberg states.*

we practically fix the hyperradius and θ and solve the motion of ϕ. The effective potential $U_{\text{eff}}(R, \theta)$ for fixed $R = 8$ a.u. is shown in Fig. 2.9. We only show θ range from 0 to $\pi/2$ since $U_{\text{eff}}(R, \theta)$ is symmetric with respect to $\theta = \pi/2$. It should be noted that we are essentially solving two different motions by solving ϕ motion. If θ is large or r_1 is small, we effectively solve ρ_N motion and obtain Rydberg states, which is indicated in Fig. 2.9(b). If θ is small or r_1 is large, we effectively solve electronic motion(r_2) and obtain electronic states for H_2^+. We see that the $1g$ and $2u$ channels are recovered in Fig. 2.9(a). We also notice that a barrier, as we expected, shows up in the lower channel. With the effective potentials, we solve for the single-channel solutions in the ground and excited channels respectively and get a series of bound states. The excited states in the excited channel are truly doubly excited states in the united atom limit. If the doubly excited states lie above the barrier of the lower channel, they can decay into $H_2^+ + e^-$. We thus can see a series of avoided crossings in the adiabatic hyperspherical potentials [Fig. 2.4(d)]. These avoided crossings diabatically form the doubly excited states channels [green curves in Fig. 2.4(d)]. For autoionization, the distance between the H_2^+ and the ionized electron will be the dominant contribution to the hyperradius. For lower channels, the doubly excited states are more strongly coupled to the $H_2^+ + e^-$ vibrational states, where the hydrogen molecule won't dissociate but ionize. This type of couplings leads to the other series of the avoided crossings [along blue curve in Fig. 2.4(d)] in the adiabatic hyperspherical potentials.

We've discussed how autoionization is treated in the BO and the hyperspherical representation. The hyperspherical representation is in principle exact and complete. While in the BO picture, electronic continuum states must be discretized with large box size and the continuum states are not unique in contrast to unique discretization of continuum channels in the hyperspherical representation. Also in hyperspherical, the hyperspherical coordinates treat all channels including ionization on equal footings, so that we can analyze all
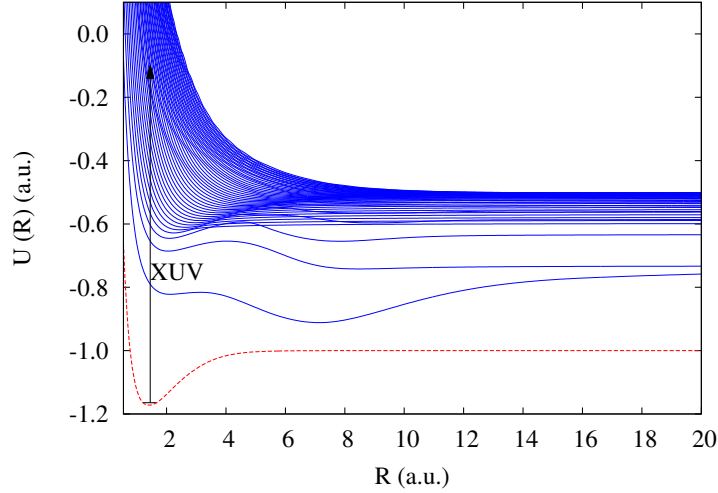
Figure 2.10: *Sketch for transition from vibrational state on the* H_2 *ground channel (dashed red) for total even parity to the excited states on the lowest fifty channels (solid blue) for total odd parity.*

fragmentation processes in H_2 through non-adiabatic transitions.

2.3 Application in ultrafast physics

In this section, we will show a simple example for how these adiabatic hyperspherical potentials can be useful to study attosecond physics. We apply a weak XUV laser field, $\mathcal{E}(t)$, to H_2. Assuming a vibrational state in the H_2 ground channel as the initial state, wavepackets are generated in the excited channels by a one-photon transition. For $I = 0$ and $S = 0$, only $\Pi = -1$ channels can be populated due to the dipole selection rule. Such transitions are schematically illustrated in Fig. 2.10, where the dashed red curve is H_2 ground channel for total even parity, whereas the other curves are the lowest fifty channels for $\Pi = -1$.

The total Hamiltonian is written as $H_0 - \boldsymbol{d} \cdot \boldsymbol{\mathcal{E}}(t)$. [see Eq. (2.2)] The dipole operator is written as $\boldsymbol{d} = \boldsymbol{\rho} = R \cos\theta \hat{z}$. Using first-order perturbation theory, the differential transition probability is written as

$$\frac{dP_{\nu_f}}{dE} = |\langle F_{\nu_f,E}(R)|D_{\nu_f,\nu_i}(R)|F_{\nu_i}(R)\rangle|^2 |\tilde{\mathcal{E}}(E)|^2 \qquad (2.10)$$

where $\tilde{\mathcal{E}}(E)$ is the Fourier transform of the electric field, and $D_{\nu_f,\nu_i}(R)$ are the dipole matrix elements:

$$D_{\nu_f,\nu_i}(R) = \langle \Phi_{\nu_f}(R;\theta,\phi)|d|\Phi_{\nu_i}(R;\theta,\phi)\rangle \qquad (2.11)$$

21

In general, molecular dynamics can be manipulated by changing the laser parameters in $|\tilde{\mathcal{E}}|^2$ [102, 103]. For instance, one can consider to study H_2 with a two-color XUV pulse, using the bandwidth of the pulse to control the number of channels that are populated. In a two-color study, one can also manipulate the relative CEP between the two colors to manipulate overlap of the pulse in the frequency domain, thus to gain control over the wavepacket distribution when the laser is gone. However, in this chapter, we focus on the structural information and its role in molecular dynamics. We study the dipole matrix elements $D_{\nu_f,\nu_i}(R)$ to gain some insights in the differential transition probability without doing sophisticated, time-dependent calculations. We assume the initial state is the lowest vibrational state in the ground channel, and calculate the dipole matrix elements between ground channel with $I = 0$, $S = 0$ and $\Pi = +1$ (dashed red curve in Fig. 2.10) and channels with $I = 0$, $S = 0$ and $\Pi = -1$ (solid blue curves in Fig. 2.10).

Previous works [33, 34] have shown that the doubly excited states are significant in dissociate ionization of H_2, we thus analyze the dipole matrix elements in the vicinity of doubly excited states, i.e. around the avoided crossings in the doubly excited state channels. We show in Fig. 2.11(a) the adiabatic hyperspherical potential curves for channels $\nu_f = 10$ to $\nu_f = 22$ and the dipole matrix element $D_{\nu_f=15,\nu_i=1}$ in Fig. 2.11(b). Since the initial state is the ground vibrational state, we focus on dipole matrix elements in the vicinity of the Franck-Condon region. In Fig. 2.11(a), the potential curves have been scaled to better show the avoided crossings. It can be readily noticed that the absolute value of the dipole matrix element oscillates at small R, and the oscillation frequency is proportional to the frequency of the emergence of the avoided crossings. Also it's surprising that the dipole matrix elements peaks for the $H_2^+ + e^-$ dominating channels but are minimized for doubly excited state channels, and vice versa for large R. This can be explained by noting that the overlap between the ground channel and the $H_2^+ + e^-$ channels is larger than that between the ground channel to the doubly excited channels, and again vice versa for large R. So, from dipole matrix elements we conclude that in our 1D model, at least, the $H_2^+ + e^-$ channels rather than the doubly excited state channel are more likely to be populated during the pulse at small R. But one should be aware that after the pulse is gone, initial wavepacket will propagate among these adiabatic channels, and go across different families of avoided crossings. Channels with different characters will finally be populated through different pathways coherently.

We show in Fig. 2.12(b) the dipole matrix elements for $\nu_f = 1$ to 6, and also show revelant adiabatic hyperspherical potential curves in Fig. 2.12(a). We notice that the dipole matrix element for $\nu_f = 1$, the $H^+ + H^-$ channel, maximizes in the vicinity of the outer minimum of the final state potential, where the ionic geometric configuration dominates. This is not surprising since the ionic character bears large classical dipole moment. We also see that at large R the dipole matrix element for channel $H(1) + H(2)$ (dashed green) is much larger than other Rydberg channels such as $H(1) + H(3)$ (dashed blue). This is also expected since the ground state $H(n = 1)$ is more likely to generate a large dipole moment with the odd parity atomic state $H(n = 2)$ than with those atomic states bearing even parity. Also the $H(n = 2)$ atomic state carries a more localized wave function than the other Rydberg states, such as $H(n = 4)$. So the dipole matrix element associated to
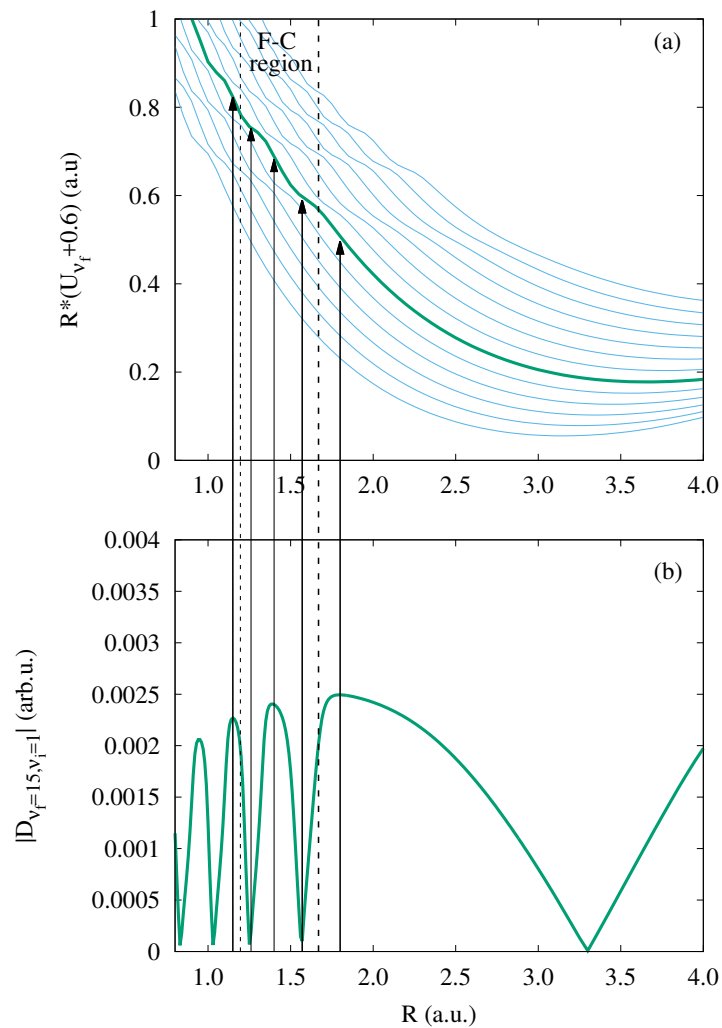
Figure 2.11: *(a) The 10th-22th adiabatic hyperspherical potential curves for $I = 0$, $S = 0$ and $\Pi = -1$. (b) Absolute value of the dipole matrix elements between the ground channel and the 15th channel in (a). The dot dashed lines indicate the Franck-Condon region.*
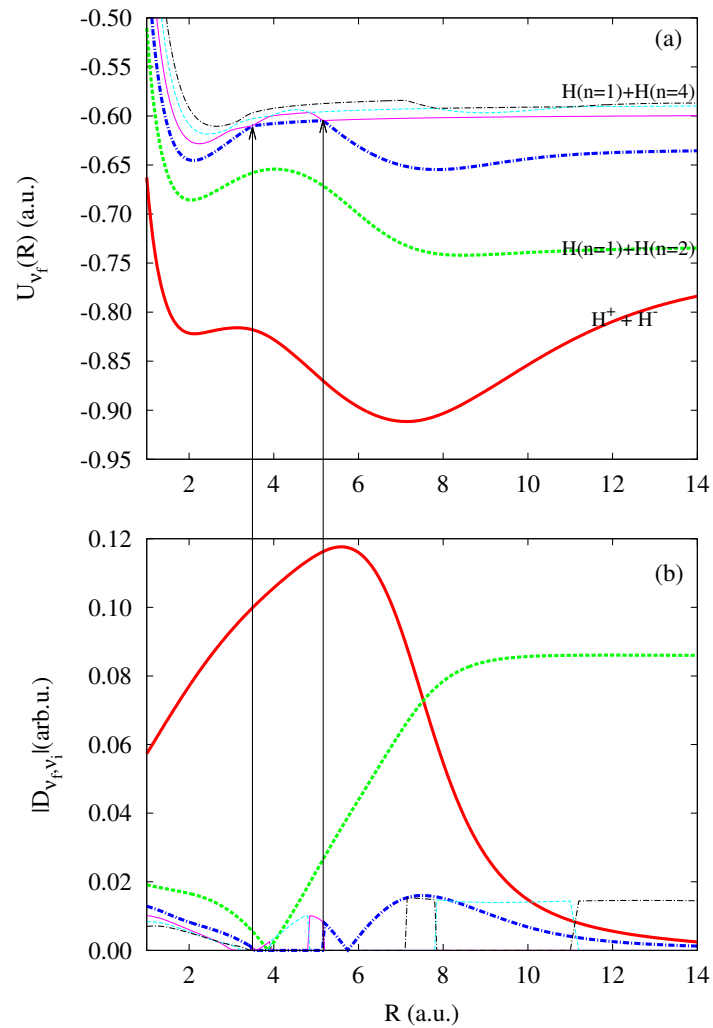
Figure 2.12: *(a) The lowest six channels for $I = 0$, $S = 0$ and $\Pi = -1$. (b) Absolute value of the dipole matrix elements from the ground channel to the channels in (a). The color and line-type schemes are the same on both panels.*

H(1) + H(2) is larger than that associated with H(1) + H(4) (dashed black) at large R. Another point we want to make through Fig. 2.12 is that the dipole matrix elements for ν_f corresponding to $H_2^+(v) + e^-$ states are vanishingly small. Take the third channel (dashed blue) for example, the dipole matrix element is approximately zero between the two arrows, where $H_2^+(v = 1) + e^-$ character shows up. Similarly, on the right side of the second arrow, the dipole matrix elements vanish for the fourth channel, which also bears $H_2^+(v = 1) + e^-$ character. This is due to the fact that the overlaps between the $H_2^+(v)+e^-$ channel functions and the ground channel function are almost zero. Furthermore, if the dynamics start from a much higher vibrational state where the size of the wavepacket can be extended to around 5 a.u. instead of ground state in the Franck-Condon region, one would expect, from Fig. 2.12, that direct ionization from the ground channel as the first step will be negligible.

2.4   Summary

To summarize, we use the adiabatic hyperspherical representation, for the first time, to treat a one-dimensional model of the hydrogen molecule. Effective potentials for all ionization channels and doubly excited states can be identified. We also propose an exemplar application of these adiabatic potentials in ultrafast physics and study the relevant dipole matrix elements, where we get qualitative insights in the diatomic molecular dynamics. For instance, information about the initial wavepacket distribution when the pulse is gone can be obtained by studying the magnitudes of dipole matrix elements. Our study shows that the adiabatic hyperspherical approach is a good candidate to study strongly correlated molecular dynamics.

Chapter 3

Strong-field two-center effects in diatomic molecular ionization

In this chapter, we move to studies of molecular dynamics, where we would like to solve the time-dependent Schrödinger equation in three spatial dimensions. In this case, including all degrees of freedom is simply not feasible considering current computational capability. We thus solve the diatomic molecular ionization in the fixed-nuclei framework.

3.1 Theoretical formalism

Previously, spheroidal coordinates have been proven useful in solving two-center problems, for both time-independent [104] and time-dependent studies [105, 106].

3.1.1 Time-dependent Schrödinger equation

The full-dimensional time-dependent Schrödinger equation (TDSE) for H_2^+, where the nuclei are fixed along the laser polarization direction, is written as

$$i\frac{\partial}{\partial t}\Psi(\boldsymbol{R};\boldsymbol{r},t) = \left(\frac{(\boldsymbol{p}+\boldsymbol{A}(\boldsymbol{r},t)/c)^2}{2\mu} + V\right)\Psi(\boldsymbol{R};\boldsymbol{r},t) \tag{3.1}$$

where $\boldsymbol{p} = -i\nabla$ and $\boldsymbol{r}$ are the electron's momentum and position relative to the center of the nuclei, $\boldsymbol{A}$ is the vector potential for the laser field, and V is the electron's Coulomb interaction with the nuclei. Atomic units are used throughout this section unless otherwise stated. Since the wavelengths we will consider are 800 nm or more—which is much longer than the size of the system —and the intensities are weak enough to neglect the effect of the magnetic field of the laser, we can use the electric dipole approximation, i.e. $\boldsymbol{A}(\boldsymbol{r},t) = \boldsymbol{A}(t)$. Under this approximation, the term $\mathcal{A}^2(t)$ can be eliminated by a simple time-dependent

phase. Eq. (3.1) thus becomes the velocity gauge TDSE

$$i\frac{\partial}{\partial t}\Psi(\boldsymbol{r},t) = (H_0 + W)\,\Psi(\boldsymbol{r},t) \tag{3.2}$$

where the field-free Hamiltonian $H_0 = -\frac{1}{2\mu}\nabla_r^2 + V$ and the interaction $W = \frac{\boldsymbol{A}(t)\cdot\boldsymbol{p}}{\mu c}$.

We solve Eq. (3.2) in prolate spheroidal coordinates (PSC), which have proven suitable for two-center problems [104–106]. In particular, for two-center Coulomb problems as in this work, the Coulomb singularities are located at the boundaries in PSC, thus reconciling the numerical difficulty. See the book by Flammer [107] for details about spheroidal coordinates and wave functions. The prolate spheroidal coordinates for H$_2^+$ in the center-of-mass frame are thus defined as

$$\xi = \frac{r_A + r_B}{R},\ \ 1 \le \xi < \infty$$
$$\eta = \frac{r_A - r_B}{R},\ \ -1 \le \eta < 1,$$

where $r_{A/B}$ is the distance between the electron and proton A/B, and the azimuthal angle χ ranges from 0 to 2π. The 3D volume element is

$$dV = \frac{R^3}{8}(\xi^2 - \eta^2)d\xi d\eta d\chi$$

and the electronic Laplacian has the prolate spheroidal definition

$$\nabla_r^2 = \frac{4}{R^2(\xi^2 - \eta^2)}\left[\frac{\partial}{\partial \xi}(\xi^2 - 1)\frac{\partial}{\partial \xi} + \frac{\partial}{\partial \eta}(1 - \eta^2)\frac{\partial}{\partial \eta} + \frac{1}{(\xi^2 - 1)}\frac{\partial^2}{\partial \chi^2} + \frac{1}{(1 - \eta^2)}\frac{\partial^2}{\partial \chi^2}\right]. \tag{3.3}$$

The Coulomb interaction between the electron and nuclei is

$$V(\xi,\eta) = -\frac{Z_A}{r_A} - \frac{Z_B}{r_B} = -\frac{2(Z_A + Z_B)\xi + 2(Z_B - Z_A)\eta}{R(\xi^2 - \eta^2)}. \tag{3.4}$$

where the charge could be generalized to other diatomic systems. The time-dependent interaction reads

$$W = \frac{1}{\mu c}\boldsymbol{A}(t)\cdot\boldsymbol{p} = -\frac{i}{\mu c}\boldsymbol{A}(t)\cdot\boldsymbol{\nabla}. \tag{3.5}$$

We choose $\boldsymbol{A}(t) = \mathcal{A}(t)\hat{z}$. Because

$$\boldsymbol{\nabla} = \frac{1}{2}[\nabla^2, \boldsymbol{r}], \tag{3.6}$$

the interaction term W thus becomes

$$W = -\frac{i}{\mu c}\mathcal{A}(t)\frac{\partial}{\partial z} = -\frac{i}{\mu c}\mathcal{A}(t)\frac{1}{2}[\nabla^2, z] = -\frac{i}{\mu c}\mathcal{A}(t)\frac{1}{2}[\nabla^2, \frac{R}{2}\xi\eta] \tag{3.7}$$

with $z = \frac{R}{2}\xi\eta$, and

$$[\nabla^2, \frac{R}{2}\xi\eta] = \frac{2}{R}\eta\left[\frac{1}{\xi^2 - \eta^2}\frac{\partial}{\partial\xi}(\xi^2 - 1)\frac{\partial}{\partial\xi}\xi - \frac{\xi}{\xi^2 - \eta^2}\frac{\partial}{\partial\xi}(\xi^2 - 1)\frac{\partial}{\partial\xi}\right]$$
$$+ \frac{2}{R}\xi\left[\frac{1}{\xi^2 - \eta^2}\frac{\partial}{\partial\eta}(1 - \eta^2)\frac{\partial}{\partial\eta}\eta - \frac{\eta}{\xi^2 - \eta^2}\frac{\partial}{\partial\eta}(1 - \eta^2)\frac{\partial}{\partial\eta}\right]. \tag{3.8}$$

The vector potential $\mathcal{A}(t)$ for the electric field is expressed as

$$\mathcal{A}(t) = \frac{c}{\omega}\mathcal{E}_0 e^{-(t/\tau)^2}\sin(\omega t + \varphi)\hat{z}. \tag{3.9}$$

We use pulses with a full width of the intensity at half maximum (FWHM), $\tau_{\text{FWHM}} \approx \tau\sqrt{2\ln 2}$, of 10 fs and a wavelength of 780 nm. The intensity is taken as 1×10^{14} W/cm^2. The carrier-envelope phase (CEP) is set $\varphi = 0$ unless stated otherwise.

In Eq. (3.2), the azimuthal angle χ-dependence in Ψ could be separated by

$$\Psi(\xi, \eta, \chi, t) = \sum_\Lambda \Psi_\Lambda(\xi, \eta, t)\frac{e^{i\Lambda\chi}}{\sqrt{2\pi}}. \tag{3.10}$$

Thus Eq. (3.2) reduces:

$$i\frac{\partial\Psi_\Lambda(\xi, \eta, t)}{\partial t} = (H_0^\Lambda + W)\Psi_\Lambda(\xi, \eta, t), \tag{3.11}$$

where,

$$H_0^\Lambda = -\frac{2}{\mu R^2(\xi^2 - \eta^2)}\left(\frac{\partial}{\partial\xi}(\xi^2 - 1)\frac{\partial}{\partial\xi} + \frac{\partial}{\partial\eta}(1 - \eta^2)\frac{\partial}{\partial\eta}\right.$$
$$\left. -\frac{\Lambda^2}{(\xi^2 - 1)} - \frac{\Lambda^2}{(1 - \eta^2)} + \mu R(Z_A + Z_B)\xi + \mu R(Z_B - Z_A)\eta\right). \tag{3.12}$$

Since the laser pulse is linearly polarized along z-axis, the azimuthal quantum number $\Lambda = 0$ — for the ground state — is conserved. Therefore, we will not discuss the azimuthal angle in our work.

Equation (3.11), as a partial differential equation in two spatial dimensions, could be solved in various discretized representations, such as discrete variable representation [105, 106, 108], finite difference [109, 110], or B-splines [104, 111]. We choose B-splines (see Appendix C.1 for details) for this work.

In B-splines representation, the wave function Ψ_Λ is expanded as

$$\Psi_\Lambda(\xi, \eta, t) = \sum_{ij} c_{ij}(t) u_i(\xi) v_j(\eta). \tag{3.13}$$

By projecting out the basis splines, Equation (3.11) can then be written as a matrix form

$$i\boldsymbol{S}\dot{\boldsymbol{c}} = \boldsymbol{H}\boldsymbol{c} \tag{3.14}$$

where the Hamiltonian matrix $\boldsymbol{H} = \boldsymbol{H}_0^\Lambda + \boldsymbol{W}$ has matrix elements evaluated as

$$
\begin{aligned}
(H_0^\Lambda)_{ij,i'j'} &= \int_1^\infty d\xi \int_{-1}^1 d\eta (\xi^2 - \eta^2) u_i(\xi) v_j(\eta) H_0 u_{i'}(\xi) v_{j'}(\eta) \\
&= -\frac{2}{\mu R^2} \left[\int_1^\infty d\xi \left(-\frac{\partial u_i}{\partial \xi} (\xi^2 - 1) \frac{\partial u_i'}{\partial \xi} - \frac{\Lambda^2}{(\xi^2 - 1)} u_i u_i' \right) S_\eta \right. \\
&\quad + \int_{-1}^1 d\eta \left(-\frac{\partial v_j}{\partial \eta} (1 - \eta^2) \frac{\partial v_{j'}}{\partial \eta} - \frac{\Lambda^2}{(1 - \eta^2)} v_j v_{j'} \right) S_\xi \\
&\quad \left. + \int_1^\infty d\xi \, u_i \mu R(Z_A + Z_B) \xi u_{i'} S_\eta + \int_{-1}^1 d\eta \, v_j(\eta) \mu R(Z_B - Z_A) \eta v_{j'} S_\xi, \right]
\end{aligned} \tag{3.15}
$$

where

$$(S_\xi)_{ii'} = \int_1^\infty d\xi \, u_i u_{i'}$$

$$(S_\eta)_{jj'} = \int_{-1}^1 d\eta \, v_j v_{j'},$$

and

$$
\begin{aligned}
W_{ij,i'j'} &= \int_1^\infty d\xi \int_{-1}^1 d\eta (\xi^2 - \eta^2) u_i(\xi) v_j(\eta) W u_{i'}(\xi) v_{j'}(\eta) \tag{3.16} \\
&= -\frac{iA(t)}{cR} \int_1^\infty d\xi \int_{-1}^1 d\eta u_i(\xi) v_j(\eta) \left[\eta \left(\frac{\partial}{\partial \xi} (\xi^2 - 1) \frac{\partial}{\partial \xi} \xi - \xi \frac{\partial}{\partial \xi} (\xi^2 - 1) \frac{\partial}{\partial \xi} \right) \right. \\
&\quad \left. + \xi \left(\frac{\partial}{\partial \eta} (1 - \eta^2) \frac{\partial}{\partial \eta} \eta - \eta \frac{\partial}{\partial \eta} (1 - \eta^2) \frac{\partial}{\partial \eta} \right) \right] u_{i'}(\xi) v_{j'}(\eta) \tag{3.17} \\
&= -\frac{i\mathcal{A}(t)}{cR} \left\{ \int_{-1}^1 d\eta v_j \eta v_{j'} \int_1^\infty d\xi \left[u_i(\xi^2 - 1) \frac{\partial u_{i'}}{\partial \xi} - \frac{\partial u_i}{\partial \xi} (\xi^2 - 1) u_{i'} \right] \right. \\
&\quad \left. + \int_{-1}^1 d\eta \left[v_j(1 - \eta^2) \frac{\partial v_{j'}}{\partial \eta} - \frac{\partial v_j}{\partial \eta} (1 - \eta^2) v_{j'} \right] \int_1^\infty d\xi u_i \xi u_{i'} \right\}. \tag{3.18}
\end{aligned}
$$

Note Eq. (3.18) is derived from Eq. (3.17) through integral by parts.

The elements of the overlap matrix $\boldsymbol{S}$ are

$$S_{ij,i'j'} = \int_1^\infty d\xi \int_{-1}^1 d\eta (\xi^2 - \eta^2) u_i(\xi) v_j(\eta) u_{i'}(\xi) v_{j'}(\eta) \tag{3.19}$$

$$= \int_1^\infty d\xi \ \xi^2 u_i u_{i'} S_\eta - \int_{-1}^1 d\eta \ \eta^2 v_j v_{j'} S_\xi \tag{3.20}$$

The kinetic energy matrix elements above are derived from the weak form (see Appendix C.2 for details) of the variational principle. This is also the case for any kinetic energy matrix elements evaluated in this thesis.

Note that Eq. (3.1) has also been solved in the length gauge (see Appendix D for details) for validation of the formalism and the code as well.

3.1.2 Coordinate transformation

The $\Psi_\Lambda(\xi, \eta)$ in Eq. (3.11) become non-analytic at $\xi = 1$, $\eta = \pm 1$ for odd Λ's — behaving as $(\xi^2 - 1)^{\frac{|\Lambda|}{2}} (1 - \eta^2)^{\frac{|\Lambda|}{2}}$. Thus, they cannot be represented by polynomial bases such as B-splines. To resolve this issue, we transform ξ and η to some other variables, i.e.

$$\xi = \cosh x \qquad\qquad 0 \leqslant x \leqslant \infty \tag{3.21}$$
$$\eta = \cos y \qquad\qquad 0 \leqslant y \leqslant \pi, \tag{3.22}$$

even though only $\Lambda = 0$ is considered in this work. Such treatment could also work for the scaled radial wave function in PSC when solving for the scattering states since the scaled radial solution also behaves as $(\xi^2 - 1)^{\frac{1}{2}}$. (one could easily derive the radial equation for scaled radial function in PSC. In Sec. 3.1.6, though, we will only solve for the unscaled radial function)

After the coordinate transformation, the Hamiltonian matrix elements are evaluated as

$$
\begin{aligned}
(H_0^\Lambda)_{ij,i'j'} =& \frac{2}{\mu R^2} \left(\int_0^\infty dx \ \sinh x [\frac{\partial u_i}{\partial x} \frac{\partial u_{i'}}{\partial x} + \frac{\Lambda^2}{\sinh^2 x} u_i u_{i'}] S_\eta \right. \\
&\left. + \int_0^\pi dy \ \sin y [\frac{\partial v_j}{\partial y} \frac{\partial v_{j'}}{\partial y} + \frac{\Lambda^2}{\sin^2 y} v_j v_{j'}] S_\xi \right) \\
&- \frac{2(Z_A + Z_B)}{R} \int_0^\infty dx \ \sinh x \cosh x u_i u_{i'} S_\eta \\
&- \frac{2(Z_B - Z_A)}{R} \int_0^\pi dy \ \sin y \cos y v_j v_{j'} S_\xi,
\end{aligned}
\tag{3.23, 3.24}
$$

and

$$W_{ij,i'j'} = -\frac{i\mathcal{A}(t)}{cR} \left[\int_0^\pi dy v_j \sin y \cos y v_{j'} \int_0^\infty dx \sinh x \left(u_i \sinh x \frac{\partial u_{i'}}{\partial x} - \frac{\partial u_i}{\partial x} \sinh x u_{i'} \right) \right.$$
$$\left. + \int_0^\pi dy \sin y \left(v_j(-\sin y)\frac{\partial v_{j'}}{\partial y} - \frac{\partial v_j}{\partial y}(-\sin y)v_{j'} \right) \int_0^\infty dx \sinh x \cosh x u_i u_{i'} \right], \quad (3.25)$$

where

$$(S_\xi)_{ii'} = \int_1^\infty d\xi \; u_i u_{i'} = \int_0^\infty dx \; \sinh x u_i u_{i'} \tag{3.26}$$

$$(S_\eta)_{jj'} = \int_{-1}^1 d\eta \; v_j v_j' = \int_0^\pi dy \; \sin y v_j v_{j'}, \tag{3.27}$$

and the overlap matrix elements are

$$S_{ij,i'j'} = \int_0^\infty dx \; \sinh x \cosh^2 x u_i u_{i'} S_\eta - \int_0^\pi dy \; \sin y \cos^2 y v_j v_{j'} S_\xi. \tag{3.28}$$

3.1.3 Iterative propagation

We solve Eq. (3.14) over one time step δ using a Padé [1/1] approximation [112] to the short-time propagator

$$\boldsymbol{c}(t+\delta) = e^{-i\boldsymbol{S}^{-1}\boldsymbol{H}(t+\frac{\delta}{2})\delta}\boldsymbol{c}(t) = \left[\boldsymbol{S} + i\boldsymbol{H}(t+\frac{\delta}{2})\frac{\delta}{2} \right]^{-1} \left[\boldsymbol{S} - i\boldsymbol{H}(t+\frac{\delta}{2})\frac{\delta}{2} \right] \boldsymbol{c}(t). \tag{3.29}$$

where $\boldsymbol{H}(t+\delta) = \boldsymbol{H}_0 + \boldsymbol{W}(t+\delta/2)$. Treating $\boldsymbol{W}(t+\delta/2)$ as a perturbation, the matrix inversion in Eq. (3.29) is obtained via a power series [113–115].

Specifically, the inversion in Eq. (3.29) adapts a matrix-splitting method called Neumann expansion

$$(A+B)^{-1} = \sum_{n=0}^\infty (-A^{-1}B)^n A^{-1}, \tag{3.30}$$

where the convergence requires the maximum eigenvalue of $A^{-1}B$ to have an absolute value less than 1. Thus the explicit form for the inversion in Eq. (3.29) is

$$\left[\boldsymbol{S} + i\boldsymbol{H}(t+\frac{\delta}{2})\frac{\delta}{2} \right]^{-1} = \sum_{n=0}^{n_{\max}} \left[-\left(\boldsymbol{S} + i\frac{\delta}{2}\boldsymbol{H}_0 \right)^{-1} i\frac{\delta}{2}\boldsymbol{W} \right]^n \left(\boldsymbol{S} + i\frac{\delta}{2}\boldsymbol{H}_0 \right)^{-1} \tag{3.31}$$

with a maximum order of $n_{\max}$ (typically less than 10), which is adjusted dynamically at each iteration by requiring that the norm of the wave function is unitary to the machine precision, i.e. 16 digits. Importantly, the inversion on the right-hand-side of Eq. (3.31) only

involves time-independent matrices, thus the factorization in the linear solve only needs to be done once. The back substitutions and matrix-vector multiplications, however, are required for each iteration in Eq. (3.31).

As noted in Ref. [113], this propagation scheme has a clear advantage over the split-operator approach used in our previous work [116]. It avoids the well-known commutator errors that require a smaller δt to compensate.

Although the matrix-splitting method — Eq. (3.31) — allows accurate solutions, the overall accuracy of the propagation scheme is limited by the $O(\delta t^3)$ error induced by the short-time propagator. Note the interaction matrix $\boldsymbol{W}$ in Eq. (3.14) involves R^{-1}, thus δt can be relaxed to a larger number with increasing R. This feature seems favorable. However, due to Coulomb singularities at the nuclei, more points will be needed on the spatial grid close to the nuclei as R increases. In practice, we search numerical parameters for a desired accuracy at small R's say $R = 50$, then increase the δt as well as the number of grid points for larger R.

The initial state in the propagation is solved using the same numerical method stated in Sec. 2.1.4.

3.1.4   Complex absorption potential and ionization yield

In solving Eq. (3.11), we apply a complex absorbing potential (CAP) at the grid boundaries to absorb the outgoing electronic flux. The CAP is added into the field-free Hamiltonian H_0. The form of the CAP is systematically designed to achieve certain absorption criteria, as discussed in Chapter 6. The specific form of th CAP used in this work is called "double-sinh":

$$V(r) = -\frac{\hbar^2}{2m}\frac{\alpha_1^2}{2\sinh\frac{(r_{\max}-r)}{2\beta}} - i\frac{\hbar^2}{2m}\frac{\alpha_2^2}{4\sinh^2\frac{(r_{\max}-r)}{2\beta}} \tag{3.32}$$

with r being the electronic radial coordinate and $r_{\max}$ being the grid boundary. We use $\alpha_1^2 = 0.296 + 0.0308i$, $\alpha_2^2 = 0.707 - 0.0642i$, and $\beta = 1.97$. Detail discussions about CAP in general can be found in Chapter 6.

To apply the CAP to prolate spheroidal coordinates, we simply transform the spherical radial coordinate r to (ξ, η) by

$$r = \frac{R}{2}\sqrt{(\xi^2 - 1)(1 - \eta^2) + \xi^2\eta^2}. \tag{3.33}$$

Due to the benefit from the CAP, the box size required to obtain the total ionization yield is tremendously reduced — more than a factor of 2 — since the wavepacket getting absorbed at the boundary is counted as part of the ionization. The total ionization yield is thus written as

$$P = 1 - \sum_n P_n \tag{3.34}$$

where P_n is the bound state population remained at the end of the pulse.

3.1.5   Numerical discussion

For the iterative propagation in Sec. 3.1.3, the matrix-vector products are computed via an Intel `MKL` [117] sparse `BLAS` routine, namely *zcsrgemv*, where the matrix is stored in the CSR format. The linear solve is done via the Intel `MKL PARDISO` (Parallel Direct Sparse Solver) [118]. The propagation has also been done using a banded matrix solver, which takes advantage of the Intel `MKL` banded matrix routines. However, by comparing these two, we find at least a factor of 2 speedup for the sparse solver (matrix-vector multiply plus linear solve) in present calculations. Unfortunately, the sparse-direct solver–`PARDISO` does not parallelize as well as the banded solver. In general, for a Hamiltonian bearing a banded structure, such as in B-splines as discussed in Sec. 2.1.4, the higher the dimension, the sparser the matrix, thus the more advantage of the sparse solver over the banded one.

The efficiency of the TDSE solver is further improved by optimizing the (ξ, η) grid. First, the maximum value of ξ could be defined by the radial distance of the electron in spherical coordinates centered at one of the nuclei, r_{max}, as

$$\xi_{\mathrm{max}} = 1 + \frac{2r_{\mathrm{max}}}{R}, \tag{3.35}$$

where r_{max} should be large enough that the wave function of the atomic state with the largest hydrogenic principal quantum number n is contained within the distance. Such a quantum number, however, is not available a priori since the Rydberg states populated during the pulse are unknown. In practice, we treat r_{max} as a convergence parameter. In the calculations, we have chosen the ξ grid distribution to be quadratic at small values to resolve fast oscillations due to the Coulomb potential, and linear at large distance. The η distribution is chosen to be linear over the whole range, except for extra points added around $\eta = \pm 1$—the positions of two nuclei. Overall, the calculations require $r_{\mathrm{max}} \geq 400$ a.u. (including the absorbing range) and about 800 splines in ξ and 80 splines in η. The propagation time step is about 0.04 a.u.. Without fine tuning of numerical parameters, each calculation for single R and single initial state takes about 10 to 20 CPU hours for a 3.50GHz Intel Xeon CPU (E5-2637 v3), single threaded. All the ionization yields shown in this work are converged to at least two digits ($<1\%$) with respect to the grid size as well as the other parameters. The validity of the formalism is verified by performing a test calculation for the ionization of atomic hydrogen and comparing the ionization yield to a result generated by an independent atomic code in spherical coordinates. They agree to 3 significant digits, which is also the convergence level.

3.1.6   Energy analysis

In this subsection, we analyze the solution of the Schrödinger equation in Sec. 3.1.1 to obtain the momentum distribution and the energy spectrum. The formalism is adapted from the free-particle version in the book by Flammer [107]. We also followed previous

work [119] for parts of the derivation and found a few issues with it that we resolved in our derivation below.

Separation of variables in prolate spheroidal coordinates

We want to solve for the energy normalized scattering states for the diatomic molecule in prolate spheroidal coordinates with the nuclei fixed. The Schrödinger equation is written as:

$$\left(-\frac{1}{2\mu}\nabla^2 + V - E\right)\Psi(\xi, \eta, \chi) = 0, \tag{3.36}$$

with the Laplacian ∇^2 given in Eq. (3.3) and the Coulomb interaction V in Eq. (3.4). Again, the χ-dependence is of no significance for $\Lambda = 0$ in this work. It is separated from Ψ by Eq. (3.10). Then Eq. (3.36)—reads

$$-\frac{2}{\mu R^2(\xi^2 - \eta^2)}\left(\frac{\partial}{\partial\xi}(\xi^2 - 1)\frac{\partial}{\partial\xi} + \frac{\partial}{\partial\eta}(1 - \eta^2)\frac{\partial}{\partial\eta}\right.$$
$$\left.-\frac{\Lambda^2}{(\xi^2 - 1)} - \frac{\Lambda^2}{(1 - \eta^2)} + \mu R(Z_A + Z_B)\xi + \mu R(Z_B - Z_A)\eta\right)\Psi_\Lambda(\xi, \eta) = E\Psi_\Lambda(\xi, \eta). \tag{3.37}$$

The wave function Ψ_Λ takes the form $\Psi_\Lambda = R_\Lambda(\xi)S_\Lambda(\eta)$, in which we call the "radial" wave function $R_\Lambda(\xi)$ and the "angular" wave function $S_\Lambda(\eta)$. By separation of variables, Eq. (3.37) reduces to

$$\left(\frac{\partial}{\partial\xi}(\xi^2 - 1)\frac{\partial}{\partial\xi} - \frac{\Lambda^2}{(\xi^2 - 1)} + \mu R(Z_A + Z_B)\xi + c^2\xi^2 - A_\Lambda\right)R_\Lambda(\xi) = 0 \tag{3.38}$$

and

$$\left(\frac{\partial}{\partial\eta}(1 - \eta^2)\frac{\partial}{\partial\eta} - \frac{\Lambda^2}{(1 - \eta^2)} + \mu R(Z_B - Z_A)\eta - c^2\eta^2 + A_\Lambda\right)S_\Lambda(\eta) = 0, \tag{3.39}$$

where $c = \frac{kR}{2}$ and $k = \sqrt{2\mu E}$.

Angular equation

The separation constant A_Λ is obtained by solving the eigenvalue problem—with $E > 0$ specified beforehand—in the "angular" equation Eq. (3.39), which is re-written as

$$H_\eta^\Lambda S_{\Lambda n}(\eta) = A_{\Lambda n}S_{\Lambda n}(\eta), \tag{3.40}$$

where the "angular" Hamiltonian is

$$H_\eta^\Lambda = -\frac{\partial}{\partial \eta}(1 - \eta^2)\frac{\partial}{\partial \eta} + \frac{\Lambda^2}{1 - \eta^2} - \mu R(Z_B - Z_A)\eta + c^2\eta^2, \tag{3.41}$$

and n is the quantum number for H_η^Λ.

In B-splines representation,

$$S_{\Lambda n}(\eta) = \sum_i c_i v_i(\eta). \tag{3.42}$$

Then, the matrix elements for the Hamiltonian are written as

$$(H_\eta^\Lambda)_{ij} = \int_0^1 d\eta \left[\frac{\partial v_i}{\partial \eta}(1 - \eta^2)\frac{\partial v_j}{\partial \eta} + v_i \left(\frac{\Lambda^2}{1 - \eta^2} - \mu R(Z_B - Z_A)\eta + c^2\eta^2\right)v_j\right] \tag{3.43}$$

or

$$(H_\eta^\Lambda)_{ij} = \int_0^{\frac{\pi}{2}} dy \left[\sin y \frac{\partial v_i}{\partial y}\frac{\partial v_j}{\partial y}\right.$$
$$\left. +v_i \left(\frac{\Lambda^2}{\sin y} - \mu R(Z_B - Z_A)\sin y \cos y + c^2 \sin y \cos^2 y\right)v_j\right] \tag{3.44}$$

for the angle-like coordinate. The overlap matrix is evaluated as in Eq. (3.27).

Radial equation

To solve the radial equation

$$\left(\frac{\partial}{\partial \xi}(\xi^2 - 1)\frac{\partial}{\partial \xi} - \frac{\Lambda^2}{(\xi^2 - 1)} + R(Z_A + Z_B)\xi + c^2\xi^2 - A_{\Lambda n}\right)R_{\Lambda n}(\xi) = 0, \tag{3.45}$$

where n indicates the state from Eq. (3.40), we use the eigenchannel R-matrix method [90], which, however, has to be modified since the standard R-matrix formalism is in spherical coordinates.

In the eigenchannel R-matrix approach, we calculate the eigenstates for the R-matrix. This means that for each such eigenstate, the solution has a constant logarithmic derivative at the boundary:

$$b = -\frac{1}{R_{\Lambda n}}\frac{dR_{\Lambda n}}{d\xi}. \tag{3.46}$$

The variational principle for b can be derived easily as in Ref. [90], starting from the exact

expression for electronic energy,

$$E = \frac{\int d\xi R^*_{\Lambda n} H^\Lambda_\xi R_{\Lambda n}}{\int d\xi R^*_{\Lambda n} \frac{\mu R^2}{2} \xi^2 R_{\Lambda n}} \tag{3.47}$$

where

$$H^\Lambda_\xi = -\left(\frac{\partial}{\partial\xi}(\xi^2 - 1)\frac{\partial}{\partial\xi} - \frac{\Lambda^2}{(\xi^2 - 1)} + R(Z_A + Z_B)\xi - A_{\Lambda n} \right). \tag{3.48}$$

With integration by parts and a little algebra,

$$b = \frac{\int d\xi \left[-\frac{\partial R^*_{\Lambda n}}{\partial\xi}(\xi^2 - 1)\frac{\partial R_{\Lambda n}}{\partial\xi} + R^*_{\Lambda n}\left(c^2\xi^2 + R(Z_A + Z_B)\xi - \frac{\Lambda^2}{\xi^2 - 1} - A_{\Lambda n} \right) R_{\Lambda n} \right]}{R^*_{\Lambda n}(\xi^2 - 1)R_{\Lambda n}|_{\xi_{max}}}. \tag{3.49}$$

In B-splines representation, $R^*_{\Lambda n} = \sum_i c_i u_i$ and $R_{\Lambda n} = \sum_j c_j u_j$, Eq. (3.49) becomes

$$b(c_i) = \frac{\sum_{ij} c_i c_j \Gamma_{ij}}{\sum_{ij} c_i c_j \Lambda_{ij}}, \tag{3.50}$$

where

$$\begin{aligned}
\Gamma_{ij} &= \int d\xi \left\{ -\frac{\partial u_i}{\partial\xi}(\xi^2 - 1)\frac{\partial u_j}{\partial\xi} + u_i\left[c^2\xi^2 + R(Z_A + Z_B)\xi - \frac{\Lambda^2}{\xi^2 - 1} - A_{\Lambda n} \right] u_j \right\} \\
&= \int_0^{x_{max}} dx \sinh x \left[-\frac{\partial u_i}{\partial x}\frac{\partial u_j}{\partial x} \right. \\
&\quad \left. + u_i\left(c^2 \cosh^2 x + R(Z_A + Z_B)\cosh x - A_{\Lambda n} - \frac{\Lambda^2}{\sinh^2 x} \right) u_j \right],
\end{aligned} \tag{3.51}$$

and

$$\Lambda_{ij} = u_i(\xi^2 - 1)u_j|_{\xi_{max}} = u_i \sinh^2 x u_j|_{x_{max}}. \tag{3.52}$$

Using $\frac{db}{dc_i} = 0$, we arrive at the generalized eigenvalue problem for b, which is given in matrix form by

$$\mathbf{\Gamma}\vec{c} = b\mathbf{\Lambda}\vec{c}. \tag{3.53}$$

Using the streamlined formulation [90], the Γ and Λ matrices are divided into open and closed spaces according to the behavior of the basis function on the boundary, i.e. "closed" means the basis function is zero at the boundary. The eigenvector is thus divided into open and closed spaces

$$\vec{c} = (\vec{d_c}, d_o). \tag{3.54}$$

The eigenvalue b can be written as

$$b = \frac{\Omega_{oo}}{\Lambda_{oo}}, \tag{3.55}$$

where $\Omega_{oo} = \Gamma_{oo} - \mathbf{\Gamma}_{oc}\mathbf{\Gamma}_{cc}^{-1}\mathbf{\Gamma}_{co}$. Note that Λ_{oo} is the only non-zero element in matrix $\mathbf{\Lambda}$. The main computational step is to evaluate $\mathbf{\Gamma}_{cc}^{-1}$. Let $\mathbf{\Gamma}_{cc}^{-1}\mathbf{\Gamma}_{co} = \vec{B}_{co}$, and solve linear equation $\mathbf{\Gamma}_{cc}\vec{B}_{co} = \mathbf{\Gamma}_{co}$. The "closed" eigenvector is then given by

$$\vec{d_c} = -\vec{B}_{co}d_o, \tag{3.56}$$

where d_o is obtained by matching the asymptotic solution of radial equation.

Now, we need to know the asymptotic behavior for $R_{\Lambda n}$. With a little algebra, Eq. (3.38) reads

$$\left(\frac{\partial^2}{\partial\xi^2} + \frac{2\xi}{(\xi^2-1)}\frac{\partial}{\partial\xi} + c^2\frac{\xi^2}{\xi^2-1} + R(Z_A + Z_B)\frac{\xi}{(\xi^2-1)} - \frac{A_{\Lambda n}}{(\xi^2-1)} - \frac{\Lambda^2}{(\xi^2-1)^2} \right) \\ \times R_{\Lambda n}(\xi) = 0 \tag{3.57}$$

and, with some simplification,

$$\left\{ \frac{\partial^2}{\partial\xi^2} + \left[\frac{2}{\xi} + O(\xi^{-3}) \right]\frac{\partial}{\partial\xi} + c^2 + \frac{R(Z_A + Z_B)}{\xi} - \frac{A_{\Lambda n}}{\xi^2} + O(\xi^{-3}) \right\} R_{\Lambda n}(\xi) = 0. \tag{3.58}$$

Neglecting $O(\xi^{-3})$ as for asymptotic behavior, we have Coulomb-like equation

$$\left\{ \frac{\partial^2}{\partial\xi^2} + \frac{2}{\xi}\frac{\partial}{\partial\xi} + c^2 + \frac{R(Z_A + Z_B)}{\xi} - \frac{A_{\Lambda n}}{\xi^2} \right\} R_{\Lambda n}(\xi) = 0. \tag{3.59}$$

With $\xi_s = c\xi$ and $R_{\Lambda n} = R_{\Lambda n}^s/\xi_s$, Eq. (3.59) is

$$\left[\frac{\partial^2}{\partial\xi_s^2} + 1 + \frac{R(Z_A + Z_B)}{c\xi_s} - \frac{A_{\Lambda n}}{\xi_s^2} \right] R_{\Lambda n}^s(\xi_s) = 0, \tag{3.60}$$

thus,

$$R_{\Lambda n}^s(c\xi) \xrightarrow{\xi\to\infty} N\sin(c\xi + \frac{R(Z_A + Z_B)}{2c}\ln(2c\xi) - \frac{l^*\pi}{2} + \sigma_{l^*}) \tag{3.61}$$

where σ_{l^*} is the Coulomb phase and l^* is defined as $l^*(l^* + 1) = A_{\Lambda n}$. The ξ-dependent term $\frac{R(Z_A+Z_B)}{2c}\ln(2c\xi)$ indicates that the wavelength of the Coulomb wave approaches the asymptotic limit $2\pi/c$ very slowly, due to the long range nature of the Coulomb potential. Note that N is the normalization constant, which satisfies the energy normalization

asymptotically:

$$
\begin{aligned}
\int d\xi \frac{R^3}{8} \xi^2 R_{\Lambda n}(c'\xi) R_{\Lambda n}(c\xi) &= \int d\xi \frac{R^3}{8} \xi^2 \frac{R^s_{\Lambda n}(c'\xi)}{c'\xi} \frac{R^s_{\Lambda n}(c\xi)}{c\xi} \\
&= \frac{R^3}{8} \xi^2 \frac{N'N}{c'c\xi^2} \frac{\pi}{2} \delta(c - c') \\
&= \frac{R}{2} \frac{N'N}{k'k} \frac{\pi}{2} \frac{dk}{dc} \delta(k - k') \\
&= \frac{N'N}{k'k} \frac{\pi}{2} \delta(k - k') \\
&= \delta(E - E') \\
&= \frac{dk}{dE} \delta(k - k') \\
&= \frac{\mu}{k} \delta(k - k'),
\end{aligned}
\tag{3.62}
$$

leading to the normalization constant

$$
N = \sqrt{\frac{2\mu k}{\pi}},
\tag{3.63}
$$

which is different from the normal constant in spherical coordinates due to the factor c. Therefore, the open space function is

$$
\begin{aligned}
d_o = R_{\Lambda n}|_{\xi=\xi_{\max}} &= \sqrt{\frac{2\mu k}{\pi}} \frac{1}{c\xi} R^s_{\Lambda n}|_{\xi=\xi_{\max}} \\
&\cong \frac{1}{c\xi} \sqrt{\frac{2\mu k}{\pi}} \left[F_{l^*}(\eta_c, c\xi_{\max}) \cos(\Delta_{\Lambda l^*}) + G_{l^*}(\eta_c, c\xi_{\max}) \sin(\Delta_{\Lambda l^*}) \right].
\end{aligned}
\tag{3.64}
$$

where F_{l^*} and G_{l^*} are the regular and irregular Coulomb functions, and $\Delta_{\Lambda l^*}$ is the phase shift.

With the closed-space function obtained through Eq. (3.56). We have thus arrived at the energy normalized radial solution.

Momentum distribution

In spherical coordinates, the pure Coulomb wave satisfying the outgoing-wave (incoming plane wave, outgoing spherical wave) boundary condition is written as [120]

$$
\Psi_C^{(+)}(\boldsymbol{r}) = \sum_l (2l + 1) i^l e^{i\sigma_l} \frac{F_l(\eta_c, kr)}{kr} P_l(\cos\theta),
\tag{3.65}
$$

In a half collision problem, the Coulomb wave needs to satisfy the incoming-wave boundary condition (outgoing plane wave, incoming spherical wave), where we take the complex

conjugate of the boundary condition for $\Psi_C^{(+)}(\boldsymbol{r})$ in Eq. (3.65) and change the direction of $\hat{k}$. We thus obtain $\Psi_C^{(-)}$ satisfying the desired boundary condition

$$
\begin{aligned}
\Psi_C^{(-)}(\boldsymbol{r}) &= \sum_l (2l+1)(-i)^l e^{-i\sigma_l} \frac{F_l(\eta_c, kr)}{kr} P_l(-\cos\theta) \\
&= \sum_l (2l+1) i^l e^{-i\sigma_l} \frac{F_l(\eta_c, kr)}{kr} P_l(\cos\theta) \\
&= 4\pi \sum_{lm} i^l e^{-i\sigma_l} \frac{F_l(\eta_c, kr)}{kr} Y_{lm}^*(\hat{k}) Y_{lm}(\hat{r}).
\end{aligned}
\tag{3.66}
$$

Including the short-range scattering for the two centers, the full scattering wave function asymptotically is expressed as

$$
\Psi_{\boldsymbol{k}}^{(-)}(\boldsymbol{r}) = \Psi_C^{(-)}(\boldsymbol{r}) + f'(\hat{k}) \frac{e^{-i(kr - \eta \ln 2kr)}}{r},
\tag{3.67}
$$

with $f'(\hat{r})$ as the scattering amplitude induced by the short range potential.

In prolate spheroidal coordinates, however, the plane wave can also be expanded as [107]

$$
e^{i\boldsymbol{k}\cdot\boldsymbol{r}} = 4\pi \sum_{\Lambda n} i^n \mathcal{Y}_{\Lambda n}^*(\eta_k, \chi_k) \mathcal{Y}_{\Lambda n}(\eta, \chi) \mathcal{R}_{\Lambda n}(c\xi)
\tag{3.68}
$$

where $\mathcal{R}_{\Lambda n}(\xi)$ is a spheroidal radial function of the first kind, and the "spheroidal harmonic" $\mathcal{Y}_{\Lambda n}(\eta, \chi)$ is defined as

$$
\mathcal{Y}_{\Lambda n}(\eta, \chi) = S_{\Lambda n}(\eta) \frac{e^{i\Lambda\chi}}{\sqrt{2\pi}},
\tag{3.69}
$$

with $S_{\Lambda n}(\eta)$ as the prolate spheroidal angular function of the first kind with order Λ and degree $n = 0, 1, 2, ...$ The $\mathcal{Y}_{\Lambda n}(\eta, \chi)$ are normalized according to

$$
\int_{-1}^{1} d\eta \int_{0}^{2\pi} d\chi \, \mathcal{Y}_{\Lambda n}^*(\eta, \chi) \mathcal{Y}_{\Lambda'n'}(\eta, \chi) = \delta_{nn'} \delta_{\Lambda\Lambda'}.
\tag{3.70}
$$

Asymptotically, $c\xi \to kr$, the spheroidal radial solution becomes the spherical radial solution. Thus similar to that in spherical coordinates, the spheroidal Coulomb wave corresponding to Eq. (3.65) is

$$
\Psi_C^{(+)}(\boldsymbol{r}) \xrightarrow{\xi \to \infty} \frac{N}{(2\pi)^{\frac{3}{2}}} 4\pi \sum_{\Lambda n} i^{l^*} \mathcal{Y}_{\Lambda n}^*(\eta_k, \chi_k) \mathcal{Y}_{\Lambda n}(\eta, \chi) e^{i\sigma_{l^*}} \frac{F_{l^*}(\eta_c, c\xi)}{c\xi}.
\tag{3.71}
$$

If the internuclear distance is $R = 0$, l^* reduces to integer n, and $S_{\Lambda n}(\eta)$ reduces to the associated Legendre function.

To satisfy the incoming-wave boundary condition as for Eq. (3.66), we have

$$
\begin{aligned}
\Psi_C^{(-)}(\boldsymbol{r}) \xrightarrow{\xi\to\infty} &\frac{N}{(2\pi)^{\frac{3}{2}}} 4\pi \sum_{\Lambda n} \mathcal{Y}_{\Lambda n}^*(-\eta_k, \chi_k+\pi) \mathcal{Y}_{\Lambda n}(\eta, \chi)(-i)^{l^*} e^{-i\sigma_{l^*}} \frac{F_{l^*}(\eta_c, c\xi)}{c\xi} \\
=& \frac{N}{(2\pi)^{\frac{3}{2}}} 4\pi \sum_{\Lambda n} (-1)^{n-\Lambda}(-1)^{\Lambda} \mathcal{Y}_{\Lambda n}^*(\eta_k, \chi_k) \mathcal{Y}_{\Lambda n}(\eta, \chi)(-i)^{l^*} e^{-i\sigma_{l^*}} \frac{F_{l^*}(\eta_c, c\xi)}{c\xi} \\
=& \frac{N}{(2\pi)^{\frac{3}{2}}} 4\pi \sum_{\Lambda n} (-1)^{n+l^*} \mathcal{Y}_{\Lambda n}^*(\eta_k, \chi_k) \mathcal{Y}_{\Lambda n}(\eta, \chi) i^{l^*} e^{-i\sigma_{l^*}} \frac{F_{l^*}(\eta_c, c\xi)}{c\xi}.
\end{aligned}
\tag{3.72}
$$

where N is the normalization constant, same as before.

Therefore, the full asymptotic scattering wave can be written as

$$
\Psi_{\text{scatt}}^{(-)}(\boldsymbol{r}) \xrightarrow{\xi\to\infty} \Psi_C^{(-)}(\boldsymbol{r}) + f' \frac{e^{-i[c\xi - \frac{R(Z_A+Z_B)}{2c}\ln(2c\xi)]}}{c\xi},
\tag{3.73}
$$

where again f' is the scattering amplitude resulting from the short range potential. The outgoing part is expressed as

$$
\left(\Psi_{\text{scatt}}^{(-)}\right)_{\text{out}} \xrightarrow{\xi\to\infty} \frac{4\pi N}{(2\pi)^{\frac{3}{2}}} \sum_{\Lambda n} \mathcal{Y}_{\Lambda n}^*(\eta_k, \chi_k) \mathcal{Y}_{\Lambda n}(\eta, \chi)
$$
$$
\times (-1)^{n+l^*} \frac{i^{l^*}}{c\xi} \frac{1}{2i} e^{i\left[c\xi + \frac{R(Z_A+Z_B)}{2c}\ln(2c\xi) - \frac{l^*\pi}{2}\right]}.
\tag{3.74}
$$

On the other hand, the numerical two-center Coulomb scattering wave is expanded on the spheroidal harmonics

$$
\Psi_E^{(-)}(\boldsymbol{r}) = \sum_{\Lambda n} B_{\Lambda n} \mathcal{Y}_{\Lambda n}(\eta, \chi) R_{\Lambda n}(c\xi).
\tag{3.75}
$$

Asymptotically,

$$
R_{\Lambda n}(c\xi) \xrightarrow{\xi\to\infty} \frac{N}{c\xi}\sqrt{\frac{2}{\pi}} \sin(c\xi + \frac{R(Z_A+Z_B)}{2c}\ln(2c\xi) - \frac{l^*\pi}{2} + \sigma_{l^*} + \Delta_{\Lambda n})
\tag{3.76}
$$

where $\Delta_{\Lambda n}$ is the phase shift. The outgoing part of $\Psi_E^{(-)}$ is written as

$$
\left(\Psi_E^{(-)}\right)_{\text{out}} \xrightarrow{\xi\to\infty} \sum_{\Lambda n} B_{\Lambda n} \mathcal{Y}_{\Lambda n}(\eta, \chi) \frac{N}{c\xi}\sqrt{\frac{2}{\pi}}\frac{1}{2i} e^{i\left[c\xi + \frac{R(Z_A+Z_B)}{2c}\ln(2c\xi) - \frac{l^*\pi}{2} + \sigma_{l^*} + \Delta_{\Lambda n}\right]}.
\tag{3.77}
$$

By matching Eq. (3.74) and Eq. (3.77), we have the desired boundary condition and $B_{\Lambda n}$ is

obtained

$$B_{\Lambda n} = (-1)^{n+l^*} i^{l^*} e^{-i(\sigma_{l*} + \Delta_{\Lambda n})} \mathcal{Y}_{\Lambda n}^*(\eta_k, \chi_k). \tag{3.78}$$

Finally, the full scattering solution satisfying the outgoing-wave boundary condition is

$$\Psi_E^{(-)}(\boldsymbol{r}) = \sum_{\Lambda n} (-1)^{n+l^*} i^{l^*} e^{-i(\sigma_{l*} + \Delta_{\Lambda n})} \mathcal{Y}_{\Lambda n}^*(\eta_k, \chi_k) \mathcal{Y}_{\Lambda n}(\eta, \chi) R_{\Lambda n}(c\xi). \tag{3.79}$$

To get the scattering solution — energy or momentum normalized — we simply take, respectively

$$N = \sqrt{\frac{2\mu k}{\pi}} \text{ or } N = k\sqrt{\frac{2}{\pi}} \tag{3.80}$$

in Eq. (3.76).

Therefore, we obtain the momentum distribution by projecting the wave function in Eq. (3.11) to the energy normalized scattering states:

$$\frac{\partial P}{\partial E \partial \theta} = \int d\chi_k |\langle \Psi_E^{(-)} | \Psi(t_f) \rangle|^2 = |\sum_n \langle M_{\Lambda n} S_{\Lambda n}(\eta) R_{\Lambda n}(\xi) | \Psi_\Lambda(\xi, \eta, t_f) \rangle|^2 \tag{3.81}$$

where $M_{\Lambda n} = (-1)^{n+l^*} i^{l^*} e^{-i(\sigma_{l*} + \Delta_{\Lambda n})} S_{\Lambda n}^*(\eta_k)$, and $\Psi_\Lambda(\xi, \eta, t_f)$ is the time-dependent wave function at the end of the pulse. Note again that the azimuthal quantum number $\Lambda = 0$ is conserved.

Expanding the wave functions in the B-splines bases,

$$R_{\Lambda n}(\xi) = \sum_i c_i^n u_i(\xi)$$

$$S_{\Lambda n}(\eta) = \sum_j c_j^n v_j(\eta)$$

$$\Psi_\Lambda(\xi, \eta, t_f) = \sum_{i,j} c_{ij}(t_f) u_i(\xi) v_j(\eta),$$

Eq. (3.81) reduces to

$$\frac{\partial P}{\partial E \partial \theta} = \left| \langle \sum_n M_{\Lambda n} \sum_j c_j^n v_j \sum_i c_i^n u_i | \sum_{i',j'} c_{i'j'}(t_f) u_{i'} v_{j'} \rangle \right|^2$$

$$= \left| \sum_{ij,i'j'} \sum_n M_{\Lambda n}^*(\theta) c_j^{n*} c_i^{n*} c_{i'j'}(t_f) \mathcal{S}_{ij,i'j'} \right|^2, \tag{3.82}$$

with the overlap matrix $\boldsymbol{\mathcal{S}}$ evaluated in Eq. 3.20.

Energy spectrum

The energy spectrum can thus be obtain by integrating the momentum distribution over angles:

$$
\begin{aligned}
\frac{dP}{dE} &= \iint d\eta_k d\chi_k |\langle \Psi_E^{(-)} | \Psi(t_f) \rangle|^2 \\
&= \iint d\eta_k d\chi_k \left[\sum_{\Lambda n} \langle (-1)^{n+l^*} i^{l^*} e^{-i(\sigma_{l*}+\Delta_{\Lambda n})} \mathcal{Y}_{\Lambda n}^*(\eta_k, \chi_k) \mathcal{Y}_{\Lambda n}(\eta, \chi) R_{\Lambda n}(c\xi) | \Psi(t_f) \rangle \right] \\
&\quad \times \left[\sum_{\Lambda' n'} \langle \Psi(t_f) | (-1)^{n'+l^{*'}} i^{l^{*'}} e^{-i(\sigma_{l*'}+\Delta_{\Lambda' n'})} \mathcal{Y}_{\Lambda' n'}^*(\eta_k, \chi_k) \mathcal{Y}_{\Lambda' n'}(\eta, \chi) R_{\Lambda' n'}(\xi) \rangle \right]. \quad (3.83)
\end{aligned}
$$

Given the orthogonality of the spheroidal harmonics, i.e. Eq. (3.70), the energy spectrum can be simplified as

$$
\frac{dP}{dE} = \sum_n \left| \langle (-1)^{n+l^*} i^{l^*} e^{-i(\sigma_{l*}+\Delta_{\Lambda n})} S_{\Lambda n}(\eta) R_{\Lambda n}(c\xi) | \Psi_\Lambda(t_f) \rangle \right|^2. \quad (3.84)
$$

Again, in B-Spline representation, Eq. (3.81) becomes

$$
\begin{aligned}
\frac{dP}{dE} &= \sum_n \left| \langle \sum_j c_j^n v_j(\eta) \sum_i c_i^n u_i(\xi) | \sum_{i',j'} c_{i'j'}(t_f) u_{i'}(\xi) v_{j'}(\eta) \rangle \right|^2 \\
&= \frac{\mu R^2}{4c} \sum_n \left| \sum_{ij,i'j'} c_j^{n*} c_i^{n*} c_{i'j'}(t_f) \mathcal{S}_{ij,i'j'} \right|^2 \quad (3.85)
\end{aligned}
$$

with $\mathcal{S}_{ij,i'j'}$ evaluated in Eq. 3.20.

Note that the correctness of the energy analysis formalism is verified by reproducing an independent atomic photoelectron energy distribution in a test example.

3.2 Strong-field two-center effects beyond double-slit interference

3.2.1 Two center interference effect: homonuclear diatomic molecules

In this section, we focus on the ionization of H_2^+ at large internuclear separations — $30 < R < 150$ a.u. — where two lowest states are essentially degenerate and the linear combinations of the atomic orbitals (LCAO) almost exactly approximate the molecular states. In such cases, intuitively, one would not expect molecular physics to play a significant role, especially when it approaches the high end of R ($\sim$150 a.u.).

In Fig. 3.1, however, we show the total ionization yield as a function of R for the gerade and ungerade initial electronic states for H_2^+, i.e. P_g and P_u. First, the well-known enhanced ionization at critical distance [4, 5] of H_2^+ is reproduced for intermediate R range from 4 to 16 a.u., as shown in the inset. Interestingly, one can notice such enhanced ionization is strongly symmetry-dependent. For the case of the ungerade initial state, the enhancement peak moves to somewhat smaller R for the same set of laser parameters, and the enhancement is much higher than that of the gerade initial state. This is partially due to the fact that the ionization potential for the ungerade initial state is smaller than that of the gerade initial state. However, it does not explain the ionization yield at other R, for example the yield for $2p\sigma_u$ is smaller than that for $1s\sigma_g$ at $R = 11$ a.u..
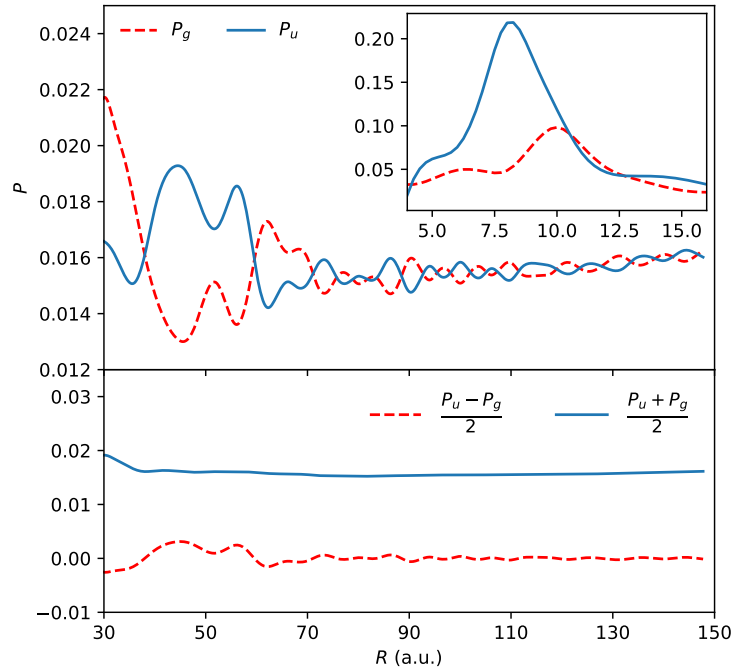
Figure 3.1: *Ionization probability as a function of R for the gerade–P_g and ungerade–P_u initial states (upper) and the decomposition of $P_u(R)$ (lower), for a Gaussian pulse with the FWHM of 10 fs, an intensity of 10^{14} W/cm^2, and the wavelength of 780 nm.*

Surprisingly, in the large-R region in Fig. 3.1, a pronounced interference feature is found in the total ionization yield, which oscillates dramatically as a function of R. Such interference, however, fades away as R increases, which is expected because as the internuclear separation gets larger the central wavelength of the electronic wavepacket becomes negligible compared to R. A good example sharing similar physical footing is the study of the photoelectron spectrum for diatomic molecular ionization [70], where the photoelectron scattering intensity loses its interference as the momentum increases, i.e. the wavelength decreases away from the bond length of the nuclei. Such loss in interference in the photoelectron spectrum can also be confirmed by Cohen and Fano's prediction ($\sim 1 + \frac{\sin kr}{kr}$) [65]. Moreover, for

$R > 30$ a.u. in Fig. 3.1, the ionization yield shows an even stronger symmetry-dependence compared to that at the critical distance. Further, the ionization yield oscillates as a function of R in the opposite direction for gerade and ungerade initial states at $R>30$ a.u.. The oscillation of the total ionization yield as a function of R can also be found in the S-matrix based KFR theory [18, 121] for H_2^+, where ionization yield with different initial symmetries oscillates in the opposite direction. Besides these two features, the KFR theory, however, completely fails to predict the magnitude of the total yield, and does not match the TDSE solution even qualitatively. Another interesting point for the R-dependent yield in Fig. 3.1 is the broad peak of ionization for R ranging from 40 to 60 a.u. for the ungerade initial state, which could be potentially measured in experiments (will be discussed more in Chapter 5).

Apparently, the rich structures in Fig. 3.1 at large R come from the molecular nature. For diatomic molecular ionization, one would probably think of the two-center nature of the system. Most of the previous studies of two-center effect in molecular ionization follow Cohen and Fano's picture [65] of molecular two-center interference, which is essentially a single-photon process. It predicts oscillation behavior for differential quantities, such as the photoelectron spectrum. However, for integral quantities such as the total yield, such formalism does not predict any interference pattern. Therefore, in the following, we numerically explore the strong-field two-center effect by examining the interference term in the total ionization yield at large internuclear distances.

For H_2^+, we start from gerade/ungerade initial wave functions

$$\Psi_{g/u}(t_i) = \frac{1}{\sqrt{2}} \left[\Phi_A(R;r) \pm \Phi_B(R;r)\right], \tag{3.86}$$

where g/u indicates the $1s\sigma_g/2p\sigma_u$ electronic channels, and $\Phi_{A/B}$ is simply the atomic orbital centered at A/B. Such LCAO represents $\Psi_{g/u}$ almost exactly for the large R's concerned in the present work. The final state is thus written as

$$\Psi_f^{g/u} = U(t_f, t_i)\Psi_{g/u}(t_i) \tag{3.87}$$

with U as the time-evolution operator. The ionization probability reads

$$P_{g/u} = \int d\vec{k} \left|\left\langle E|\Psi_f^{g/u}\right\rangle\right|^2$$
$$= \int d\vec{k} \left[\frac{1}{2}\left|\langle E|U\Phi_A\rangle\right|^2 + \frac{1}{2}\left|\langle E|U\Phi_B\rangle\right|^2 \pm \mathrm{Re}[\langle E|U\Phi_A\rangle^* \langle E|U\Phi_B\rangle]\right], \tag{3.88}$$

where $|E>$ indicates the energy normalized molecular scattering states. Note the actual ionization probability is obtained through projecting out the bound states, as discussed in Sec. 3.1. Including scattering states here is for simplicity.

Since the broad ionization peak observed in Fig. 3.1 is for the $2p\sigma_u$ channel, we thus decompose the P_u into two components: the first one includes two absolute square terms in Eq. (3.88), which is called "single-center" component, and the second component involves the interference term in Eq. (3.88), which is called "two-center" interference component.

44

Thus the single-center component is

$$\int d\vec{k} \frac{1}{2} |\langle E|U\Phi_A\rangle|^2 + \frac{1}{2} |\langle E|U\Phi_B\rangle|^2 = \frac{1}{2}(P_u + P_g), \tag{3.89}$$

while the two-center interference component is

$$\int d\vec{k} - \text{Re}[\langle E|U\Phi_A\rangle^* \langle E|U\Phi_B\rangle] = \frac{1}{2}(P_u - P_g). \tag{3.90}$$

These two components in P_u are shown in the lower pannel in Fig. 3.1, where one can see the single-center contribution is fairly structureless as one might expect since it approximates the atomic ionization. The strong interference in P_u over all range of R mainly comes from the two-center interference. Moreover, the broad ionization peak at $40 \lesssim R \lesssim 60$ a.u. remains in the two-center component. We thus conclude that the broad peak of ionization at large R for the ungerade initial state is attributed to strong-field two-center interference effect. Note that the broad ionization peak in ungerade state is accompanied by a suppression in the gerade state.

To have a detailed picture of the strong-field two-center effect in molecular ionization of H_2^+ in Fig. 3.2 — on the 2nd row — we show the photoelectron spectrum as a function of internuclear distances for both initial symmetries, below which the total yields are shown for comparison. For the low energy spectrum, one can clearly see three different photon bands evolve as a function of R. It is due to the change in the ionization potential. By comparing the total yield and the photoelectron spectrum, it is not difficult for one to tell that the interference pattern in the total yield mainly comes from the low energy spectrum, where most of the ionization peaks in P_g/P_u correspond to peaks in the first photon band of the photoelectron spectrum.

To directly distinguish the strong-field two-center interference from the one-photon two-center interference, we extracted the interference term in the Cohen and Fano's picture — $1 + \sin kr/(kr)$ — as plotted on the top panel in Fig. 3.2. Remarkably, the simple "strip" structure in one-photon two-center interference can still be seen in the strong-field calculation, which is marked by a series of black curves on the "strong-field" low energy spectrum for $1s\sigma_g$ state. Similar structure can also be found for $2p\sigma_u$ state. This also confirms that the interference pattern in the photoelectron spectrum does exist for strong-field molecular ionization at fixed R. Besides the "strip" structure, it is difficult to find more commonality between these two. Due to highly nonperturbative processes, the strong-field two-center interference bears much more complicated features, e.g. "strip" structures are coupled with each other and hard to distinguish.

Two-center interference in the independent-atom model

The intriguing dynamics in Fig. 3.1 can be attributed to the strong-field two-center effect, which intrinsically involves two mechanisms: two-center interference and two-center dynamics. Generally, when it comes to two-center interference, one refer to the Young's
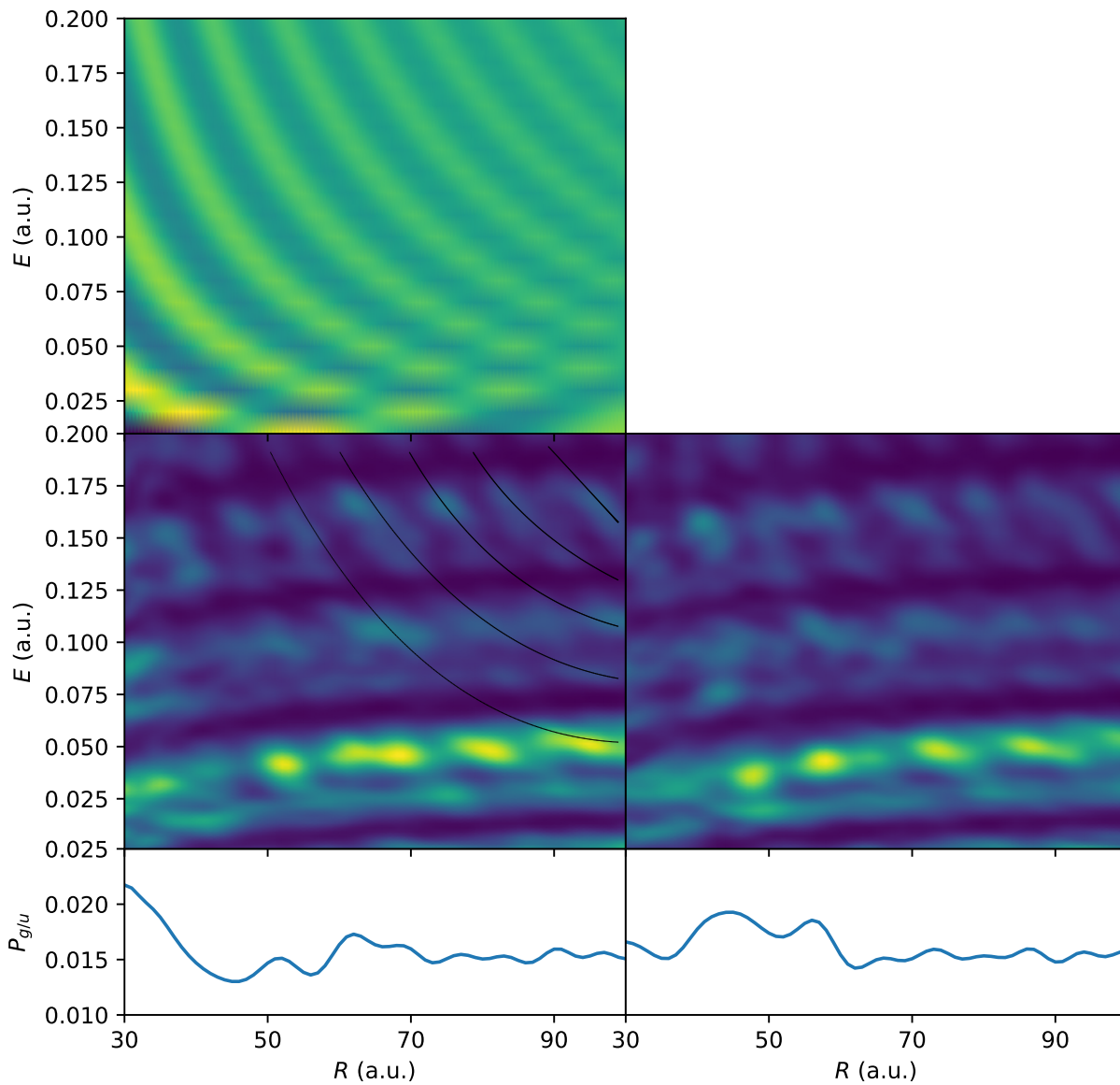
Figure 3.2: *Low energy spectrum (2nd row) and the total ionization yield (3rd row) calculated by TDSE as a function of R for a Gaussian pulse with the FWHM of 10 fs, an intensity of 10^{14} W/cm^2, and the wavelength of 780 nm, and the low energy spectrum as a function of R extracted from Cohen and Fano's picture (1st row), for initial state $1s\sigma_g$ (left) and $2p\sigma_u$ (right).*

double-slit experiment, where the waves produced from two separated sources interfere with each other as they propagate, generating an interference pattern. In such a picture, there are no dynamics involved, i.e. one wave — as it propagates — does not interact with the other source. For the molecular double slit, however, things are more complicated. The electronic wavepacket generated from one atomic center, with the assistance of the laser field, most likely will interact with the other center. For H_2^+, specifically, the electronic wavepacket ionized from one proton could interact with the other proton during the field, producing complicated two-center dynamics. For example, electronic recombination can occur where the electronic wavepacket is driven back to the bound states during the interaction with the other center. Normally, such a two-center dynamics is not quite distinguishable from the commonly understood two-center interference, especially in experiments, given no observables exist to distinguish these two processes.

However, here we propose a case which is closest to the normal two-center interference where the atomic ionization at two centers separated by R are superposed—in-phase or out-of-phase—to mimic the diatomic molecular ionization. The in-phase superposition matches the $1s\sigma_g$ scenario while the out-of-phase one matches $2p\sigma_u$ for H_2^+. In such a model calculation, the final wavefunction reads

$$|\Psi(t_f)_{g/u}\rangle = |\Phi_A^{\mathrm{a}}(t_f)\rangle \pm |\Phi_B^{\mathrm{a}}(t_f)\rangle = U_A^{\mathrm{a}}(t_f, t_i)\,|\Phi_A^{\mathrm{a}}(t_i)\rangle \pm U_B^{\mathrm{a}}(t_f, t_i)\,|\Phi_B^{\mathrm{a}}(t_i)\rangle, \qquad (3.91)$$

where $U^{\mathrm{a}}(t_f, t_i)$ are atomic time evolution operator and $|\Phi_{\mathrm{A/B}}^{\mathrm{a}}(t_i)\rangle$ is the ground state of atomic H located at center A/B. The total ionization yield is then obtained by projecting the final state onto the molecular scattering states, as in the case of full two-center calculation above,

$$P = \int d\vec{k}|\,\langle E|\Psi(t_f)_{g/u}\rangle\,|^2$$
$$= \int d\vec{k}\left[\frac{1}{2}\,|\langle E|\Phi_A^{\mathrm{a}}(t_f)\rangle|^2 + \frac{1}{2}\,|\langle E|\Phi_B^{\mathrm{a}}(t_f)\rangle|^2 \pm \mathrm{Re}[\langle E|\Phi_A^{\mathrm{a}}(t_f)\rangle^* \langle E|\Phi_B^{\mathrm{a}}(t_f)\rangle]\right]. \qquad (3.92)$$

In this case, the electronic wavepacket generated from two centers interfere with each other, as in the normal two-center interference. Since there is no other center involved during the ionization, the wavepacket produced from one-center does not interact with the other center, thus preventing the two-center dynamics.

The total ionization yield is shown in the upper panel in Fig. 3.3. By comparing such model for molecular ionization to the one shown in Fig. 3.1, one can tell that they both share strong symmetry dependence, i.e. yields with different symmetries oscillate as a function of R in the opposite direction. Otherwise, there are basically no common characteristics between the two. The overall shapes in two cases are quite different. There are much more oscillation structures in Fig. 3.3. The lack of correlation between the model ionization yield and the full two-center ionization yield indicates that the two-center dynamics play a significant role in the ionization process. This also suggests that the standard way to think about two-center interference in homonuclear diatomic molecular ionization is not enough
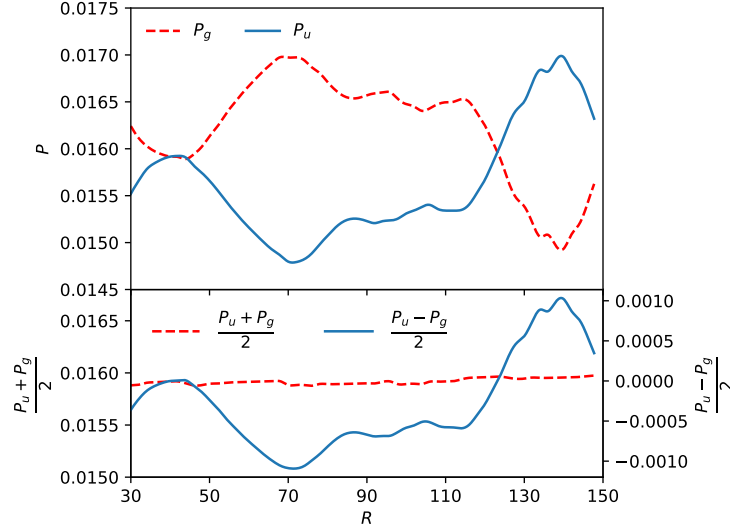
Figure 3.3: *Upper: total ionization yield obtained by superposing—in-phase or out-of-phase—the atomic ionization—with laser parameters as in Fig. 3.1—separated by R to mimic the two-center interference without two-center dynamics involved. Lower: decomposition of P_u.*

when strong fields are involved. The two-center dynamics should be taken into account.

The lower panel in Fig. 3.3 shows the decomposition of P_u as in the Fig. 3.1. One might notice that the average of P_g and P_u are basically flat within the accuracy level of calculations, and the average ionization yield (≈ 0.0159) matches well with the "asymptotic" value at $\tau = 300$ fs in Fig. 3.1. This agreement actually confirms the expectation that the "single-center" component in the ionization of H_2^+ approximates the atomic ionization yields.

Short-range potential

We have shown surprising strong-field two-center effect for the ionization of H_2^+ at large R. Being a Coulomb system, one might think this is due to the long-range Coulomb effect. In this section, however, we perform the same study but replacing the Coulomb potential with a short-range Yukawa potential in the form

$$V(r) = -\frac{e^{-0.1r}}{r}, \tag{3.93}$$

where r is the distance between electron and nuclei. In Fig. 3.4, we show the ionization yield as a function of R for initial electronic states $1s\sigma_g$ and $2p\sigma_u$ (P_g and P_u), as well as the decomposition of P_g. In general, the ionization behavior for the short-range potential is similar to that for Coulomb potential. Strong oscillations as a function of R can still be found in systems with short-range potentials. Ionization yields with different initial symmetries oscillate in the opposite direction. Moreover, the interference gradually decays with

48
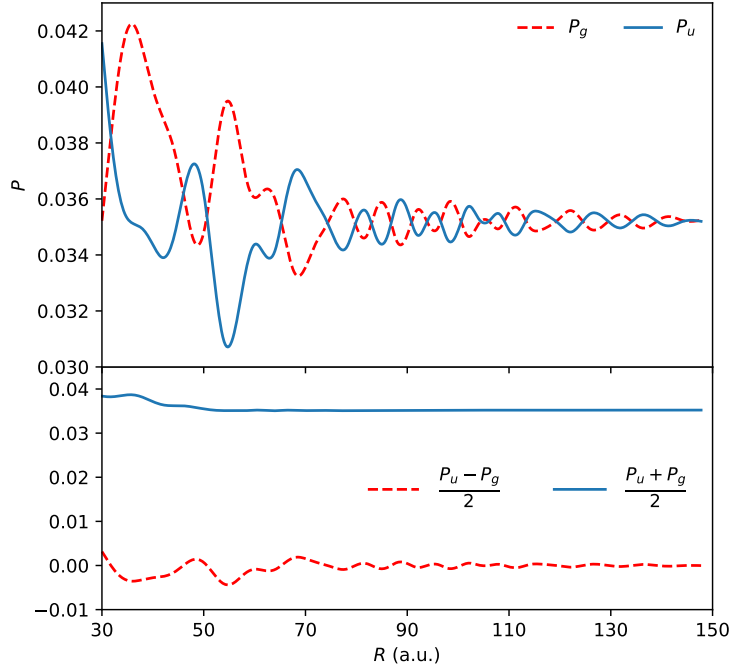
Figure 3.4: *Upper: ionization probability — calculated using laser parameters as in Fig. 3.1 — as a function of R for short-range potentials for gerade (P_g) and ungerade (P_u) initial states. Lower: decomposition of P_u.*

increasing R. The difference though, lies in the details of the structure in the ionization yield, e.g. peak positions, peak width, etc.. Note that for the particular Yukawa potential we choose, seeing complicated structures along the R range in Fig. 3.4 is even more surprising since the two centers are completely separated, with sizes of the bound states much less than R. Therefore, the strong-field two-center effect presented here is independent of whether the system is Coulombic or not, which makes the result more generalizable to larger systems, which typically involve interactions more complicated than Coulomb, such as atomic clusters.

3.2.2 Two center induced CEP effect: heteronuclear diatomic molecules

To investigate the strong-field two-center effect in a heteronuclear molecule, we study the R-dependent ionization yield for HD^+, where the initial state is centered at either the proton or the deuteron. Note that since the nuclei are fixed, there is no mass effect on the ionization yield. Therefore, the proton and deuteron are essentially the same, and will be labeled by A and B in the following discussion. The only difference though between ionization of HD^+ and ionization of H_2^+ with fixed internuclear distance is the initial state.

49
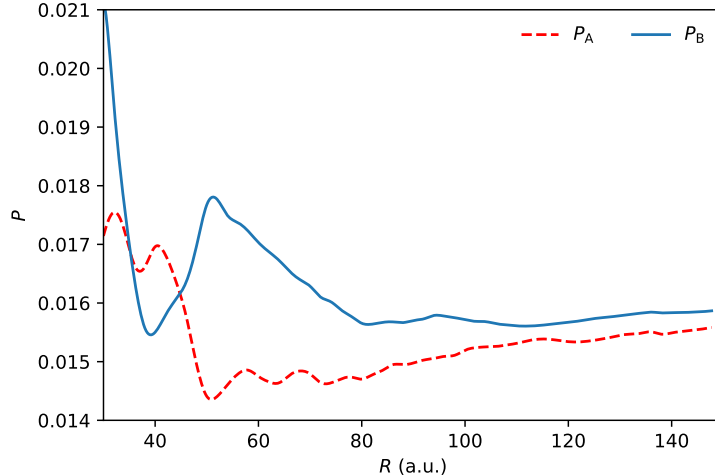
Figure 3.5: *Ionization probability as a function of R for initial state centered at A and B respectively.*

For HD^+, the initial states are obtained by superposing g and u states of H_2^+

$$\Psi_{A/B} = \Psi_{1s\sigma_g} \pm \Psi_{2p\sigma_u}. \tag{3.94}$$

Such difference, however, captures one of the key heteronuclear characteristics of HD^+: $H+D^+$ or H^++D, assuming the molecule is oriented.

In Fig. 3.5, we show the R-dependent ionization yield for HD^+. One interesting observation is that much less interference is found in the R-dependent yield for HD^+ than that for H_2^+, which indicates that the two-center dynamics are less involved in HD^+ than H_2^+ given that the fine oscillations, as discussed in Sec. 3.2.1, are attributed to the two-center dynamics. One should note the results in Fig. 3.5 are exactly the two components: $P_A = \int d\vec{k}\frac{1}{2} |\langle E|U\Phi_A\rangle|^2$ and $P_B = \int d\vec{k}\frac{1}{2} |\langle E|U\Phi_B\rangle|^2$ in Eq. 3.88, which is also two components of $(P_g + P_u)/2$ in Fig. 3.1.

Different from the case of H_2^+, where strong symmetry dependence of ionization is found, the symmetry for the initial electronic states is broken for heteronuclear HD^+. For large R, one typically would not expect any effects of the initial state on the ionization yield of HD^+ since the yield in CW lasers should be invariant to initial electronic localization. Surprisingly, as seen in Fig. 3.5, the total ionization yield still depends on the initial state. For instance, 20% contrast is found for the yield at $R \approx 50$ a.u.. Furthermore, we found this strong initial-state dependence is due to the CEP effect, which is not so expected in such case. Because for 800 nm, the CEP effect for such a long pulse — with a FWHM of 10 fs — is negligible for photodissociation of H_2^+ [36]. We thus do not expect it to play a significant role in the ionization of H_2^+, which is in fact confirmed by doing calculations in Fig. 3.1 with different CEP's. However, by checking the CEP dependence of the ionization yield of HD^+ we found the initial-state dependence of the ionization yield is essentially the CEP dependence, i.e., the yield corresponding to initial-localization on one center approximates

the yield for initial-localization on the other center, but with a CEP differed by π. Further, such CEP dependence becomes weaker with increasing pulse length, e.g. the 20% contrast at $R \approx 50$ a.u. in Fig. 3.5 drops to few percent for a longer — 20 fs — pulse. This is expected since again there should not be any CEP effect in the CW-laser induced ionization. Given that such a CEP effect is due to the two-center nature of the molecule, we call it the two-center induced CEP effect. Note that by confirming such two-center induced CEP effect in
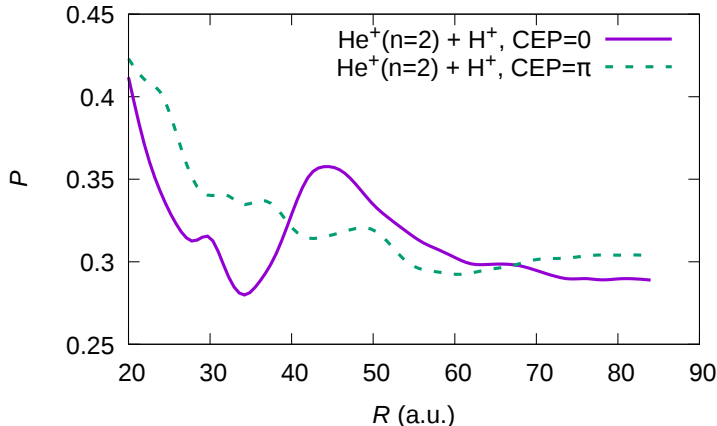
Figure 3.6: *Ionization probability as a function of R for HeH^{++} with initial state $He^+(n=2)+H^+$, and CEP of 0 and π. The laser parameters are the same as for HD^+.*

another heteronuclear molecule, i.e. HeH^{++} as shown in Fig. 3.6, we thus expect it to exist in other heteronuclear systems, which do require oriented molecules.

To examine contributions other than the two-center induced CEP effect in Fig. 3.5, CEP averaging is necessary. Here we direct the readers to Fig. 3.1, where the component $(P_g + P_u)/2$ is simply a two-points $(0,\pi)$ CEP averaging of the ionization yield for certain initial electronic localization. One could tell, after the CEP averaging, that the two-center interference almost disappears at large R, which again indicates that there are negligible two-center dynamics in heteronuclear diatomic molecular ionization.

3.3   Summary

To summarize, we have investigated molecular ionization at large internuclear separations and surprisingly discovered two classes of strong-field two-center effects. Specifically, we have shown a strong symmetry-dependent two-center interference in photoionization of homonuclear diatomic molecules and the two-center induced CEP effect for heteronuclear diatomic molecular ionization, both in terms of the total ionization probability. Even though we mainly study a specific molecule—H_2^+/HD^+—in this work, we do expect such strong-field two-center effects to be carried over to other diatomic systems and potentially be observed in multi-center physics. Due to the two-center dynamics, such strong-field two-center effects could lead to system-dependent features, e.g. broad ionization peak at large R in H_2^+, which

could potentially be measured in practical experiments. Discussions about the application of the strong-field two-center effects in experiments will be presented in Chapter 5.

Chapter 4

Low energy structure in strong-field ionization

The advance of producing few-cycle pulses of infrared wavelengths in experiments has accelerated the investigation of strong-field ionization in atoms and molecules at laser wavelength longer than 1 μm [122]. The general understanding of the photoelectron spectra involves the "direct" and "rescattered" electrons. The "direct" electrons are ionized and driven by the laser field without re-entering the parent ion and gain a kinetic energy up to twice the ponderomotive energy (U_p). This is what contributes to the low energy spectrum. Some electrons — moving in the field — may re-collide with the parent ion, thus gaining more energy – up to $10U_\mathrm{p}$. They are called "rescattered" electrons. The energy span from $2U_\mathrm{p}$ to $10U_\mathrm{p}$ is thus the "plateau" in the photoelectron spectra [83, 84]. According to the classical tunneling model [123], the spectrum for "direct" electrons should smoothly decay at small photoelectron energies. When it goes to long wavelength regime (>1 μm), the classical model should be more appropriate to describe the photoelectron spectra than that in the standard Ti:sapphire laser (wavelength=780 nm). Surprisingly, more recent studies [85, 124] reported a remarkable peak structure at low energy — normally about few eV — in in the photoelectron spectra — called the low energy structure (LES) — contradicting the understanding of the "direct" electrons in the classical picture.

Previously, the LES has been measured in experiments for molecular ionization, typically as shown in Fig. 1 in Ref. [85], where a peak-like structure is shown at low photoelectronic energy ($\lesssim 6$ eV). Similar LES are normally expected for atomic and molecular ionization with laser wavelengths ranging from 1 μm to 3 μm and intensity ranging from tens of TW/cm^2 to hundreds of TW/cm^2.

In this chapter, we will present, for the first time, an *ab initio* study of molecular LES by solving the 3D time-dependent Schrödinger equation. The wavelength dependence, initial-symmetry dependence as well as dimensionality dependence of the LES will be discussed. Note that the results shown in this chapter are preliminary and still in progress.

4.1 Molecular low energy structure

We solve the full-dimensional TDSE for H_2^+ using methods discussed in Sec. 3.1. The final wave function at the end of the pulse is analyzed by applying the energy analysis documented in Sec. 3.1.6. In fact, at the first attempt, the photoelectron energy distribution was obtained by field-free propagating the final wave function of the TDSE — where the bound states are projected out — followed by a autocorrelation or a Fourier transform to momentum space. This approach in principle seems smooth and easy. Nevertheless, we found various numerical issues in the practical implementation, for example the numerical integral involving fast oscillations in the Fourier transform is barely accurate and the selection of the Fourier transform window is tricky. Even though, we managed to get the photoelectron spectrum eventually. It can only reproduce the result for certain perturbative test example. The accuracy cannot be guaranteed for all kinds of spectra and is rather unstable. We thus move to the complicated yet exact analysis scheme, as discussed in Sec. 3.1.6.

Since the molecular ionization could be dramatically enhanced at critical distance [4, 5], we choose the internuclear distance R=10 a.u., where the molecular nature could potentially be maximized. For laser parameters, we select wavelengths of 1200 nm and 1600 nm, an intensity of 10^{14} W/cm^2 for a Gaussian pulse with a FWHM of 2 optical cycles, or 8 fs for 1200 nm and 10 fs for 1600 nm. As presented in Sec. 3.2.1, the diatomic molecular ionization bears a strong initial-symmetry dependence. We thus include different initial symmetries—$1s\sigma_g$ and $2p\sigma_u$—as well in the discussion.

In Fig. 4.1, we show the normalized photoelectron spectrum at low electronic energy for H_2^+. One can see that the calculated photoelectron spectrum for H_2^+ with fixed R at long wavelength shows clear ATI peaks with dramatic oscillation amplitude. Such pronounced ATI peaks however might either not show up or show up with a much weaker oscillation amplitude in practical experiments. This could be attributed to the finite width of the nuclear wave function. Assume molecular ionization mainly occurs at small internuclear distances in experiments where the ionization potential could change dramatically for different R, therefore averaging the photoelectron spectrum for different internuclear distances would probably wash out the ATI peaks. Another reason comes from the bandwidth of the pulse. A shorter pulse typically would reduce the oscillation amplitudes of the ATI peaks.

The existence of the ATI peaks in the spectrum, however, makes it difficult to identify the LES. To resolve such issue, we smooth the photoelectron spectrum with a Gaussian kernel. The smoothed spectrum is written as

$$\bar{P}(E') = \int dE P(E) \frac{1}{\sqrt{2\pi\Delta E}} e^{-\frac{(E-E')^2}{2\Delta E^2}} \tag{4.1}$$

where $P(E)$ is the actual photoelectron spectrum and ΔE equals $\hbar\omega$. As shown in Fig. 4.1, the smoothed spectrum follows the overall shape of the actual photoelectron spectrum, as it should be. By examining the smoothed spectra in Fig. 4.1, one could clearly see peak-like structures at low photoelectron energies (few eV), i.e. the LES are found in the molecular photoelectron spectra. It is true for different symmetries, and different wavelengths consid-
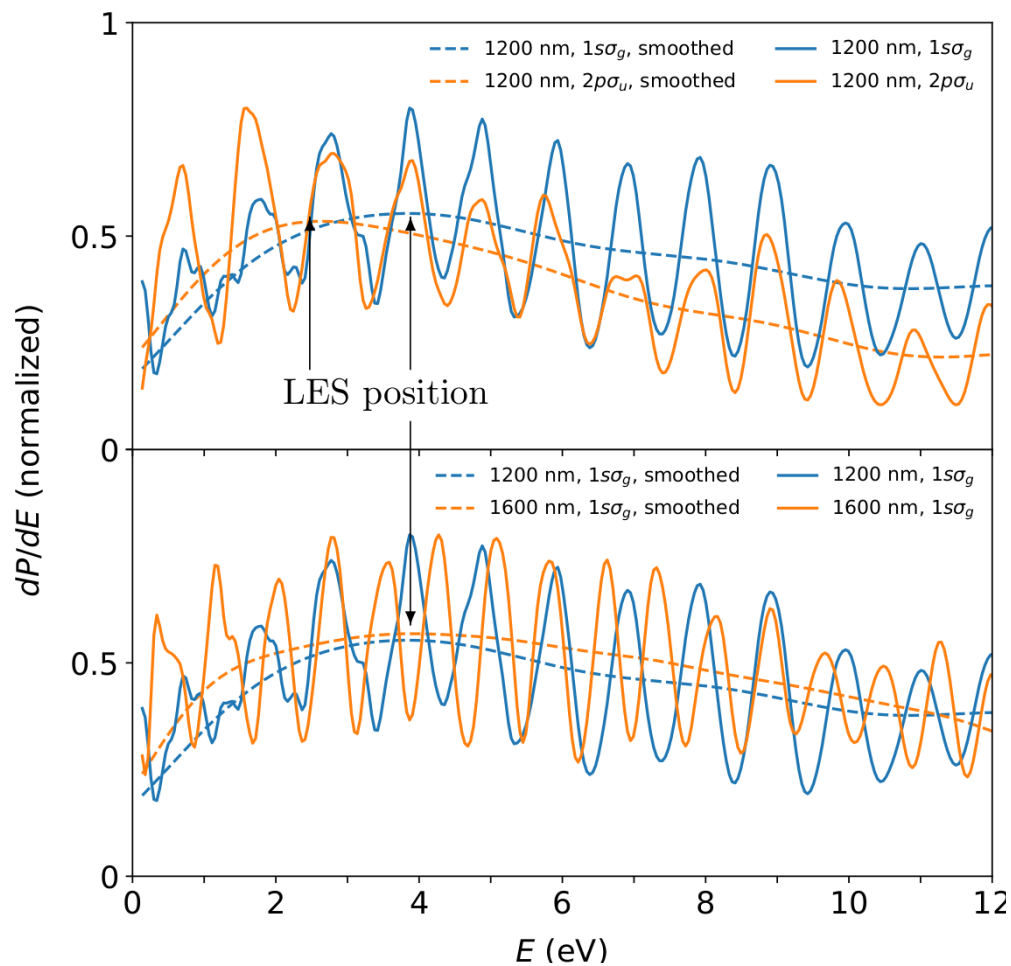
Figure 4.1: *Comparison of the photoelectron energy distribution for H_2^+ for different initial states (upper), and for different wavelength(lower). The photoelectron energy distributions are normalized so that the maximum value is 0.8. Dashed lines indicate photoelectron spectra smoothed with Gaussian kernels (see text for details).*

ered in this work. The position of the LES can also be readily identified in the smoothed spectra, which are indicated by arrows in Fig. 4.1. One can easily see, in the upper panel, the position of the LES for $2p\sigma_u$ ($\sim$2 eV) somewhat moves to a smaller energy than that for $1s\sigma_g$ ($\sim$4 eV). This might be due to the strong-field two-center effect, as discussed in Sec. 3.2.1, but exact explanation is still not clear.

In general, the position of the LES does depend on the pulse shape [85, 125]. We thus move to the lower panel in Fig 4.1 for different wavelengths, where both 1200 nm and 1600 nm with a $1s\sigma_g$ initial state shows a peak structure at small energy, around 3–4 eV. The overall shape of the LES is similar in both cases, especially the position of the LES. One should note though that the LES for 1600 nm is broader than that for 1200 nm, which coincides with previous experiments of atomic LES [85].

A quantum-orbit—or saddle-point—study [125] of the LES, including the Coulomb effect, suggested that the main contribution of the LES comes from the quantum trajectory where the electron's transverse/lateral momentum is reversed, which confirms the conclusion of another work [126] that the change of the electrons' transverse momenta plays a important role in the understanding of the LES. This suggests that the LES is a dimensionality-dependent phenomenon, which means at least two dimensions are required in the calculation to produce the LES.

To examine such dimensionality dependence, we solve a reduce-dimensional TDSE using the 1D solver in Sec. 6.6. The photoelectron spectrum is obtained by projecting the TDSE solution onto the energy normalized scattering states. The scattering states are numerically solved using the R-matrix formalism adapted from Sec. 3.1.6. In Fig. 4.2, we show the ATI
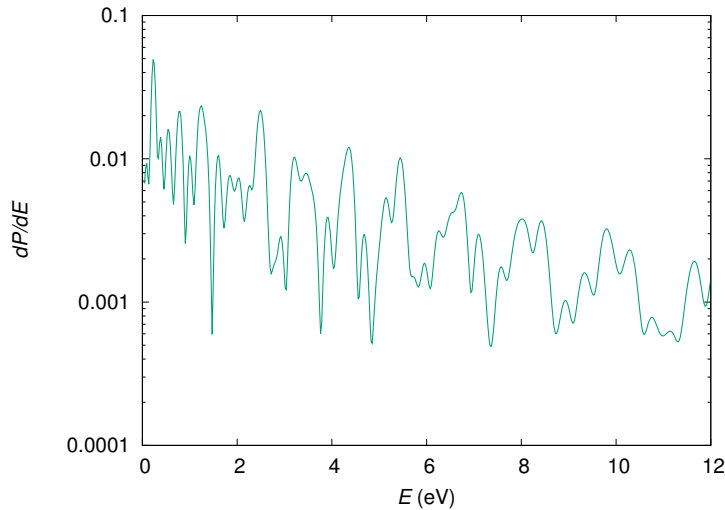
Figure 4.2: *Photoelectron energy distribution for atomic hydrogen restricted to move in one dimension for 2000 nm, 13.3 fs (2 cycles), 5×10^{13} W/cm^2, with ground initial state.*

spectrum for one-dimensional hydrogen at low energy. Overall, one can see the ATI peaks smoothly decrease without any pronounced peak structure at low energy, which differs from the 3D calculation. (See Fig. 4 in Ref. [85] for a 3D calculation of the LES for argon.) This

is expected and consistent with previous studies [125, 126] stated above. Note that there are no clear ATI peaks in Fig. 4.2. This might be an artifact of the 1D model. Generally, atoms are much easier to ionize in 1D than that in 3D, thus could potentially produce artificial nonlinearity in the photoelectron spectrum.

To examine the dimensionality dependence of the molecular ionization in Fig. 4.1, a 1D calculation with similar laser parameters is underway.

4.2 Future works for molecular LES

Due to the sensitivity of molecular ionization to the internuclear distance, either at critical distance or at large R, it would be interesting to see how the LES evolves as a function of R. Specifically, such picture will provide an answer to the question: how does the strong-field two center effect influence the LES? Such a question among others will be addressed in future works.

Chapter 5

Pump-probe study of dissociative ionization of hydrogen molecular ions

As one of the simplest techniques to directly probe electronic and nuclear dynamics on different time scales, pump-probe spectroscopy is widely used to study ultrafast molecular structure and dynamics [77–82, 127–130]. In particular, for diatomic molecular ionization, the pump-probe approach — see Ref. [77, 81] for two examples — has been successfully used to observe enhanced ionization at critical distances [4, 5].

As discussed in Chapter 3, we have found pronounced strong-field two-center effects at large internuclear distances for the differential as well as the integral observables in molecular ionization, providing a new mechanism for the time-resolved dissociative dynamics in laser-matter interactions. In this chapter, we will perform a pump-probe study of dissociative ionization of both homo- and hetero-nuclear diatomic molecules, comparing theory with practical experiments. In the pump-probe scheme, a weak pump pulse is first applied to dissociate the molecule generating a dissociating wavepacket sitting on the $2p\sigma_u/2p\sigma$ channels for H_2^+/HD^+ through one-photon dissociation. This is followed by a probe pulse delayed by τ which ionizes the dissociating wavepacket. Large delays—typically in hundreds of femtoseconds—thus qualitatively correspond to the large internuclear separations. It is based on the fact that the pump pulse is selected to generate a relatively narrow wavepacket in space, i.e. with a width of about 10 a.u..

The work in this chapter together with Chapter 3 will appear in our work [92].

5.1 Two-channel dissociation through 3D time-dependent Schrödinger equation

To calculate the dissociating wavepacket, we solve the 3D time-dependent Schrödinger equation for H_2^+/HD^+ using methods described in our previous works [104, 116, 131]. Here a brief summary is provided for completeness. First, the BO potentials and dipole matrix elements are calculated using the formulation in Ref. [104]. Then, the total wave function $\Psi(\boldsymbol{R}, \boldsymbol{r}, t)$ is expanded on the BO basis, and the nuclear rotation is treated via an expansion

over symmetrized Wigner D-functions, which reduce to spherical harmonics in this work. For our pulse parameters, retaining only the $1s\sigma_g$ and $2p\sigma_u$ channels is a good approximation [116]. In this case, both the Coriolis and non-Born-Oppenheimer couplings are zero. The TDSE thus reduces to the coupled radial equations

$$i\frac{\partial}{\partial t}F_\alpha = \left(-\frac{1}{2\mu}\frac{\partial^2}{\partial R^2} + \frac{J(J+1)}{2\mu R^2} + U_\beta\right)F_\alpha - \boldsymbol{\mathcal{E}}\cdot\sum_{\alpha'}\boldsymbol{D}_{\alpha\alpha'}F_{\alpha'}, \tag{5.1}$$

where $F_\alpha = F_\alpha(R,t)$ is the nuclear radial wave function. The index α collectively represents the quantum numbers βJM with J and M the total orbital angular momentum and its lab-frame z-projection, respectively, and β the electronic channel label, in this work, $\beta = 1s\sigma_g, 2p\sigma_u$ for H_2^+ or $1s\sigma, 2p\sigma$ for HD^+. Note that non-Born-Oppenheimer terms—see Ref. [104] for details—are included in Eq. (5.1) for HD^+. The precise form of the dipole matrix elements $\boldsymbol{D}_{\alpha\alpha'}$ is given in Ref. [116]. We use a Gaussian pulse polarized along the lab-frame z-direction, as for the probe pulse, with a full width of the intensity at half maximum τ_{FWHM} of 20 fs, a wavelength of 780 nm, and a intensity of 1×10^{13} W/cm^2.

To solve Eq. (5.1), we use the 5th-order B-Splines on a WKB grid for the radial coordinate, and the iterative method described in Ref. [115] and Sec. 3.1.3 for the time evolution [113]. The WKB grid uses 5 splines per WKB wavelength, with a maximum energy of 0.15 a.u. resolved. The grid extends from R=0.5 a.u. to R=200 a.u.. Time evolution starts at $t_{\min}$ when the pulse envelope first reaches 10^8 W/cm^2 and ends at t_f when it reaches 10^6 W/cm^2, with a time step of 0.02 a.u.. The probability density is calculated every 10 fs from τ=0 to τ=300 fs. All the dissociation results shown in this work are tested to be converged to at least 4 significant digits.

5.2 Convolution from R to delay

With the dissociating wavepacket calculated as a function of R and τ, we then perform the convolution from the R-dependent ionization yield for H_2^+/HD^+—shown in Chapter 3—to the τ-dependent yield. The final wave function at the end of the probe pulse is written as

$$\Psi_f = \sum_{J\beta} F_{vJ\beta}(R,\tau)Y_{J0}(\theta)\Phi_\beta^f(R;\boldsymbol{r},t) \tag{5.2}$$

where v indicate initial vibrational state, $\Phi_\beta^f(R;\boldsymbol{r})$ is the final electronic wave function with nuclei fixed for the initial electronic state β. Note that we assume frozen nuclei during the ionization. Therefore, in Eq. 5.2, only $\Phi_\beta^f(R;\boldsymbol{r},t)$ propagates in the probe pulse. The total ionization yield as a function of R and τ, therefore, is written as:

$$P_v(R,\tau,\theta=0) = \int dE|\sum_{J\beta}F_{vJ\beta}(R,\tau)Y_{J0}(\theta)\langle E|\Phi_\beta^f(R;\boldsymbol{r})\rangle|^2 \tag{5.3}$$

where $|E>$ is the energy normalized scattering state with fixed nuclei. Note the angular cut for θ has been taken — $\theta = 0$ — along the laser polarization since nuclear angular information is not available in calculations for the ionization process. However, we do not expect such approximation to make a qualitative change for the final observables. Because first, the field-free rotational dynamics effect after the pump pulse is small ($\sim$4%). (See panel (b) in Fig. 5 in Ref. [132]), and second we estimate pump-pulse induced alignment to be $<\cos^2\theta> \approx$ 0.5x, with which we do not have special expectation that the angular cut — or isotropic assumption — will not work.

For H_2^+, there is only one channel involved in the dissociation process, namely $2p\sigma_u$ or u. Eq. (5.3) can thus be simplified,

$$P_v(R, \tau, \theta = 0) = |\sum_J F_{vJu}(R, \tau)Y_{J0}(\theta)|^2 \int dE |\langle E|\Phi_\beta^f(R; \boldsymbol{r})\rangle|^2 \tag{5.4}$$

The total yield as a function of τ can be obtained by integrating over R in Eq. (5.4) and averaging the initial vibrational states with the Franck-Condon distribution,

$$P(\tau) = \sum_v FC_v \int dR P_v(R, \tau, \theta = 0) \tag{5.5}$$

where FC_v is the Franck-Condon factor for initial vibrational states.

For HD^+, however, the heteronuclear nature does complicate things. First, due to non-adiabatic couplings between the $1s\sigma$ and $2p\sigma$, both channels are populated during the dissociation. Thus Eq. (5.3) can not be simplified. The τ-dependent ionization yield is obtained through Eq. (5.5) but with $P_v(R, \tau, \theta = 0)$ evaluated directly from Eq. (5.3). Second, the two-center induced CEP effect on the R-dependent ionization yield, as discussed in Chapter 3, indicates that a CEP averaging is necessary for HD^+. We thus perform a two-point — $\varphi = 0, \pi$ — CEP averaging for τ-dependent yield in Eq. 5.5.

Also, by assuming an isotropic angular distribution of the dissociating wavepacket, the orientation effect must be taken into account for HD^+, which is not an issue for H_2^+. Fortunately, the orientation averaging — $\theta = 0, \pi$ — in this case coincides with the two-point — $\varphi = 0, \pi$ — CEP averaging. Therefore, after the CEP averaging, the orientation effect no longer exists.

In Fig. 5.1, we show the τ-dependent ionization probability for both H_2^+ and HD^+. Surprisingly, we see broad ionization peaks at large delay — from about 120 fs to 220 fs — for both cases. The peak of the ionization yield is about 10%$\sim$15% higher than the yield at $\tau = 300$ fs, the largest delay considered in this work. The broad peak in the ionization yield for HD^+ is shifted to larger delays than that for H_2^+ due to the heavier mass moving slower. For H_2^+, it is not difficult to connect the broad ionization peak at large delay in Fig. 5.1 to that at large R for P_u in Fig. 3.1. However, the strong-field two-center interference in R-direction does not survive in the τ-dependent ionization yield, partially due to the finite width of the dissociating wavepacket, which is comparable to the oscillation period in R-dependent yield. Also the Franck-Condon averaging, to some extent, helps wash out the
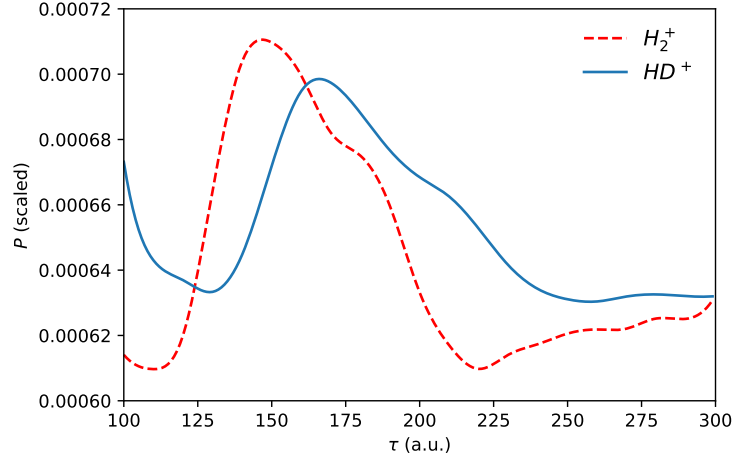
Figure 5.1: *Ionization yield as a function of pump-probe delay τ for H_2^+ and HD^+.*

interference pattern in the convolution.

For HD^+, surprisingly, the broad ionization peak remains even though both channels are involved in the ionization process due to non-adiabatic couplings. Coherent superposition of the two channels are carried out in the convolution from R to τ. The observation of the final time-resolved ionization yield possessing a broad peak in HD^+ might be attributed to the strong-field two-center effect in general. Yet, the details are unclear. This should be regarded as an open question for the readers.

5.3 Comparison with experiments

The pump-probe experiment for the dissociative ionization of HD^+ was done by Dr. Ben-Itzhak's group at J.R. Macdonald Laboratory, Kansas State University. A detailed description of the experimental method can be found in Ref. [133]. The experiments involved linear polarized 23 fs, 790 nm pulses, and the pump- and probe-pulse intensities were 7.6×10^{13} and 3.3×10^{14} W/cm^2, respectively. In experiments, however, there are two different ionization channels during the probe: ionization of the bound electronic wavepacket and ionization of the dissociating wavepacket, where the latter one is the focus of this work. The experimental results are shown in Fig. 5.2, where signals of the nuclear ion are measured to represent the ionization yield.

By comparing the theory in Fig. 5.1 and experiments in Fig. 5.2(c), one can readily identify a broad ionization peak between 100 fs and 300 fs in both cases, which is fairly impressive given the ionization occurs at such large internuclear distances, where molecular physics is not so expected, as discussed in Chapter 3. To move beyond such qualitative agreement, we further examine the peak position of the broad ionization peak, where theory predicts $\tau \approx 170$ fs while experiment locates the ionization peak at $\tau \approx 250$ fs. We also note that the enhancement between $\tau = 100$ fs and $\tau = 300$ fs are different between experiments
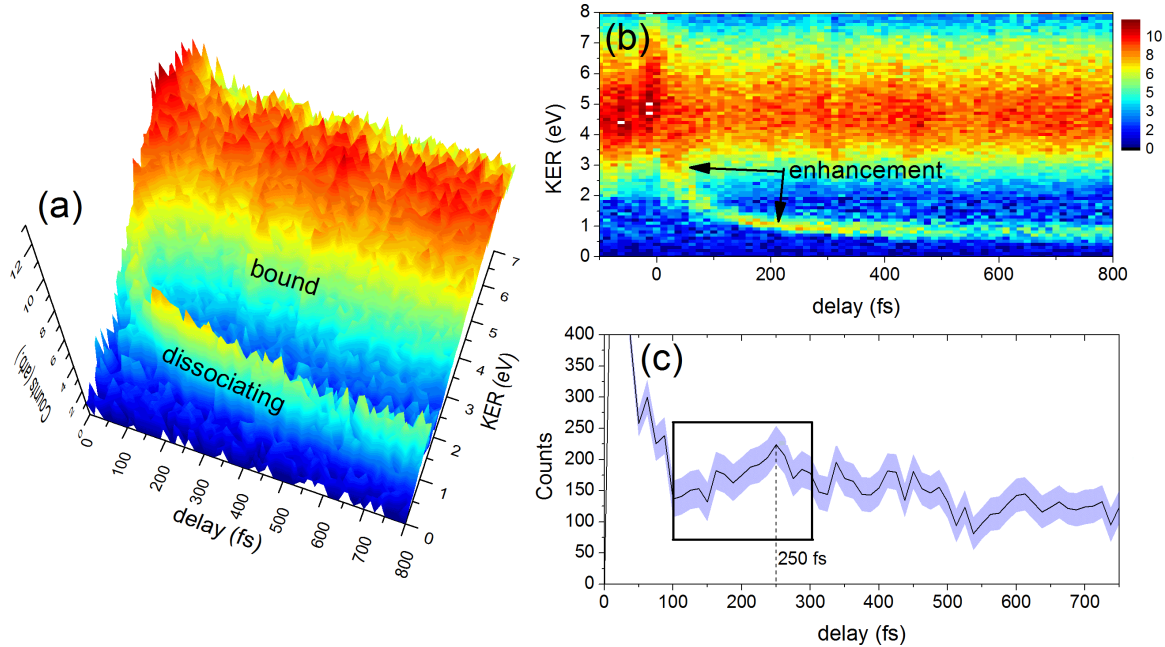
Figure 5.2: *(a,b) The yield of $H^+ + D^+$ events mapped as a function the pump-probe delay and KER. The high-KER component is due to the ionization of bound HD^+. The tail extending to lower KER is due to ionization of the dissociating HD^+ wavepacket, and it exhibits a broad enhancement around 250 fs. (c) The integrated yield in "tail" associated with ionization of the dissociating wavepacket indicates a 1.75 ± 0.33 times enhancement in the ionization of the dissociating wavepacket between 200 and 300-fs delay.*

and theory.

To explain such discrepancy, it is now a good time to review those approximations in calculations, which might provide hints for what one should expect for experiments. First, the nuclei are fixed in the ionization calculation, assuming the nuclei are moving much slower than the electron, which should be reasonable from a qualitative perspective. However, during the probe pulse—with a FWHM of 10 fs and a total propagation time of 41 fs—the nuclei could still have an appreciable displacement. We show, in Fig. 5.3, a dissociating wavepacket—on the $2p\sigma_u$ channel—for the dominant initial vibrational state $v = 9$ in H_2^+ dissociation, where different pump-probe delays are shown. One could readily notice that the wavepacket moves about 13 a.u. during the probe pulse. If the nuclear motion is included in the ionization process, we would expect the broad peak in the delay-dependent ionization yield in Fig. 5.1 to be even broader.

The second approximation in the calculation is that we do not include the nuclear angular dependence in the ionization process, where we simply take an angular cut along the laser polarization direction. This indicates that the ionization for lower effective intensity are not included in the calculation. Another intensity-relevant mismatch between experiments and theory is the intensity averaging, which is omitted due to limited computing resources. This also leads us to lower intensities. To our knowledge, changing the intensity could

shift the peak position of the ionization yield in Fig. 5.1. In fact, we have tried one other higher intensity for the ionization calculations and seen the ionization peak slightly moving to smaller τ. Our calculation also indicates that the enhancement of ionization at large τ is sensitive to the pulse length. With these factors in mind, we would therefore expect the
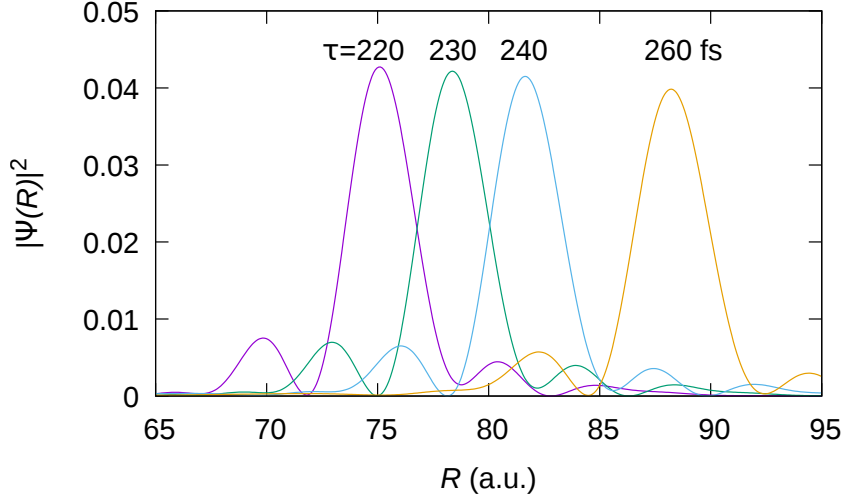
Figure 5.3: *Dissociation wavepacket on $2p\sigma_u$ channel with the initial vibrational state $v = 9$, by a Gaussian pulse with a FWHM of 20 fs, a wavelength of 780 nm, and an intensity of 1×10^{14} W/cm^2, at delay $\tau = 220$, 230, 240, 260 fs.*

width, the position and the enhancement of the ionization peak in term of τ to be different in experiments from theory, which — to some extent — explains the quantitative gap between the theory (Fig. 5.1) and experiments (Fig. 5.2)(c).

Finally, in theory — as stated above — the oscillation feature found in Fig. 3.1 is washed out in the τ-dependent yield after taking the dissociating wavepacket and Franck-Condon averaging into account. In Fig. 5.2(c), however, some oscillation structures can be found in the τ-dependent yield in the experiment, which should be attributed to the strong-field two-center effects if they are physical since the error bar in this experiment is comparable to the oscillation amplitude. We note, in principle, such strong-field two-center interference in the total yield can be measured by a sophisticated experimental apparatus, e.g. selecting a pump pulse with much smaller bandwidth—thus significantly reduced wavepacket width—in a vibronic-resolved experiment.

Chapter 6

An optimized absorbing potential for ultrafast, strong-field problems

6.1 An introduction to absorbing potentials

To theoretically describe highly nonperturbative interactions—such as strong-field physics—in a fully quantitative manner, the best option is usually to numerically solve the time-dependent Schrödinger equation (TDSE). One of the most popular approaches to practically solving the TDSE represents the wave function on a finite spatial grid with boundary conditions applied at its edges. In general, such a grid needs to be large enough so that there are no reflections from the boundaries which behave as infinitely hard walls. Otherwise, the reflections might lead to unphysical changes in the observables. For example, an ionized wavepacket reflected from the boundary back to the origin might be driven by the laser field into bound states, thus reducing the total ionization yield.

The most direct way to avoid such spurious reflections is to move the boundary further away. Since the grid density is fixed physically by the highest energy, however, this requires more grid points which, in turn, incurs a greater computational cost. In fact, the large grids required to describe current experiments have become a key bottleneck to improving the numerical efficiency of solving the TDSE, especially as laser wavelengths push beyond 800 nm.

Fortunately, if the wave function at large distances can easily be reconstructed or is not of interest, it can be absorbed at a sufficiently large distance that it does not affect the dynamics at small distances. Applying such absorption techniques, one can generally reduce the box size significantly. The absorb-and-reconstruct strategy was probably first developed by Heather and Metiu [134] which they demonstrated for strong-field dissociation. Their work has been adopted in hundreds of papers since. A new implementation following this philosophy [135, 136] has proven similarly effective.

Among the various methods to effect absorption at the boundary, the most widely used—and probably the simplest—method is the complex absorbing potential (CAP) [137–150] or the closely related masking function [151]. Another increasingly popular absorbing-

boundary technique is exterior complex scaling [152–156], where one rotates the coordinate into the complex plane at large distances. Other, less common, methods to treat the boundary reflection include time-dependent coordinate scaling [157–159], the interaction representation [160–162], and Siegert-state expansions [163]. While these methods are local in time and vary from exact to approximate, it is also possible to construct a perfectly transparent boundary using Feshbach projection techniques [146]. The disadvantage of such methods is that they require the wave function from previous times and are thus nonlocal in time. In this work, we will focus on the CAP due to its popularity and the simplicity of its implementation. Our goals are to make it both more efficient and more effective.

Although the CAPs utilized in previous studies are predominantly polynomials [141, 142, 145–147, 149, 150], other types of absorbing potentials such as $\cos^2$ [148], Pöschl-Teller $(1/\cosh^2)$[137], and a pseudo-exponential [$\exp(-x^{-n})$] [138, 139] have also been used. In most of these works, the CAP's performance is examined by studying the dependence of the reflection R and transmission T coefficients on the energy. Riss and Meyer [141], for instance, carefully investigated the properties of R and T for polynomial CAPs, finding some difficulty in treating low energies. They characterized their optimized potential parameters in terms of the absorbed energy ratio $E_{\max}/E_{\min}$, where $E_{\min}$ and $E_{\max}$ indicate the minimum and maximum energies, respectively, for which absorption exceeds a given value. The maximum ratio they considered, 30, is too small, however, for typical strong-field electronic dynamics. We will, for instance, consider $E_{\max}/E_{\min}$=500. Vibok and Balint-Kurti [138, 139] presented a more optimal CAP — the $\exp(-x^{-n})$ type — for heavy particles, but the range of absorbed energies was still insufficient for strong-field problems.

Even though R and T provide a clear, quantitative measure of performance, studies of CAPs in strong-field problems utilizing them can hardly be found. Their absence is likely due to the inherent time-dependent nature of the strong-field problem and the authors' consequent focus on wavepacket behavior, losing track of the connection with R and T. In contrast, we will adopt R as the figure of merit for designing our absorbing potentials for the strong-field problem, incorporating it as a critical piece in our systematic CAP construction method.

The major advantage of the CAP is its simplicity. The major disadvantage is that it has required a relatively large spatial range to be effective, thus consuming non-negligible computational resources. In this chapter, we improve the performance of the CAP and systematically design a more optimal — yet general — CAP for strong-field processes. Specifically, we provide an optimized CAP with a factor of 3–4 reduction in the absorption range compared to some widely-used CAPs [146]. Our optimized CAP absorbs at a prescribed level over a large enough energy range to be useful for strong-field processes.

To be clear, while we optimize our CAP for the strong-field problem, it can be readily adapted and re-optimized for other problems following the procedures we outline below.
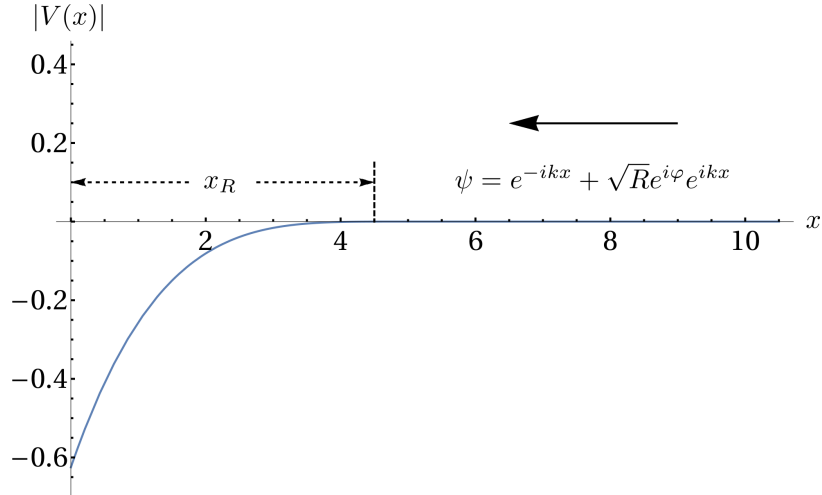
Figure 6.1: *The scheme used to characterize a CAP and determine its reflection coefficient. The edge of the grid is taken to be $x = 0$, and we require $\psi(x{=}0) = 0$ as is typical in solving the TDSE. We assume incidence from the right as indicated. We define the absorption range x_R from the distance at which the absorbing potential decreases beyond a cutoff value V_c and can be neglected, $|V(x_R)| = V_c$.*

6.2 Theoretical background

Since a time-dependent wavepacket can always be written as a superposition of the time-independent scattering states, we use the time-independent reflection coefficient as a quantitative tool for characterizing and designing an optimal CAP. We will require the CAP's reflection coefficient to remain below a cutoff value R_c, $R \leqslant R_c$, over a given energy range $E_{\min} \leqslant E \leqslant E_{\max}$. Since the spatial region devoted to the CAP near the edge of the grid is unphysical, we wish to minimize the computing resources it consumes as much as possible. Therefore, in this work, our optimization efforts focus on reducing the absorption range x_R, as defined in Fig. 6.1, while meeting the absorption criteria above.

We study one-dimensional CAPs since they can be easily adapted to higher dimensions, obtaining the reflection coefficient R by solving the Schrödinger equation,

$$\left[-\frac{\hbar^2}{2m} \frac{d^2}{dx^2} + V(x) \right] \psi = E\psi, \tag{6.1}$$

as indicated schematically in Fig. 6.1. We consider the potential $V(x)$ to be one of the CAPs listed in Table 6.1. The shapes of all the CAPs considered are generically as in Fig. 6.1 and are controlled by the following parameters: α^2 is the strength of the potential, β mainly determines its width, and x_0 is a shift. These are the parameters that will be varied to optimize the CAPs.

The JWKB-based CAP obtained by Manolopoulos [144] — labeled M-JWKB in Table 6.1 — is qualitatively different from the others, however, in that it requires no opti-

Table 6.1: *The CAPs considered in this work, both from the literature and proposed in this work.*

CAP type	$V(x)$ (units of $\hbar^2/2m$)
quadratic [141, 146]	$-i\alpha^2(x - x_0)^2$
cosine masking function [151]	$-i\alpha^2 \log\{\sec[(x_0 - x)/\beta]\}$
M-JWKB [144]	$-ik_{\min}^2\epsilon(x)$
quartic [141, 146]	$-i\alpha^2(x - x_0)^4$
pseudo-exponential [138]	$-i\alpha^2 e^{-\beta/(x_0 - x)}$
Pöschl-Teller [137]	$-i\alpha^2\text{sech}^2[(x + x_0)/\beta]$
single-exponential (present)	$-\alpha^2 e^{-x/\beta}$
double-exponential (present)	$-\alpha_1^2 e^{-x/(2\beta)} - i\alpha_2^2 e^{-x/\beta}$
double-sinh (present)	$-\alpha_1^2/(2\sinh[x/(2\beta)]) - i\alpha_2^2/(2\sinh[x/(2\beta)])^2$

mization. This simplicity is certainly one of its strengths and derives from the fact that its reflection coefficient effectively decreases monotonically from unity at zero energy to $e^{-\sqrt{2}\pi/\delta}$ at infinite energy. Its explicit expression is in terms of the Jacobi elliptic function $\text{cn}(u, k)$,

$$\epsilon(x) = \sqrt{\text{cn}^{-4}[2\delta k_{\min}(x_0 - x)/\sqrt{2}, 1/\sqrt{2}] - 1}, \tag{6.2}$$

with $x_0 = 2.622/(2\delta k_{\min})$ [144] where $k_{\min} = \sqrt{2mE_{\min}/\hbar^2}$. One simply chooses δ from the condition $R(E_{\min}) = R_c$.

The first five CAPs in the table are defined to be non-zero only for $0 \leqslant x \leqslant x_0$ and to vanish identically for $x > x_0$. The remaining CAPs are defined for all x, but vanish exponentially with x. The first four CAPs are some of the most commonly used, with the cosine masking function recast as a CAP using $e^{-iV(x)\Delta t} \sim \cos^{1/8}[(x - x_0)/\beta]$.

We include the Pöschl-Teller potential because it is well known to be reflectionless for specific *real* values of $i\alpha^2$, suggesting that it might have advantageous properties as a CAP. It can be shown analytically, however, that this property no longer holds for complex $i\alpha^2$. In the process of optimizing it for the present purposes, we found that shifting its center off the grid minimized x_R, leaving only its exponential tail on the grid. This result suggested using instead the simpler family of exponential CAPs included in the table.

We calculate the reflection coefficient numerically using the finite-element discrete-variable representation (FEDVR) [164, 165] and eigenchannel R-matrix method [90]. See Appendix C.2 and Sec. 3.1.6 for details. The reflection coefficient can also be calculated analytically for several of the potentials in Table 6.1. However, we give the analytic solutions (derivations in the appendices) only for the CAPs we propose — namely, the single-exponential and double-exponential CAPs. The double-sinh potential has no analytic solution to the best of our knowledge. In these cases, we confirmed that the R-matrix reflection coefficients agreed with the analytical R to several significant digits.

Since our primary goal is to systematically design an absorbing potential for the strong-field ionization problem with predetermined properties, we will use atomic units for the

remainder of our discussion. Our results can be readily applied to other problems, though, using the derivations in the appendices in which the masses and SI units are explicitly retained.

6.3 Optimization of proposed CAPs

We demonstrate our optimization procedure in detail below first for the single-exponential CAP since it is the simplest to optimize. It also establishes a few key results important for the optimization of our recommended CAPs: the double-exponential and double-sinh potentials. Whether the solution is analytical or numerical, the procedure we describe for optimization is the same and can be applied to other CAPs as well. In fact, this is what we have done for the comparison in Sec. 6.4.

The values of R_c, $E_{\min}$, and $E_{\max}$ that we will focus on for this discussion are

$$R_c = 10^{-3}, \ E_{\min} = 0.006 \, \text{a.u.}, \ \text{and} \ E_{\max} = 3 \, \text{a.u.} \tag{6.3}$$

We chose this energy range to cover $0.1\hbar\omega \leqslant E \leqslant 14U_p$ for an 800-nm laser pulse at $10^{14} \, \text{W/cm}^2$ (U_p is the pondermotive energy: $U_p = I/4\omega^2$ with I the intensity and ω the laser frequency). This energy range includes essentially all photoelectrons one would expect to be produced in this typical pulse. In momentum, which is more convenient for the analytical R, this range corresponds to

$$k_{\min} = 0.110 \, \text{a.u. and } k_{\max} = 2.45 \, \text{a.u.} \tag{6.4}$$

Note that $14U_p$ exceeds the highest-energy electrons one would normally expect in a strong-field problem, but we will show below that this choice has little effect on the resulting x_R. Finally, we use $V_c = 10^{-4}$ a.u. to define x_R from $|V(x_R)| = V_c$.

6.3.1 Single-exponential CAP

We take the single-exponential CAP to have the form

$$V(x) = -\frac{\hbar^2\alpha^2}{2m}e^{-x/\beta} \tag{6.5}$$

Its reflection coefficient, as shown in Appendix A.1, is

$$R = e^{4K \arg \lambda^2} \left| \frac{J_{2iK}(2\lambda)}{J_{-2iK}(2\lambda)} \right|^2, \tag{6.6}$$

where the unitless momentum is $K = k\beta$ with $k = \sqrt{2E}$ and the unitless potential strength is $\lambda = \alpha\beta$. To achieve our goal of minimizing x_R, we must find the optimal λ and β.
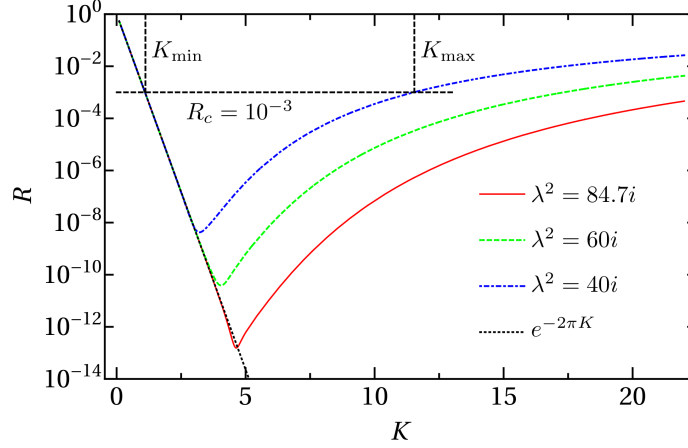
Figure 6.2: *Examples of the reflection coefficient $R(K)$ for a single-exponential CAP with different potential strengths. The predicted small-K behavior, $e^{-2\pi K}$, is shown for comparison. The unitless limits $K_{\min}$ and $K_{\max}$ for which $R(K) \leqslant R_c$ holds are also indicated.*

Purely imaginary potential

For a purely imaginary potential, $\lambda^2 \propto i$, Fig. 6.2 shows the behavior of R as a function of K. As the figure suggests, one can show from Eq. (6.6) that

$$R \xrightarrow[K \to 0]{} e^{-2\pi K}. \tag{6.7}$$

As can also be seen in the figure, increasing the strength $|\lambda^2|$ of the CAP means this exponential decrease continues to larger K and the large-K tail decreases.

We can thus use Eq. (6.7) to write

$$K_{\min} = -\frac{1}{2\pi} \log R_c, \tag{6.8}$$

giving

$$K_{\min} = 1.10$$

for $R_c = 10^{-3}$. From $K_{\min} = k_{\min}\beta$, the scale β is therefore determined:

$$\beta = \frac{K_{\min}}{k_{\min}} = 10.0 \,\text{a.u.}.$$

We can now find the required λ^2 from

$$R(K_{\max}) = R\left(\frac{k_{\max}}{k_{\min}} K_{\min}\right) = R_c \tag{6.9}$$

since $K_{\mathrm{max}}=k_{\mathrm{max}}\beta$. Solving this equation gives

$$\lambda^2 = 84.7i \text{ and } x_R = 83.4 \text{ a.u.} \tag{6.10}$$

This example illustrates the fact that x_R can only be substantially decreased if β is decreased. Thus, K_{min} and k_{min} determine x_R, and K_{min} is set by the form of the CAP and its parameters. In general, the smaller k_{min} is, the more difficult absorption becomes. Roughly speaking, this behavior can be traced to the need for x_R to be large enough for the potential to contain the longest wavelength to be absorbed.

Complex potential

Given k_{min}, decreasing β further requires decreasing K_{min}. This is not possible with a purely imaginary single-exponential CAP, so we must allow λ^2 to be complex.

The reflection coefficient in Eq. (6.6) still holds for complex λ^2 and looks generically like those displayed in Fig. 6.2—with the exception that

$$R \xrightarrow[K\to 0]{} e^{-4\pi K + 4K \arg \lambda^2}. \tag{6.11}$$

This small-K behavior suggests that the best way to reduce K_{min}—and thus β and x_R—is to make $\arg \lambda^2$ small (since $\arg \lambda^2$ must be positive to have absorption). That is, we should make $\operatorname{Re} \lambda^2$ much larger than $\operatorname{Im} \lambda^2$. The fastest decay one can achieve with this approach is $e^{-4\pi K}$ which, in turn, sets the limit on how small K_{min} can be.

The physical origin of this faster low-K decrease is clear: the real part of the potential is attractive and accelerates the wave before it encounters the imaginary part of the potential [146]. Absorption thus occurs at a shorter wavelength where absorption can be efficient with a much smaller x_R. Since $\operatorname{Im} \lambda^2$ must be large enough for sufficient absorption, however, $\arg \lambda^2$ cannot be zero. The optimum value will be a compromise between these two factors.

To determine the magnitude of the improvement in x_R, we use $\lambda = |\lambda|e^{i\chi}$ and the small-K behavior in Eq. (6.11) to write

$$K_{\mathrm{min}} = \frac{\log R_c}{4(2\chi - \pi)}. \tag{6.12}$$

From this, we can find β and K_{max} for a given χ. Combining everything and simplifying reduces the problem to solving Eq. (6.9) for $|\lambda|$ with $R(K)$ from Eq. (6.6). The resulting x_R as a function of χ is shown in Fig. 6.3.

The figure shows that the optimization problem has been reduced to a one-dimensional minimization of x_R with respect to χ. As expected, the solution,

$$x_R = 57.1 \text{ a.u.} \tag{6.13}$$

at $\chi=0.055\pi$ (with $|\lambda^2| = 165$), lies at small χ. Adding a real part to the absorbing potential
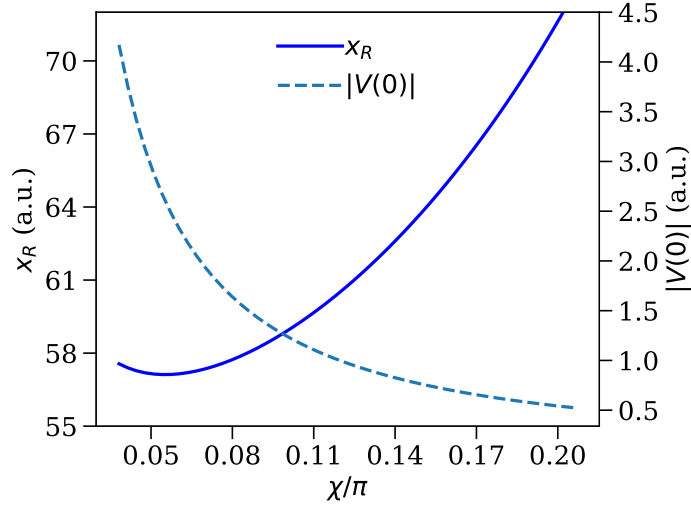
Figure 6.3: *Absorption range and potential depth for a single-exponential CAP, showing their dependence on the complex phase of λ. The magnitude of λ is determined at each χ by solving Eq. (6.9).*

has thus reduced the absorption range by 32% over the purely imaginary single-exponential CAP.

Figure 6.3 also shows that at the optimal x_R, the potential is 2.62 a.u. deep. This is roughly equal to $E_{\max}$, leading to local kinetic energies of approximately $2E_{\max}$ and thus requiring a much denser spatial grid in the absorption region. Guided by the figure, however, we see that a modest few-percent increase in x_R to 58.9 a.u. ($\lambda^2 = 97e^{i\pi/5}$) reduces $|V(0)|$ to 1.25 a.u., making it more computationally attractive. Further reduction in $|V(0)|$ can, of course, be achieved — at the expense of x_R.

Figure 6.4 shows the optimum R for both the purely imaginary single-exponential CAP of the previous section and the complex single-exponential CAP of the present section. The coefficients satisfy $R \leqslant R_c$ for different ranges of the scaled momentum K but the same range of the physical momentum k. The range of K covered by the complex CAP is smaller than for the imaginary CAP by the ratio of their respective $K_{\min}$'s.

6.3.2 Double-exponential CAP

It has long been known, of course, that adding a real potential improves CAP performance [146]. And, given the improvement to the single-exponential CAP afforded by doing so, it is natural to ask whether we can do even better with a more flexible complex potential.

Since we want to retain the ability to calculate R analytically and since the real part
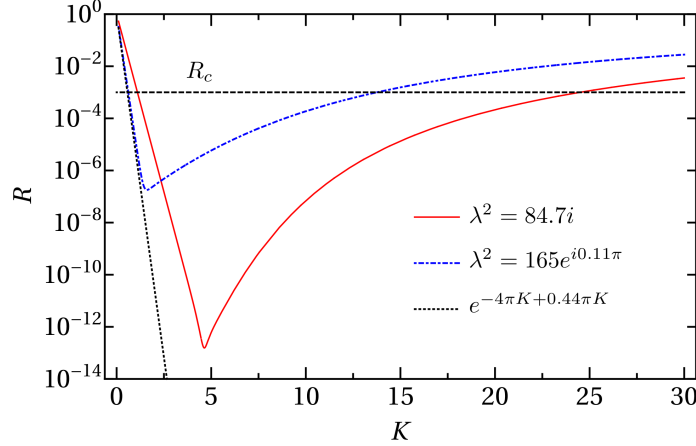
Figure 6.4: *The optimum reflection coefficients for purely imaginary and complex single-exponential CAPs as a function of the unitless momentum.*

must have longer range than the imaginary part, we choose the CAP to be

$$V(x) = -\frac{\hbar^2 \alpha_1^2}{2m} e^{-x/2\beta} - i\frac{\hbar^2 \alpha_2^2}{2m} e^{-x/\beta}. \tag{6.14}$$

The reflection coefficient, as shown in Appendix A.2, can be written in terms of the confluent hypergeometric function as

$$R = \left| \frac{{}_1F_1(\eta + 2iK, 1 + 4iK, -4\gamma^3\lambda_2)}{{}_1F_1(\eta - 2iK, 1 - 4iK, -4\gamma^3\lambda_2)} \right|^2 \tag{6.15}$$

where

$$K = k\beta \qquad\qquad \lambda_1 = \alpha_1\beta \qquad\qquad \lambda_2 = \alpha_2\beta$$

$$\gamma = e^{i\pi/4} \qquad\qquad \Lambda = \frac{\lambda_1^2}{\lambda_2} \qquad\qquad \eta = \frac{1}{2} - \gamma\Lambda.$$

λ_1 and λ_2 independent

Given the extra potential parameter, optimizing the double-exponential CAP is clearly more challenging than for the single-exponential CAP. And, the complicated expression for R only exacerbates the task. It would therefore be convenient to find a regime in which λ_1 and λ_2 are independent since this would greatly simplify the optimization.

To this end, we show in Fig. 6.5 the dependence of R on λ_1 and λ_2. Generally speaking, λ_1 — the coefficient of the longer-ranged, real part of V — controls the low-energy behavior, while λ_2 — the coefficient of the shorter-ranged, imaginary part of V — controls the high-energy behavior. The underlying physical reasons for these connections are the same as discussed for the single-exponential CAP.
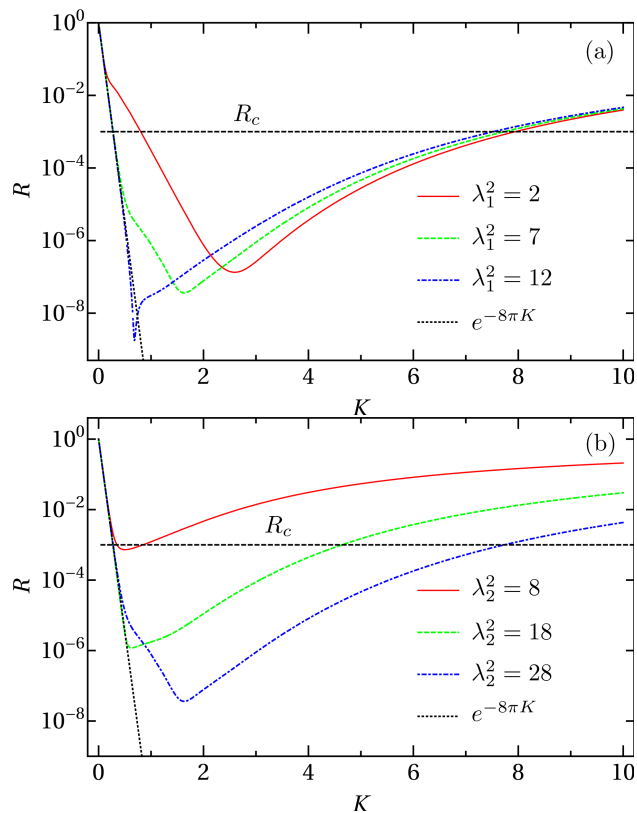
Figure 6.5: *Illustration of the dependence of R for a double-exponential CAP on the potential strength: (a) λ_1 dependence for $\lambda_2^2 = 28$, and (b) λ_2 dependence for $\lambda_1^2 = 7$.*

Figure 6.5 also shows that for λ_1 and λ_2 large enough,

$$R \to e^{-8\pi K} \tag{6.16}$$

for $R \sim R_c$. This behavior immediately shows the benefit of the double exponential since it falls faster than is possible with a single exponential, Eq. (6.11), leading to a smaller $K_{\min}$ and thus a smaller x_R.

In the regime that Eq. (6.16) holds, $K_{\min}$ is independent of λ_1 and λ_2 and takes the value

$$K_{\min} = -\frac{1}{8\pi} \log R_c. \tag{6.17}$$

For $R_c = 10^{-3}$, $K_{\min} = 0.275$ which is indeed much smaller than was possible with the single-exponential CAP.

Minimizing x_R now requires fixing λ_1 to a large enough value that Eq. (6.16) holds ($\lambda_1^2 \gtrsim 6$ is typically sufficient) and solving Eq. (6.9) for λ_2. Using R from Eq. (6.15) and $K_{\max} = 6.125$, we find, for instance,

$$\lambda_1^2 = 6 \text{ and } \lambda_2^2 = 22.6, \text{ leading to } x_R = 42.4\,\text{a.u.} \tag{6.18}$$

and the reflection coefficient shown in Fig. 6.6. There are, however, any number of combinations of λ_1 and λ_2 that satisfy Eq. (6.9). Since x_R for the double-exponential CAP is determined to a very good approximation by λ_1 alone, though, one would typically choose the smallest possible λ_1 to obtain the smallest possible x_R. At the same time, it should be noted that $x_R \propto \log \lambda_1$, so it is not terribly sensitive to small changes in λ_1. Choosing the smallest λ_1, however, also ensures that $|V(0)|$ is minimized, thereby keeping the numerical cost down.

λ_1 and λ_2 not independent

Although $x_R = 42.4\,\text{a.u.}$ is a significant improvement over the single-exponential result, $x_R = 57.1\,\text{a.u.}$, we can do better. The way to do this is to consider smaller λ_1^2 where there are particular combinations of λ_1 and λ_2 for which R falls off faster than Eq. (6.16). Such behavior permits smaller $K_{\min}$ and thus smaller x_R. Of course, λ_1 and λ_2 are no longer independent in this regime, but it is still true that λ_1 largely — but not as completely as above — controls $K_{\min}$ and λ_2, $K_{\max}$.

Figure 6.6 illustrates the small-K behavior that we want to take advantage of. For this combination of λ_1 and λ_2, R dips below the exponential from Eq. (6.16) for $R \sim R_c$ as seen in the figure. At this and other such parameter combinations, a local minimum develops in R at K near $K_{\min}$ as shown in the figure. In practice, one searches for these λ_i combinations to minimize $K_{\min}$ while simultaneously ensuring that the local maximum in R remains below R_c.

To find the minimum value of $K_{\min}$, we take advantage of its weak dependence on λ_2 by first minimizing with respect to λ_1 for some reasonable choice of λ_2. With this value
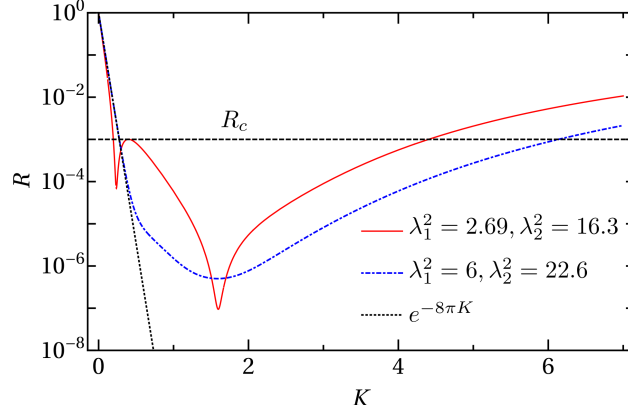
Figure 6.6: *The optimum reflection coefficient as a function of the unitless momentum for the double-exponential CAP with λ_1 and λ_2 both independent and not independent.*

of λ_1, we then solve Eq. (6.9) for λ_2. Since there is a weak dependence on λ_2, though, $K_{\min}$ must be re-minimized for λ_1 with this new λ_2. Then, Eq. (6.9) must again be solved and the iteration continued until sufficient convergence in λ_1 and λ_2 is obtained. Typically, only a handful of iterations are necessary to find 3 digits. More sophisticated methods of performing the constrained minimization of $x_R(\lambda_1, \lambda_2)$ could, of course, be employed as well.

As above, there are many combinations of λ_1 and λ_2 that give the smallest $K_{\min}$, $K_{\min} = 0.197$. But, our ultimate goal of minimizing x_R leads us to choose the smallest λ_1 possible. One convenient example for the optimal values is

$$\lambda_1^2 = 2.69 \text{ and } \lambda_2^2 = 16.3,$$

which leads to

$$\beta = 1.79 \text{ a.u. and } x_R = 29.9 \text{ a.u..}$$

The corresponding R is shown in Fig. 6.6. Although difficult to prove, this choice appears to be the global optimum for this choice of $E_{\min}$, $E_{\max}$, and R_c.

6.3.3 Double-sinh CAP

While straightforward, the optimization procedure outlined above for achieving such a substantial reduction in x_R is somewhat tedious. Fortunately, it needs to be done only once for a given R_c and ratio $E_{\max}/E_{\min}$. Should one wish to change R_c or only one of the energy limits, however, re-optimization is required. It turns out, though, that the latter limitation can be lifted without compromising on x_R.

In general, one expects the reflection coefficient to be unity for $E = 0$ and $E \to \infty$, and this is the behavior displayed by all the reflection coefficients we have shown. Consequently, the reflection coefficient necessarily satisfies $R(E) = R_c$ at both low and high energies. As mentioned in Sec. 6.2, however, the M-JWKB CAP [144] produces an R that decreases
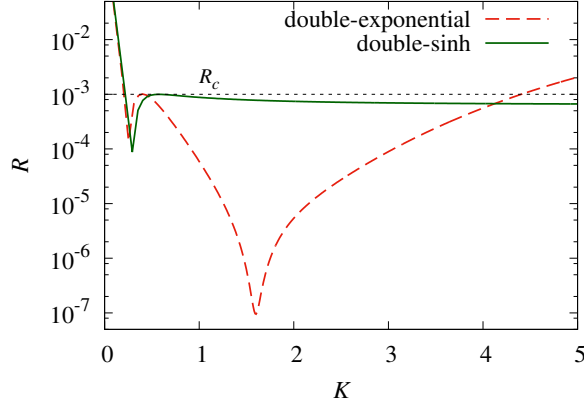
Figure 6.7: *Optimal R for the double-sinh CAP along with the optimal R for the double-exponential CAP for comparison using parameters in Table 6.2, both as a function of the unitless momentum.*

more-or-less monotonically to a value controllably less than unity at infinite energy. Its parameters thus do not depend on E_{max}, removing the need for re-optimizing with changes in either E_{min} or E_{max}. Unfortunately, x_R for the M-JWKB CAP turns out to be 118 a.u. because its R falls off relatively slowly at low energies, leading to a large K_{min}.

To retain both the small x_R found for the double-exponential CAP and the advantageous high-energy behavior of the M-JWKB CAP, we have designed the double-sinh CAP:

$$V(x) = -\frac{\hbar^2}{2m}\frac{\alpha_1^2}{2\sinh\frac{x}{2\beta}} - i\frac{\hbar^2}{2m}\frac{\alpha_2^2}{4\sinh^2\frac{x}{2\beta}}. \tag{6.19}$$

At large distances, this CAP reduces exactly to the double-exponential CAP, thus possessing its nice long-wavelength, low-energy properties. At short distances, this CAP is dominated by the $-i\alpha_2^2/x^2$ divergence of the second term. It is this behavior that is inspired by the M-JWKB CAP and that leads to similarly desirable high-energy behavior.

Unlike the single- and double-exponential CAPs, R for the double-sinh potential is not analytic as far as we know (unless $\alpha_1{=}0$ — in which case, it reduces to one-half of the generalized Pöschl-Teller potential [166]). We must thus calculate R numerically, and the optimal result is shown in Fig. 6.7 along with the optimal double-exponential result for comparison. Their absorption ranges are $x_R{=}28.8$ a.u. and $x_R{=}29.9$ a.u., respectively, confirming that there is no compromise on x_R. We note that the qualitative behavior of the double-sinh R shown is typical for this CAP.

From the figure, the similarity of the two reflection coefficients at low energies is evident. Specifically, the value of K_{min} — which has the biggest influence on x_R — is nearly identical between the two. In fact, the optimal values of λ_i from the double-exponential CAP provide a very good initial guess for the optimization of the double-sinh CAP.

Also evident from Fig. 6.7 is the difference in the two CAPs' R at high energies. Where

76

the double-exponential R rises back towards unity at high energies, the double-sinh R asymptotes to a value less than unity. This value can be approximately calculated, by considering only the $-i\alpha_2^2/x^2$ behavior of V, to be

$$R \xrightarrow[K \to \infty]{} e^{\pi \mathrm{Im}\sqrt{1-4i\lambda_2^2}}, \tag{6.20}$$

consistent with the limiting behavior found in Ref. [144].

Given the discussion in Sec. 6.3.1, one might wonder whether allowing the λ_i to be complex — rather than real as assumed so far — could improve the CAPs' performance even further. The simple answer is that it can. In fact, the double-sinh CAP plotted in Fig. 6.7 has complex λ_i. We could not, however, find a more optimal double-exponential CAP by allowing λ_i to be complex for the present $E_{\min}$, $E_{\max}$, and R_c (see, however, Sec. 6.5.2).

Incidentally, Eq. (6.20) gives the reflection coefficient at *all* energies for a CAP that has the form $-i\alpha_2^2/x^2$ everywhere (see Appendix A.3). In particular, the reflection coefficient is not unity at zero energy like the other CAPs we consider and thus corresponds to $K_{\min}=0$. In many ways, such a CAP would be ideal — no optimization would be necessary and λ_2 could simply be calculated by setting Eq. (6.20) to R_c. Unfortunately, x_R=110 a.u. for such a CAP, rendering it uncompetitive with our best CAP — although better than the quadratic CAP often used in the literature (see Table 6.2).

One possible solution would be to simply cut the $-i\alpha_2^2/x^2$ CAP off at some x_0. Intuitively, this should affect the low-energy behavior of R for wavelengths comparable to and larger than x_0. The reflection coefficient in this case is again analytic (see Appendix A.3), and it can be seen after some exploration that while this expectation is true, R falls off at small k more-or-less like $1/(kx_0)^4$ rather than like the exponential decrease of our best CAPs. Since one chooses x_0 for this CAP from

$$R(k_{\min}x_0) \sim 1/(k_{\min}x_0)^4 = R_c, \tag{6.21}$$

x_0 — and thus x_R — winds up being large. For instance, x_R=57 a.u. for $R_c = 10^{-3}$, which is about double that for our best CAP.

In the context of this discussion, the double-sinh CAP can be seen as providing a smooth cutoff of the $-i\alpha_2^2/x^2$ CAP and similarly leads to modifications of Eq. (6.20) at small energies.

Fall-to-the-center problem

Whenever an attractive $1/x^2$ potential is used, one must take care to consider the "fall-to-the-center" problem. The real-valued version of such potentials are known [167] to have an infinite number of bound states with energies stretching to $-\infty$ — a fact reflected in the wave function's oscillating an infinite number of times as $x \to 0$ — so long as the potential strength exceeds a critical value. This is the quantum-mechanical analog of the classical fall-to-the-center problem in such potentials. Moreover, this effect is possible even for potentials that are only $1/x^2$ for small x like our double-sinh CAP.

No finite numerical representation — such as the grid methods common for TDSE solvers — can represent the infinity of oscillations in the fall-to-the-center regime, and any attempt to accurately represent even a finite number of them will be very costly computationally.

To understand how to avoid this regime, we must examine the small-x behavior of the wave function. From Appendix A.3 and using its notation, we see that

$$\psi \xrightarrow[z \to 0]{} z^{\frac{1}{2}+(a_r-|a_i|)/\sqrt{2}} \exp\left[i\frac{a_r+|a_i|}{\sqrt{2}}\log z\right].$$

This solution assumes $a_r > |a_i|$ and shows that even for a nearly purely imaginary CAP, $a_i=0$, the wave function oscillates an infinity of times as $z \to 0$. Empirically, choosing $a_r \gg |a_i|$ so that the first term above suppresses the wave function for $z \to 0$ is sufficient to prevent numerical difficulties. Consequently, we have chosen $a_i=0$, which is equivalent to $\lambda_2^2 = a_r^2 - i/4$.

6.3.4   Complex boundary condition

We have so far assumed that the wave function vanishes on the boundary at $x = 0$ as is typical for most TDSE solvers. But, if the numerical method used to solve the TDSE is flexible enough to allow complex log-derivative boundary conditions, then additional absorption can be built in at very little additional cost.

The effect of the complex boundary condition,

$$\frac{1}{\psi}\frac{d\psi}{dx} = b, \tag{6.22}$$

can be most easily illustrated for a free particle. If one imposes Eq. (6.22) at $x=0$ as in Fig. 6.1, but with no potential, one obtains the reflection coefficient (see Appendix B for more details, including the effect on bound-state energies)

$$R = \left|\frac{B + iK}{B - iK}\right|^2 \tag{6.23}$$

with $B = b\beta$. To have absorption, we must have $\text{Im } B \leqslant 0$; to have maximum absorption, we must have $\text{Re } B=0$. Thus, setting $B = -iK_0$, we see that $R = 0$ at $K = K_0$. Such a boundary condition therefore makes the boundary perfectly transparent to an incident plane wave of momentum K_0 and partially transparent to other momenta. Moreover, it does so with $x_R=0$.

Unfortunately, this boundary condition by itself cannot compete with the CAPs since R cannot be made small enough over a large enough energy range. Since implementing it, in principle, requires no change in the spatial grid, though, the possibility of combining it with a CAP and reducing x_R further is worth exploring.

At low energies, the CAP will dominate the behavior of R, and the boundary condition

Figure 6.8: *Reflection coefficient as a function of the unitless momentum for a single-exponential CAP with complex boundary conditions: purely imaginary λ^2 and complex λ^2.*

will have little influence. Therefore, one should try to use the boundary condition to modify the high-energy R where it can dominate the behavior. In general, choosing $B \sim -iK_{\mathrm{max}}$ is a good initial guess and allows the reduction of λ — and therefore x_R.

It should be noted that a complex boundary condition cannot be used with the double-sinh CAP due to its singularity at the boundary. Like the centrifugal potential that it resembles, the double-sinh CAP has one regular solution that vanishes at the boundary and one irregular solution that diverges at the boundary [144]. Therefore, it is not possible to form the necessary linear combinations to satisfy Eq. (6.22).

Single-exponential CAP

The reflection coefficient for a single-exponential CAP with a complex boundary condition is again analytic and is given in Eq. (B.9). The CAP parameters must be re-optimized along with the value of b, and the procedure is largely the same as described above. The fact that K_{min} is essentially unaffected by the addition of the complex boundary condition — so long as $|B| \sim |K_{\mathrm{max}}|$ — simplifies the process.

Examples of optimal choices are shown in Fig. 6.8 for a purely imaginary CAP and a complex CAP. Comparison with the reflection coefficients shown in Sec. 6.3.1 shows the effect of the complex boundary condition through the appearance of the high-energy minimum close to $K = |B|$. In both cases, the complex boundary condition has produced a roughly 15% reduction in x_R to 71.7 a.u. and 48.1 a.u., respectively.

Double-exponential CAP

Adding a complex boundary condition to the double-exponential CAP also produces an analytic expression for R as given in Eq. (B.10). Re-optimizing the parameters yields the reflection coefficient shown in Fig. 6.9. As with the single-exponential CAPs, the boundary condition has introduced a high-energy minimum near $K = |\mathrm{Im}\, B|$. Unlike the single-exponential CAPs, though, the minimum x_R was found for $\mathrm{Re}\, B \neq 0$.

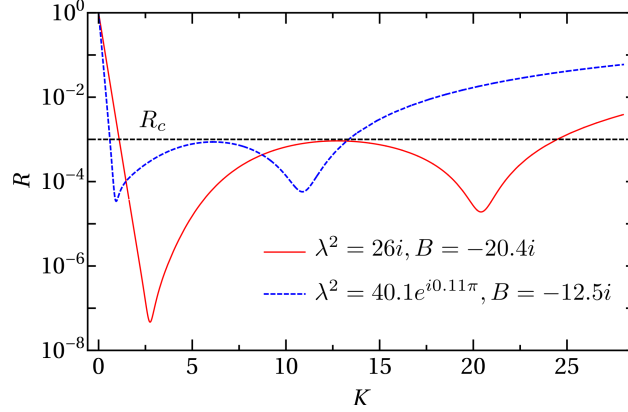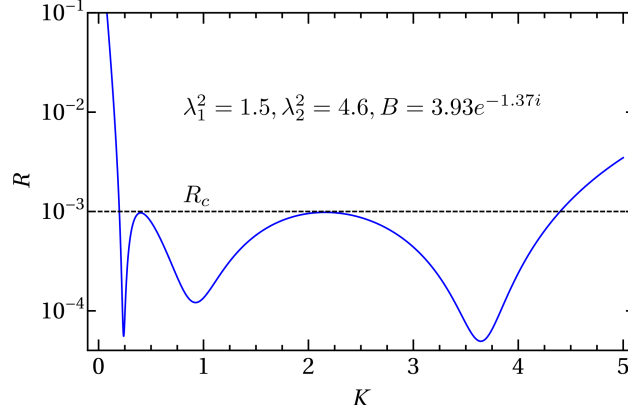**Figure 6.9**: *Optimum reflection coefficient as a function of the unitless momentum for a double-exponential CAP with complex boundary conditions.*

This optimum double-exponential CAP continues the pattern that has emerged as we have found improved CAPs: namely, that we add more structure to R and decrease the absorption for the mid-range of K. The double-exponential-CAP reflection coefficients in Fig. 6.6, for instance, have comparatively little structure — mainly a minimum in R. Moreover, this minimum is relatively broad and orders of magnitude lower than R_c. The R shown in Fig. 6.9, in contrast, has three narrower minima only one order of magnitude or so lower than R_c.

6.4 Optimal CAP

To determine which CAP — among those listed in Table 6.1 — is the best, we numerically searched for their optimal parameters, assuming they are purely imaginary potentials. From the discussion above, we know that each could be improved by including a real potential and a complex boundary condition, but we expect — and confirmed with spot tests — that the relative performance of the CAPs will remain qualitatively the same. As mentioned previously, we selected the CAPs to compare based on their apparent popularity in the literature or on the claims made for their performance.

In optimizing these CAPs, we follow the principles described in previous sections that the width of the CAP determines the long-wavelength absorption; and the depth, the short-wavelength. The optimization is then reasonably straightforward once we identify the parameters corresponding to the width and depth.

In Table 6.2, we list the optimal parameters we have found for our $E_{\min}$, $E_{\max}$, and R_c. The table includes the resulting values of x_R, and we expect that they are the optimal values to within a few percent. Note that we used $\delta=0.1$ for the M-JWKB CAP based on the solution of $R(E_{\min}) = R_c$ taken from Fig. 3 of Ref. [144]. We show in Fig. 6.10 the corresponding reflection coefficients.

The cosine masking function should be regarded as a polynomial CAP since its behavior

Table 6.2: *Comparison of the optimal absorption ranges for all the CAPs considered. The optimal parameters are given for the electron in our strong-field application — see Eqs. (6.3) and (6.4) — so that all quantities are in atomic units.*

CAP type	α^2 or (α_1^2, α_2^2)	b	β	x_0	x_R
quadratic	1.21×10^{-5}		—	129	124
cosine masking function	15.9		810	128	124
M-JWKB	—		—	119	118
quartic	2.40×10^{-9}		—	112	95
pseudo-exponential	4.54×10^5		3.27×10^3	240	88
Pöschl-Teller	11.0		20.3	40.0	85
single-exponential	$0.849i$		10.0	—	84
single-exponential+BC	$0.260i$	$-2.04i$	10.0	—	72
single-exponential	$5.24e^{i0.11\pi}$		5.62	—	57
single-exponential+BC	$1.35e^{i0.11\pi}$	$-2.29i$	5.45	—	48
double-exponential	$(0.839, 5.09)$		1.79	—	30
double-sinh	$(0.298e^{0.104i}, 0.71e^{-0.0906i})$		1.97	—	29
double-exponential+BC	$(0.463, 1.42)$	$2.19e^{-1.37i}$	1.80	—	28
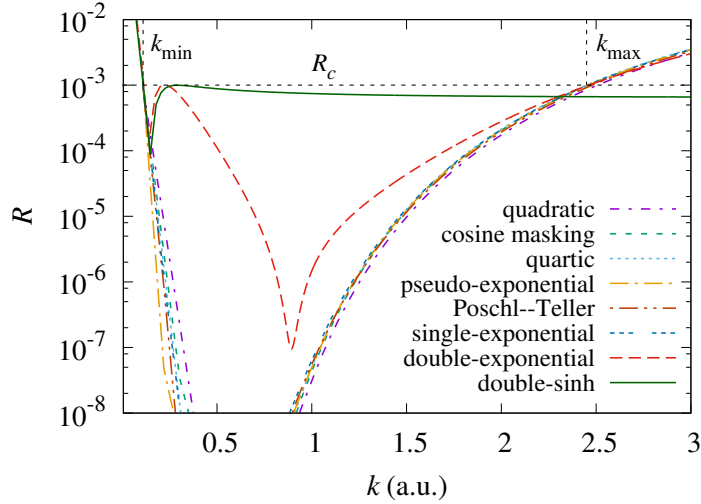
Figure 6.10: *Optimal reflection coefficients for all CAPs as a function of the electron's momentum using the parameters from Table 6.2. They all satisfy the criteria that $R \leqslant R_c$ for $0.006 \leqslant E \leqslant 3$ a.u., as required.*

81

in $0 \leqslant x \leqslant x_0$ for the optimal parameters of Table 6.2 is largely indistinguishable from the quadratic CAP — thus its x_R is identical to the quadratic CAP. Similarly, for the optimal parameters we found, only the exponential tail of the Pöschl-Teller potential remained on the grid, making its performance essentially identical to that of the purely imaginary single-exponential CAP.

The absorption ranges x_R listed in Table 6.2 display a surprisingly large range — more than a factor of 4. Comparing only the purely imaginary potentials, the exponential and Pöschl-Teller forms are more than 30% more efficient than the quadratic CAP. They are also more efficient than the quartic CAP. So, while the exponential form generally seems better, the majority of the disparity in Table 6.2 arises from adding a real part to the CAP and imposing a complex boundary condition.

From Table 6.2, the best performance is found for the double-exponential and double-sinh CAPs, outperforming the next-best CAP (the complex-valued, complex-boundary-condition, single-exponential CAP) by roughly 40%. Compared to the next-best purely imaginary CAP, they hold nearly a factor of 3 advantage in x_R. For reference, we tested the strategy of adding a real part and a complex boundary condition to the quadratic CAP and found x_R shrank only to about 70 a.u. So, while pursuing this strategy with the other CAPs in the table would reduce their x_R, we believe the double-exponential and double-sinh CAPs would remain the best. Interestingly, since the de Broglie wavelength at $k_{\min}$ is 57 a.u., our best CAP manages its efficient absorption in a range of only about half this longest wavelength.

Our recommendation, therefore, is to use the double-sinh CAP when its singularity at the boundary causes no numerical difficulties. In the cases that it does, then the double-exponential CAP is the best choice. The remainder of our discussion will thus focus on these two CAPs.

6.5 Other absorption criteria

The discussion and optimization so far has centered on the $E_{\min}$, $E_{\max}$, and R_c from Eq. (6.3). Other choices may well be needed, however, for other choices of laser parameters or calculational goals. We thus present in this section the optimal parameters for the double-exponential and double-sinh CAPs for a selection of likely changes in $E_{\min}$, $E_{\max}$, and R_c.

6.5.1 Different energy range

Changing $E_{\max}$

Computationally, the main challenges in solving the TDSE — especially for current and future laser parameters of experimental interest — are that in the course of its strongly-driven dynamics, the electron travels far from the nucleus and gains substantial energy. In particular, we still expect $E_{\max} \propto U_p \propto I/\omega^2$, so that it will grow either with increasing intensity or increasing wavelength — both of which are certainly of interest. While $E_{\min}$ does not change in this case, $E_{\max}$ does, and the CAP must accommodate it.

Table 6.3: *Optimal parameters for the double-exponential CAP for an electron exposed to longer wavelengths. Per the discussion in the text, the only impact of wavelength here is on E_{max}. All quantities are in atomic units unless otherwise specified.*

λ (nm)	E_{min}	E_{max}	α_1^2	α_2^2	β	x_R
800	0.006	3	0.839	5.09	1.79	29.9
1600	0.006	8.8	1.07	8.37	1.79	30.7
2400	0.006	20	1.31	12.4	1.79	31.5

Under these conditions, the double-sinh CAP from Table 6.2 works without change since it has no E_{max}. In fact, this is its primary advantage. The double-exponential CAP, on the other hand, must be re-optimized for each E_{max}. As discussed in Sec. 6.2, λ_2 needs the greatest changes — but should have minimal impact on x_R — and these expectations are reflected in the optimal parameters shown in Table 6.3 for two longer wavelengths. These parameters were found following the same procedure as above with the same k_{min} and R_c and with $E_{max}=10\,U_p$ at $10^{14}\,\mathrm{W/cm^2}$. They were found assuming $\psi = 0$ on the boundary, but parameters could certainly be found for a complex boundary condition as well. Note that x_R changes less than about 10% as expected.

Changing E_{min}

In our optimization scheme above, we set E_{min} to $0.1\,\hbar\omega$ for 800-nm light. This choice was motivated by the need to ensure that the entire ionized electron wavepacket is absorbed by the CAP. However, the CAP is often placed at a large distance from the nucleus so that these very slow electrons may not have time to reach the CAP during the propagation. In this case, E_{min} can be increased, thereby decreasing x_R.

Modifications to E_{min} for the double-sinh CAP are straightforward and do not require re-optimization — again, thanks to the lack of an E_{max}. Changing k_{min} just means recalculating β using $\beta = K_{min}/k_{min}$ since K_{min} is fixed. Figure 6.11 shows the x_R that results as a function of k_{min}. The figure shows that for modest increases in k_{min} from our choice in Eq. (6.4), x_R can be decreased substantially. For example, for k_{min} above about 0.3 a.u., x_R is smaller than 10 a.u. for $R_c=10^{-3}$. For k_{min} above about 0.4 a.u., the x_R for $R_c=10^{-10}$ is equal to or smaller than the original $x_R=28.8$ a.u. for the double-sinh CAP.

For a double-exponential CAP, it is still true that the larger k_{min}, the smaller λ_1 and λ_2, and the smaller x_R. However, re-optimization is required to obtain the smallest x_R. For instance, if one can accept doubling k_{min} to 0.22 a.u., then we can have

$$\lambda_1^2 = 2.00 \text{ and } \lambda_2^2 = 9.11, \text{ so that } x_R = 17.0\,\text{a.u.} \tag{6.24}$$

with $\beta=0.90$ a.u.

On the other hand, the double-exponential CAP can be adjusted just like the double-sinh CAP if a less-than-optimal x_R can be tolerated. Specifically, the values of λ_i^2 can be kept, so that K_{min} does not change, and β can be recalculated from $\beta = K_{min}/k_{min}$. In this case,
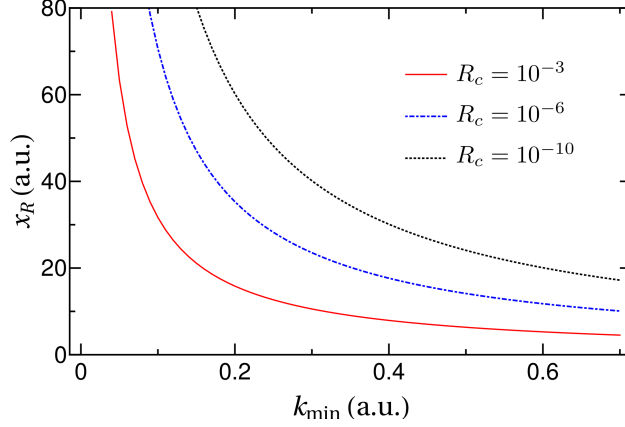
Figure 6.11: *Absorption range x_R as a function of k_{min} for the double-sinh CAP. The parameters for $R_c \leqslant 10^{-3}$ can be found in Table 6.4.*

k_{max} grows to $k_{min}K_{max}/K_{min}$, guaranteeing absorption at the prescribed level beyond E_{max}. The resulting x_R looks very much like those in Fig. 6.11, except that x_R for $R_c{=}10^{-3}$ does not go below 10 a.u. until $k_{min}{=}0.45$ a.u. For comparison, $x_R{=}17.4$ a.u. at $k_{min}{=}0.22$ a.u. and is thus slightly worse than the fully re-optimized result in Eq. (6.24).

6.5.2 Different R_c

One of the primary design goals of a CAP is to leave the physical wave function — the wave function outside the absorption region — unaffected. Of course, this goal can only be achieved to a given accuracy, and that accuracy is controlled by R_c. To see the relation, consider the physical wave function written in Fig. 6.1 from which R is extracted,

$$\psi(x) = e^{-ikx} + \sqrt{R}e^{i\varphi}e^{ikx}, \; x \geqslant x_R. \tag{6.25}$$

The second term is precisely the unwanted contribution from reflection, and it is limited by $R \leqslant R_c$ by design. Given that this is just one component of the time-dependent wave function, this error is always relative to the first term. In other words, if one desires n digits to be accurate, then one should choose $R_c{=}10^{-2n}$.

We thus provide in Table 6.4 the optimal parameters for the double-exponential and double-sinh CAPs with $\psi{=}0$ on the boundary, assuming $E_{min}{=}0.006$ a.u. and $E_{max}{=}3$ a.u. as before, for several smaller R_c. These results show that the absorption range for each type of CAP is comparable, with the double-sinh CAP tending to be a few percent smaller. Qualitatively, the reflection coefficients as a function of K resemble those shown previously for $R_c{=}10^{-3}$. As with the other CAP parameters we have given, we expect these to produce x_R within a few percent of the global optimum.

Note that the probability density corresponding to the wave function in Eq. (6.25),

$$|\psi(x)|^2 = 1 + R + 2\sqrt{R}\cos(2kx + \varphi), \tag{6.26}$$

Table 6.4:   *Optimal parameters for double-exponential and double-sinh CAPs for $R_c \leqslant$ 10^{-3}.*

Double exponential					Double sinh			
λ_1^2	λ_2^2	β (a.u.)	x_R (a.u.)	R_c	x_R (a.u.)	λ_1^2	λ_2^2	β (a.u.)
2.69	16.3	1.79	29.9	10^{-3}	28.8	$1.16e^{0.104i}$	$2.75 - 0.25i$	1.97
$4.83e^{0.187i}$	$31e^{0.0968i}$	2.77	44.7	10^{-4}	40.4	$1.78e^{0.23i}$	$4.30 - 0.25i$	2.90
$7.21e^{0.0486i}$	$57.6e^{-0.411i}$	3.38	54.5	10^{-5}	52.6	$2.66e^{0.346i}$	$6.82 - 0.25i$	3.87
$16.1e^{-0.219i}$	80.0	4.02	68.4	10^{-6}	64.2	$3.8e^{0.36i}$	$9.67 - 0.25i$	4.77
$19.4e^{i0.135\pi}$	$141e^{-0.073i}$	6.64	102	10^{-8}	89.4	$6.75e^{0.46i}$	$17.2 - 0.25i$	6.77
$30.8e^{i0.132\pi}$	$232e^{-0.204i}$	8.48	130	10^{-10}	109	$11.85e^{0.14i}$	$26.9 - 0.25i$	8.02
48	$355e^{-0.328i}$	9.04	144	10^{-12}	132	$16.1e^{0.21i}$	$38.7 - 0.25i$	9.77

can be useful for diagnosing issues with the CAP in a time-dependent calculation. In particular, the last term above is the source of the telltale ripples in the probability density near the edge of a grid. The ripples' size is limited by $\sqrt{R_c}$ and identifying their wavelength via Eq. (6.26) in a time-dependent wave function reveals the offending energy.

6.6   Time-dependent demonstration

To verify that the improved performance of our recommended CAPs does indeed carry over to the time-dependent problem and its numerical solution, we solve the TDSE for free-electron wavepacket propagation. The wavepacket we use possesses a broad momentum distribution comparable to the target momentum range from Eq. (6.4), as shown in Fig. 6.12(a).

We again use FEDVR as the spatial representation and propagate the wave function using the short-time evolution operator

$$\psi(x, t + \delta) = e^{-iH\delta}\psi(x, t) \tag{6.27}$$

where the Hamiltonian includes the CAP $V(x)$,

$$H = H_0 + V, \tag{6.28}$$

and H_0 is merely the kinetic energy in the present case. We evaluate $e^{-iH\delta}$ using the split-operator form [168]

$$e^{-iH\delta} \approx e^{-iV\frac{\delta}{2}}e^{-iH_0\delta}e^{-iV\frac{\delta}{2}}. \tag{6.29}$$

Since V is diagonal in FEDVR, $e^{-iV\delta/2}$ can be easily evaluated and applied. Moreover, in this form, the singularity in the double-sinh CAP causes no problems whatsoever. The action of the remaining term in H_0 is calculated via a Padé approximation [112].

Equation (6.29) is a simple and convenient way to add a CAP to any propagator. In
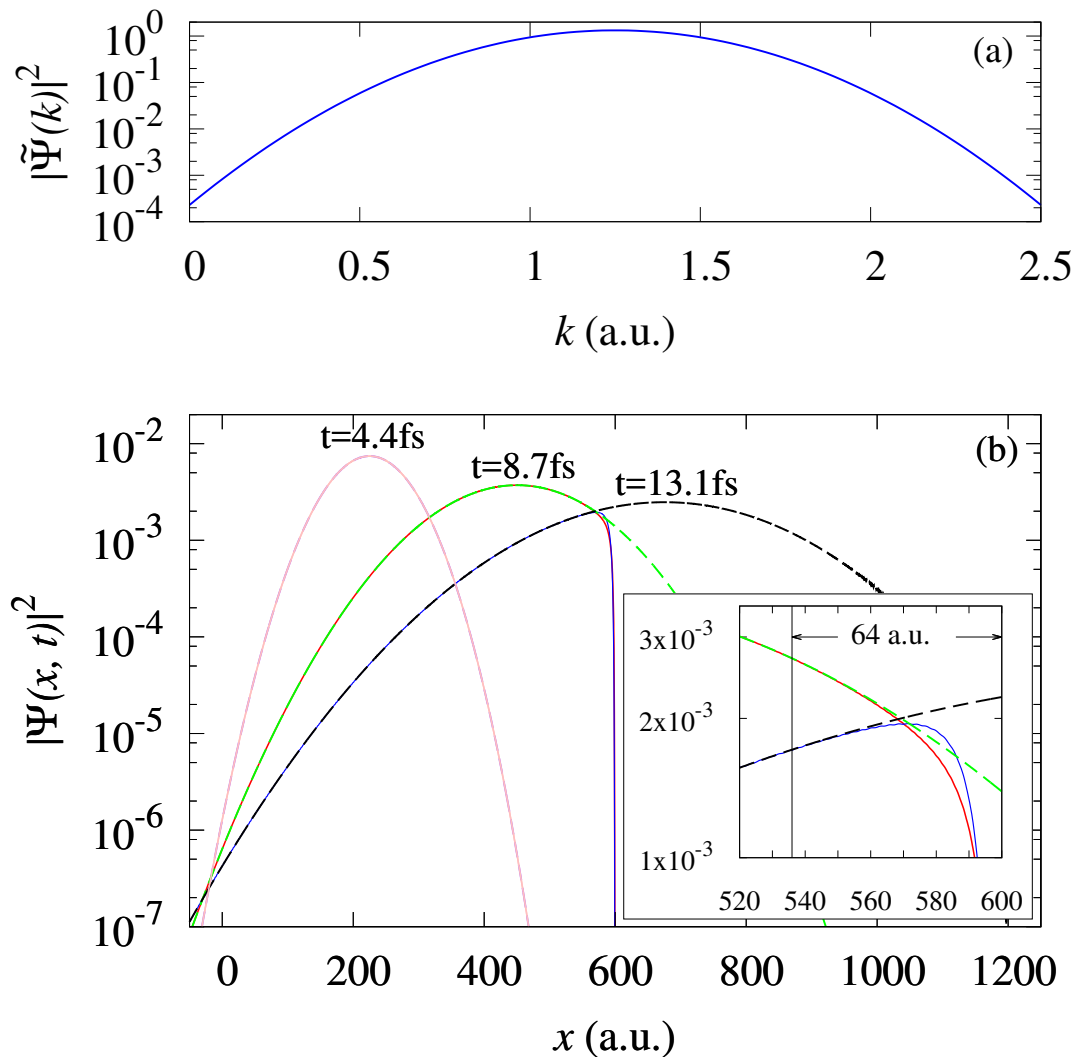
Figure 6.12: *(a) Momentum distribution of the free wavepacket, covering $0.11 \leqslant k \leqslant 2.45$ a.u. (b) Demonstration of the $R_c = 10^{-6}$ double-sinh CAP using a free wavepacket. Solid lines show the with-CAP wavepacket, calculated for $-600 \leqslant x \leqslant 600$ a.u.; and dashed lines, the without-CAP wavepacket, calculated for $-600 \leqslant x \leqslant 1200$ a.u. Inset: Expanded view of the absorption region $536 \lesssim x \leqslant 600$ a.u. for clearer comparison.*

many cases, the alternative, keeping the CAP in H, would require modifications of the propagation algorithm or parameters to handle its non-Hermiticity or the singularity of the double-sinh CAP — or both. These issues were discussed somewhat in Sec. 6.3.3 and more in Ref. [144]. Using Eq. (6.29) avoids these concerns and is more than sufficient for the application of the CAP.

The FEDVR element distribution is uniform in the range -600 a.u. $\leqslant x \leqslant 1200$ a.u., and we require $\psi = 0$ at the boundaries. Given that the wavepacket is initially centered near $x = 0$, this box is large enough for the wavepacket to propagate for 10 fs without significant reflection at the boundaries even without CAPs. This will be our reference solution. We carry out a second, identical propagation but apply the double-sinh CAP at 536 a.u. $\lesssim x \leqslant 600$ a.u.. For this example, we choose the CAP designed to have $R_c = 10^{-6}$ using the parameters shown in Table 6.4. We thus compare the wavepacket with and without applying the CAP. All the results have been tested to be converged to at least 3 digits with respect to all numerical parameters.

Figure 6.12 shows the two wavepackets at different times. It is clear that the CAP is performing as expected since the wavepacket decays in the absorbing region without any of the characteristic oscillations of reflections visible — at least without enlarging the plot by a factor of four or five. For comparison, the wavepacket without a CAP equally clearly shows the reflection oscillations at $t=13.1$ fs for reflections from the boundary at $x=1200$ a.u.

In addition, the with-CAP wavepacket is numerically unaffected before entering the absorbing region, agreeing with the without-CAP wavepacket to at least 3 digits for $x \lesssim 536$ a.u. for all times, even as more than 70% of the wavepacket has been absorbed. This agreement shows that the absorption range x_R defined in the time-independent study is consistent with the results from the time-dependent propagation.

Enlarging Fig. 6.12 by a factor of at least four or five will reveal the tiny reflection ripples in the with-CAP wavepacket near and in the absorption region. Their relative magnitude is about $10^{-3}=\sqrt{R_c}$ as expected. Per the discussion in Sec. 6.5.2, such oscillations are unavoidable with a CAP and testing with other CAPs and values of R_c further support the conclusions there. For example, the oscillation for $R_c=10^{-3}$ becomes fairly noticeable, which suggests that R_c should in practice be no larger than 10^{-4} — i.e., two digits in the wave function — to provide quantitatively reliable results. Finally, we note that the roughly 15-fs propagation time is comparable to a typical strong-field calculation, bringing some realism to this simple demonstration.

6.7 Summary

We have presented a systematic study to boost the performance of complex absorbing potentials. Based on the time-independent reflection coefficient, we were able to quantitatively design the most optimal absorbing potential of a given form. In particular, for ultrafast, strong-field TDSE solvers, the optimal CAP parameters should be determined by the absorbing energy range required for the laser parameters and by the desired accuracy of the TDSE solutions.

We proposed two new CAPs — namely, the double-sinh CAP and the double-exponential CAP — that significantly outperform the CAPs currently in standard use. Their superiority was demonstrated through comparison with optimized versions of most of the CAPs commonly found in the literature. Both of our proposed CAPs overcome the primary impediment to efficient performance — absorption of long wavelengths — while also absorbing a large range of energies that covers basically all strong-field processes. Because we quantified the CAP's performance and identified x_R as the figure of merit for their efficiency, we could show that using an exponential CAP already improved on the common quadratic CAP's performance by one third. A further factor of almost three was gained, however, by adding a real part to the CAP — a strategy well known in other uses of CAPs, but not in strong-field applications.

We highly recommend the double-sinh CAP for local spatial representations, such as FEDVR where the potential is diagonal. It is efficient, easy to use, and easy to adapt to different absorption criteria — i.e., energy range and level of absorption. Incorporating it into the time propagation via split-operator methods is easy and effective.

For other spatial representations, the double-sinh and the double-exponential CAPs are equally recommended. However, care might need to be taken for the double-sinh singularity close to the boundary. In case the double-sinh singularity is a problem for the propagator, the double-exponential CAP should be chosen. Although optimization of the double-exponential CAP is more involved than for the double-sinh CAP, it is still fairly straightforward. Its optimization procedure, along with that for the double-sinh CAP, is detailed in this work.

Chapter 7

Conclusive Remarks and Outlook

In this dissertation, we have developed/implemented new numerical frameworks to more accurately and efficiently study ultrafast, strong-field molecular ionization by solving the time-independent/time-dependent Schrödinger equations. We have investigated a time-independent picture: structure of the one-dimensional hydrogen molecule in adiabatic hyperspherical representation, where all breakup channels — including ionization — can be identified in a single picture, showing its advantage to study strongly correlated molecular dynamics with different breakup channels coupled with each other. We have also presented time-dependent studies of molecular ionization by numerically solving the TDSE, where various computational efforts have been dedicated to an efficient TDSE solver, such as choosing an appropriate coordinate system to prevent potential numerical hurdles, designing an optimal complex absorbing potential to reduce the spatial box size, and implementing a sparse-direct linear solver to take full advantage of the sparsity of the TDSE. Molecular ionization has been studied at large internuclear distances, where we have found strong-field two-center effects beyond both Young's double-slit interference and Cohen and Fano's picture of one-photon molecular two-center interference. Such a study suggests that molecular two-center dynamics have to be taken into account for studies of diatomic molecular ionization. Furthermore, a pump-probe study comparing experiments and theory has revealed a pronounced broad ionization peak at large pump-probe delays, which is partially attributed to the strong-field two-center effects, indicating the strong-field two-center effects in molecular ionization can be measured in experiments, even though its details might be system-dependent. Moreover, we have shown for the first time the low energy structure in molecular ionization in long wavelength lasers by solving the TDSE.

In the future, a few works along the lines of projects studied in this thesis are worth further exploring. For example, it would be interesting to observe molecular low energy structure coupled with the strong-field two-center effects by showing the low energy photoelectron spectrum as a function of large R's. Another possibility is to include nuclear motion in the molecular ionization, where one could study the non Born-Oppenheimer effect in the low energy structure in molecular ionization. One could also examine the impact of nuclear motion on the strong-field two-center effects. Including nuclear motion in strong-field molecular ionization involving 3D electron, however, is a non-trivial, computationally demanding

task. With a workstation similar to the one used in this thesis, it would be almost unfeasible unless further improvements being made within our current numerical framework. Fortunately, there are a couple of things one could try to optimize the one-electron TDSE solver, such as applying dynamical grid on any "radial" coordinates, using high-order propagation scheme to increase the time step, and modifying the matrix representation to take full advantage of parallel architectures.

My Publications

- Youliang Yu and B. D. Esry, "One-dimensional hydrogen molecule in hyperspherical representation," J. Chem. Phys. (to be submitted).

- Youliang Yu, M. Zohrabi, Ben Berry, G. S. J. Armstrong, T. Severt, Bethany Jochim, Peyman Feizollah, Kanaka Raju P., Jyoti Rajput, K. D. Carnes, B. D. Esry and I. Ben-Itzhak, "Strong-field molecular two-center effects beyond double-slit interference," (in preparation).

- Youliang Yu and B. D. Esry, "Low energy structure in molecular ionization," (in preparation).

- Youliang Yu and B. D. Esry, "Nuclear-electronic coherence in strong-field dissociative ionization," (in preparation).

- Youliang Yu and B. D. Esry, "An optimized absorbing potential for ultrafast, strong-field problems," arXiv preprint arXiv:1710.04338 (2017).

- Youliang Yu, Shuo Zeng, J. V. Hernández, Yujun Wang and B. D. Esry, "Influence of the initial angular distribution on strong-field molecular dissociation," Phys. Rev. A, **94**, 023423 (2016).

Bibliography

[1] P. Agostini, F. Fabre, G. Mainfray, G. Petite, and N. K. Rahman, Free-free transitions following six-photon ionization of xenon atoms, Phys. Rev. Lett. **42**, 1127 (1979).

[2] W. Becker, F. Grasbon, R. Kopold, D. Miloevi, G. Paulus, and H. Walther, Above-threshold ionization: From classical features to quantum effects, volume 48 of *Advances In Atomic, Molecular, and Optical Physics*, pages 35 – 98, Academic Press, 2002.

[3] D. B. Milošević, G. G. Paulus, D. Bauer, and W. Becker, Above-threshold ionization by few-cycle pulses, Journal of Physics B: Atomic, Molecular and Optical Physics **39**, R203 (2006).

[4] T. Seideman, M. Y. Ivanov, and P. B. Corkum, Role of electron localization in intense-field molecular ionization, Phys. Rev. Lett. **75**, 2819 (1995).

[5] T. Zuo and A. D. Bandrauk, Charge-resonance-enhanced ionization of diatomic molecular ions by intense lasers, Phys. Rev. A **52**, R2511 (1995).

[6] A. Talebpour, C.-Y. Chien, and S. L. Chin, The effects of dissociative recombination in multiphoton ionization of O_2, Journal of Physics B: Atomic, Molecular and Optical Physics **29**, L677 (1996).

[7] C. Guo, M. Li, J. P. Nibarger, and G. N. Gibson, Single and double ionization of diatomic molecules in strong laser fields, Phys. Rev. A **58**, R4271 (1998).

[8] I. V. Litvinyuk, K. F. Lee, P. W. Dooley, D. M. Rayner, D. M. Villeneuve, and P. B. Corkum, Alignment-dependent strong field ionization of molecules, Phys. Rev. Lett. **90**, 233003 (2003).

[9] A. S. Alnaser, S. Voss, X. M. Tong, C. M. Maharjan, P. Ranitovic, B. Ulrich, T. Osipov, B. Shan, Z. Chang, and C. L. Cocke, Effects of molecular structure on ion disintegration patterns in ionization of O_2 and N_2 by short laser pulses, Phys. Rev. Lett. **93**, 113003 (2004).

[10] D. Pavičić, K. F. Lee, D. M. Rayner, P. B. Corkum, and D. M. Villeneuve, Direct measurement of the angular dependence of ionization for N_2, O_2, and CO_2 in intense laser fields, Phys. Rev. Lett. **98**, 243001 (2007).

[11] M. Lein, N. Hay, R. Velotta, J. P. Marangos, and P. L. Knight, Role of the intramolecular phase in high-harmonic generation, Phys. Rev. Lett. **88**, 183903 (2002).

[12] M. Lein, N. Hay, R. Velotta, J. P. Marangos, and P. L. Knight, Interference effects in high-order harmonic generation with molecules, Phys. Rev. A **66**, 023805 (2002).

[13] M. Lewenstein, P. Balcou, M. Y. Ivanov, A. L'Huillier, and P. B. Corkum, Theory of high-harmonic generation by low-frequency laser fields, Phys. Rev. A **49**, 2117 (1994).

[14] S. V. Popruzhenko, Keldysh theory of strong field ionization: history, applications, difficulties and perspectives, Journal of Physics B: Atomic, Molecular and Optical Physics **47**, 204001 (2014).

[15] A.-T. Le, H. Wei, C. Jin, and C. D. Lin, Strong-field approximation and its extension for high-order harmonic generation with mid-infrared lasers, Journal of Physics B: Atomic, Molecular and Optical Physics **49**, 053001 (2016).

[16] F. H. Faisal, Multiple absorption of laser photons by atoms, Journal of Physics B: Atomic and Molecular Physics **6**, L89 (1973).

[17] H. R. Reiss, Effect of an intense electromagnetic field on a weakly bound system, Phys. Rev. A **22**, 1786 (1980).

[18] A. Becker and F. H. M. Faisal, Intense-field many-body S-matrix theory, Journal of Physics B: Atomic, Molecular and Optical Physics **38**, R1 (2005).

[19] X. M. Tong, Z. X. Zhao, and C. D. Lin, Theory of molecular tunneling ionization, Phys. Rev. A **66**, 033402 (2002).

[20] M. S. Pindzola and F. Robicheaux, Time-dependent close-coupling calculations of correlated photoionization processes in helium, Phys. Rev. A **57**, 318 (1998).

[21] H. W. van der Hart and L. Feng, Double photoionization of excited He-like atoms, Journal of Physics B: Atomic, Molecular and Optical Physics **34**, L601 (2001).

[22] L. A. A. Nikolopoulos and P. Lambropoulos, Multichannel theory of two-photon single and double ionization of helium, Journal of Physics B: Atomic, Molecular and Optical Physics **34**, 545 (2001).

[23] J. S. Parker, B. J. S. Doherty, K. J. Meharg, and K. T. Taylor, Time delay between singly and doubly ionizing wavepackets in laser-driven helium, Journal of Physics B: Atomic, Molecular and Optical Physics **36**, L393 (2003).

[24] J. Feist, S. Nagele, R. Pazourek, E. Persson, B. I. Schneider, L. A. Collins, and J. Burgdörfer, Probing electron correlation via attosecond XUV pulses in the two-photon double ionization of helium, Phys. Rev. Lett. **103**, 063002 (2009).

[25] G. S. J. Armstrong, J. S. Parker, and K. T. Taylor, Double-electron above-threshold ionization resonances as interference phenomena, New Journal of Physics **13**, 013024 (2011).

[26] A. Liu and U. Thumm, Criterion for distinguishing sequential from nonsequential contributions to the double ionization of helium in ultrashort extreme-ultraviolet pulses, Phys. Rev. Lett. **115**, 183002 (2015).

[27] A. Zielinski, V. P. Majety, and A. Scrinzi, Double photoelectron momentum spectra of helium at infrared wavelength, Phys. Rev. A **93**, 023406 (2016).

[28] M. Iwai, S. Lee, and H. Nakamura, Electron correlation in doubly excited states of the hydrogen molecule, Phys. Rev. A **47**, 2686 (1993).

[29] I. Sánchez and F. Martín, The doubly excited states of the H_2 molecule, The Journal of Chemical Physics **106**, 7720 (1997).

[30] J. L. Sanz-Vicario, H. Bachau, and F. Martín, Time-dependent theoretical description of molecular autoionization produced by femtosecond xuv laser pulses, Phys. Rev. A **73**, 033410 (2006).

[31] M. F. Kling, C. Siedschlag, A. J. Verhoef, J. I. Khan, M. Schultze, T. Uphues, Y. Ni, M. Uiberacker, M. Drescher, F. Krausz, and M. J. J. Vrakking, Control of electron localization in molecular dissociation, Science **312**, 246 (2006).

[32] F. Kelkensberg, C. Lefebvre, O. G. W. Siu, T. T. Nguyen-Dang, O. Atabek, A. Keller, V. Serov, P. Johnsson, M. Swoboda, T. Remetter, A. L'Huillier, S. Zherebtsov, G. Sansone, E. Benedetti, F. Ferrari, M. Nisoli, F. Le'pine, M. F. Kling, and M. J. J. Vrakking, Molecular dissociative ionization and wave-packet dynamics studied using two-color XUV and IR pump-probe spectroscopy, Phys. Rev. Lett. **103**, 123005 (2009).

[33] G. Sansone, F. Kelkensberg, J. F. Pe'rez-Torres, F. Morales, M. F. Kling, W. Siu, O. Ghafur, P. Johnsson, M. Swoboda, E. Benedetti, F. Ferrari, F. Le'pine, J. L. Sanz-Vicario, S. Zherebtsov, I. Znakovskaya, A. L'Huillier, M. Y. Ivanov, M. Nisoli, F. Martín, and M. J. J. Vrakking, Electron localization following attosecond molecular photoionization, Nature **465**, 10 (2010).

[34] A. Fischer, A. Sperl, P. Cörlin, M. Schönwald, H. Rietz, A. Palacios, A. González-Castrillo, F. Martín, T. Pfeifer, J. Ullrich, A. Senftleben, and R. Moshammer, Electron localization involving doubly excited states in broadband extreme ultraviolet ionization of H_2, Phys. Rev. Lett. **110**, 213002 (2013).

[35] V. Roudnev, B. D. Esry, and I. Ben-Itzhak, Controlling HD^+ and H_2^+ dissociation with the carrier-envelope phase difference of an intense ultrashort laser pulse, Phys. Rev. Lett. **93**, 163601 (2004).

[36] F. Anis and B. D. Esry, Enhancing the intense field control of molecular fragmentation, Phys. Rev. Lett. **109**, 133001 (2012).

[37] T. Rathje, A. M. Sayler, S. Zeng, P. Wustelt, H. Figger, B. D. Esry, and G. G. Paulus, Coherent control at its most fundamental: Carrier-envelope-phase-dependent electron localization in photodissociation of a H_2^+ molecular ion beam target, Phys. Rev. Lett. **111**, 093002 (2013).

[38] N. G. Kling, K. J. Betsch, M. Zohrabi, S. Zeng, F. Anis, U. Ablikim, B. Jochim, Z. Wang, M. Kübel, M. F. Kling, K. D. Carnes, B. D. Esry, and I. Ben-Itzhak, Carrier-envelope phase control over pathway interference in strong-field dissociation of H_2^+, Phys. Rev. Lett. **111**, 163004 (2013).

[39] V. Fock, K. Norske Vidensk. Selsk. Forh. **31**, 138 (1958).

[40] J. Macek, Properties of autoionizing states of He, J. Phys. B: At. Mol. Phys. **831**, 1 (1968).

[41] C. D. Lin, Correlations of excited electrons. the study of channels in hyperspherical coordinates, Phys. Rev. A **10**, 1986 (1974).

[42] U. Fano, Dynamics of electron excitation, Phys. Today **29(9)**, 32 (1976).

[43] C. H. Greene, Adiabatic hyperspherical treatment of the H_2^+ molecule, Phys. Rev. A **26**, 2974 (1982).

[44] C. D. Lin, Radial and angular correlations of doubly excited electrons, Phys. Rev. A **25**, 76 (1982).

[45] C. D. Lin, Doubly excited states, including new classification schemes, Advances in Atomic Mol. Phys. **22**, 77 (1986).

[46] J. S. Avery, *Hyperspherical Harmonics: Applications in Quantum Theory*, Springer, 1989.

[47] A. Ohsaki and H. Nakamura, Hyperspherical coordinate approach to atom-diatom chemical reactions in the sudden and adiabatic approximations, Phys. Rep. **187**, 1 (1990).

[48] A. Bastida, A. Requena, and J. Zúñiga, Generalized hyperspherical coordinates for molecular vibrations, J. Phys. Chem. **97**, 5831 (1993).

[49] C. D. Lin, Hyperspherical coordinate approach to atomic and other coulombic three-body systems, Phys. Rep. **257**, 1 (1995).

[50] B. D. Esry, C. D. Lin, and C. H. Greene, Adiabatic hyperspherical study of the helium trimer, Phys. Rev. A **54**, 394 (1996).

[51] A. Kuppermann, Reactive scattering with row-orthonormal hyperspherical coordinates. 1. transformation properties and hamiltonian for triatomic systems, J. Phys. Chem. **100**, 2621 (1996).

[52] A. Kuppermann, Reactive scattering with row-orthonormal hyperspherical coordinates. 2. transformation properties and hamiltonian for tetraatomic systems, J. Phys. Chem. A **101**, 6368 (1997).

[53] V. Aquilanti and S. Cavalli, The quantum-mechanical hamiltonian for tetraatomic systems in symmetric hyperspherical coordinates, J. Chem. Soc., Faraday Trans., **93**, 801 (1997).

[54] B. D. Esry, C. H. Greene, and J. P. Burke, Recombination of three atoms in the ultracold limit, Phys. Rev. Lett. **83**, 1751 (1999).

[55] E. Nielsen and J. H. Macek, Low-energy recombination of identical bosons by three-body collisions, Phys. Rev. Lett. **83**, 1566 (1999).

[56] G. Nyman and H. Yu, Quantum theory of bimolecular chemical reactions, Rep. Prog. Phys. **63**, 1001 (2000).

[57] Y. Wang and B. D. Esry, Efimov trimer formation via ultracold four-body recombination, Phys. Rev. Lett. **102**, 133201 (2009).

[58] Y. Wang, *Universal Efimov Physics in Three- and Four-Body Collisions*, PhD thesis, Kansas State University.

[59] Y. Wang, J. P. D'Incao, and B. D. Esry, Cold three-body collisions in hydrogen-hydrogen-alkali-metal atomic systems, Phys. Rev. A **83**, 032703 (2011).

[60] D. Blume, Few-body physics with ultracold atomic and molecular systems in traps, Reports on Progress in Physics **75**, 046401 (2012).

[61] Y. Wang, J. P. DIncao, and B. D. Esry, Ultracold few-body systems, **62**, 1 (2013).

[62] E. Braaten and H.-W. Hammer, Universality in few-body systems with large scattering length, Physics Reports **428**, 259 (2006).

[63] Y. Wang and P. S. Julienne, Universal van der waals physics for three cold atoms near feshbach resonances, Nature Physics **10**, 768 (2014).

[64] A. Igarashi and C. D. Lin, Full ambiguity-free quantum treatment of D^++H(1s) charge transfer reactions at low energies, Phys. Rev. Lett. **83**, 4041 (1999).

[65] H. D. Cohen and U. Fano, Interference in the photo-ionization of molecules, Phys. Rev. **150**, 30 (1966).

[66] N. Stolterfoht, B. Sulik, V. Hoffmann, B. Skogvall, J. Y. Chesnel, J. Rangama, F. Frémont, D. Hennecart, A. Cassimi, X. Husson, A. L. Landers, J. A. Tanis, M. E. Galassi, and R. D. Rivarola, Evidence for interference effects in electron emission from H_2 colliding with $60 \text{MeV}/u$ Kr^{34+} ions, Phys. Rev. Lett. **87**, 023201 (2001).

[67] D. Rolles, M. Braune, S. Cvejanovic, O. Geszner, R. Hentges, S. Korica, B. Langer, T. Lischke, G. Prumper, A. Reinkoster, J. Viefhaus, B. Zimmermann, V. McKoy, and U. Becker, Isotope-induced partial localization of core electrons in the homonuclear molecule N_2, Nature **437**, 711 (2005).

[68] J. Fernández, O. Fojón, A. Palacios, and F. Martín, Interferences from fast electron emission in molecular photoionization, Phys. Rev. Lett. **98**, 043005 (2007).

[69] D. Akoury et al., The simplest double slit: interference and entanglement in double photoionization of H_2, Science **318**, 949 (2007).

[70] B. Zimmermann, D. Rolles, B. Langer, R. Hentges, M. Braune, S. Cvejanovic, O. Geszner, F. Heiser, S. Korica, T. Lischke, A. Reinkoster, J. Viefhaus, R. Dorner, V. McKoy, and U. Becker, Localization and loss of coherence in molecular double-slit experiments, Nat Phys **4**, 649 (2008).

[71] K. Kreidi et al., Interference in the collective electron momentum in double photoionization of H_2, Phys. Rev. Lett. **100**, 133005 (2008).

[72] M. Okunishi, R. Itaya, K. Shimada, G. Prümper, K. Ueda, M. Busuladžić, A. Gazibegović-Busuladžić, D. B. Milošević, and W. Becker, Two-source double-slit interference in angle-resolved high-energy above-threshold ionization spectra of diatoms, Phys. Rev. Lett. **103**, 043001 (2009).

[73] S. E. Canton, E. Plésiat, J. D. Bozek, B. S. Rude, P. Decleva, and F. Martín, Direct observation of youngs double-slit interferences in vibrationally resolved photoionization of diatomic molecules, Proceedings of the National Academy of Sciences **108**, 7302 (2011).

[74] T. Juffmann, A. Milic, M. Müllneritsch, P. Asenbaum, A. Tsukernik, J. Tüxen, M. Mayor, O. Cheshnovsky, and M. Arndt, Real-time single-molecule imaging of quantum interference, Nature Nanotechnology **7**, 297 (2012).

[75] R. K. Kushawaha, M. Patanen, R. Guillemin, L. Journel, C. Miron, M. Simon, M. N. Piancastelli, C. Skates, and P. Decleva, From double-slit interference to structural information in simple hydrocarbons, Proceedings of the National Academy of Sciences **110**, 15201 (2013).

[76] X.-J. Liu, Q. Miao, F. Gel'Mukhanov, M. Patanen, O. Travnikova, C. Nicolas, H. Ågren, K. Ueda, and C. Miron, Einstein–bohr recoiling double-slit gedanken experiment performed at the molecular level, Nature Photonics **9**, 120 (2015).

[77] E. Constant, H. Stapelfeldt, and P. B. Corkum, Observation of enhanced ionization of molecular ions in intense laser fields, Phys. Rev. Lett. **76**, 4140 (1996).

[78] J. Posthumus, The dynamics of small molecules in intense laser fields, Reports on Progress in Physics **67**, 623 (2004).

[79] A. Rudenko, B. Feuerstein, K. Zrost, V. L. B. de Jesus, T. Ergler, C. Dimopoulou, C. D. Schröter, R. Moshammer, and J. Ullrich, Fragmentation dynamics of molecular hydrogen in strong ultrashort laser pulses, Journal of Physics B: Atomic, Molecular and Optical Physics **38**, 487 (2005).

[80] T. Ergler, A. Rudenko, B. Feuerstein, K. Zrost, C. D. Schröter, R. Moshammer, and J. Ullrich, Time-resolved imaging and manipulation of H_2 fragmentation in intense laser fields, Phys. Rev. Lett. **95**, 093001 (2005).

[81] H. Xu, F. He, D. Kielpinski, R. Sang, and I. Litvinyuk, Experimental observation of the elusive double-peak structure in r-dependent strong-field ionization rate of H_2^+, Scientific Reports **5** (2015).

[82] U. Saalmann, C. Siedschlag, and J. Rost, Mechanisms of cluster ionization in strong laser pulses, Journal of Physics B: Atomic, Molecular and Optical Physics **39**, R39 (2006).

[83] K. J. Schafer, B. Yang, L. F. DiMauro, and K. C. Kulander, Above threshold ionization beyond the high harmonic cutoff, Phys. Rev. Lett. **70**, 1599 (1993).

[84] G. G. Paulus, W. Nicklich, H. Xu, P. Lambropoulos, and H. Walther, Plateau in above threshold ionization spectra, Phys. Rev. Lett. **72**, 2851 (1994).

[85] C. Blaga, F. Catoire, P. Colosimo, G. Paulus, H. Muller, P. Agostini, and L. DiMauro, Strong-field photoionization revisited, Nature Physics **5**, 335 (2009).

[86] R. B. Lehoucq, D. C. Sorensen, and C. Yang, `ARPACK` *users' guide: solution of large-scale eigenvalue problems with implicitly restarted Arnoldi methods*, SIAM, 1998.

[87] J. K. Cullum and R. A. Willoughby, *Lanczos algorithms for large symmetric eigenvalue computations: Vol. I: Theory*, SIAM, 2002.

[88] O. Schenk, K. Gärtner, and W. Fichtner, Efficient sparse lu factorization with left-right looking strategy on shared memory multiprocessors, BIT Numerical Mathematics **40**, 158 (2000).

[89] A. I. Kuleff, J. Breidbach, and L. S. Cederbaum, Multielectron wave-packet propagation: General theory and application, The Journal of Chemical Physics **123**, 044111 (2005).

[90] M. Aymar, C. H. Greene, and E. Luc-Koenig, Multichannel rydberg spectroscopy of complex atoms, Rev. Mod. Phys. **68**, 1015 (1996).

[91] Y. Yu and B. Esry, One-dimensional hydrogen molecule in hyperspherical representation, J. Chem. Phys. , (to be submitted) (2017).

[92] Y. Yu, M. Zohrabi, B. Berry, G. S. J. Armstrong, T. Severt, B. Jochim, P. Feizollah, K. R. P., J. Rajput, K. D. Carnes, B. D. Esry, and I. Ben-Itzhak, Strong-field molecular two-center effects beyond double-slit interference.

[93] Y. Yu and B. Esry, Low energy structure in molecular ionization, (in preparation) .

[94] Y. Yu and B. Esry, Nuclear-electronic coherence in strong-field dissociative ionization, (in preparation) .

[95] Y. Yu, S. Zeng, J. V. Hernández, Y. Wang, and B. D. Esry, Influence of the initial angular distribution on strong-field molecular dissociation, Phys. Rev. A **94**, 023423 (2016).

[96] Y. Yu and B. Esry, An optimized absorbing potential for ultrafast, strong-field problems, arXiv preprint arXiv:1710.04338 (2017).

[97] K. C. Kulander, F. H. Mies, and K. J. Schafer, Model for studies of laser-induced nonlinear processes in molecules, Phys. Rev. A **53**, 2562 (1996).

[98] T. Sharp, Potential-energy curves for molecular hydrogen and its ions, Atomic Data and Nuclear Data Tables **2**, 119 (1970).

[99] H. Feshbach, A unified theory of nuclear reactions .2., Ann. Phys. NY **19**, 287 (1962).

[100] M. Iwai, S. Lee, and H. Nakamura, Electron correlation in doubly excited states of the hydrogen molecule, Phys. Rev. A **47**, 2686 (1993).

[101] I. Sánchez and F. Martín, Representation of the electronic continuum of H_2 with b-spline basis, Journal of Physics B: Atomic, Molecular and Optical Physics **30**, 679 (1997).

[102] M. Shapiro and P. Brumer, Laser control of product quantum state populations in unimolecular reactions, The Journal of Chemical Physics **84**, 4103 (1986).

[103] M. Shapiro and P. Brumer, *Principles of the Quantum Control of Molecular Processes*, Wiley, 2003.

[104] B. D. Esry and H. R. Sadeghpour, Adiabatic formulation of heteronuclear hydrogen molecular ion, Phys. Rev. A **60**, 3604 (1999).

[105] D. A. Telnov and S.-I. Chu, Ab initio study of high-order harmonic generation of H_2^+ in intense laser fields: Time-dependent non-hermitian floquet approach, Phys. Rev. A **71**, 013408 (2005).

[106] L. Tao, C. W. McCurdy, and T. N. Rescigno, Grid-based methods for diatomic quantum scattering problems: A finite-element discrete-variable representation in prolate spheroidal coordinates, Phys. Rev. A **79**, 012719 (2009).

[107] C. Flammer, *Spheroidal wave functions*, Courier Corporation, 2014.

[108] J. Light, I. Hamilton, and J. Lill, Generalized discrete variable approximation in quantum mechanics, The Journal of Chemical Physics **82**, 1400 (1985).

[109] J. Colgan, M. S. Pindzola, and F. Robicheaux, Time-dependent studies of single and multiple photoionization of H_2^+, Phys. Rev. A **68**, 063413 (2003).

[110] M. W. J. Bromley and B. D. Esry, Classical aspects of ultracold atom wave packet motion through microstructured waveguide bends, Phys. Rev. A **69**, 053620 (2004).

[111] C. De Boor, C. De Boor, E.-U. Mathématicien, C. De Boor, and C. De Boor, *A practical guide to splines*, volume 27, Springer-Verlag New York, 1978.

[112] S. Blanes, F. Casas, J. Oteo, and J. Ros, The magnus expansion and some of its applications, Physics Reports **470**, 151 (2009).

[113] M. Nurhuda and F. H. M. Faisal, Numerical solution of time-dependent schrödinger equation for multiphoton processes: A matrix iterative method, Phys. Rev. A **60**, 3125 (1999).

[114] A. N. Grum-Grzhimailo, B. Abeln, K. Bartschat, D. Weflen, and T. Urness, Ionization of atomic hydrogen in strong infrared laser fields, Phys. Rev. A **81**, 043408 (2010).

[115] G. S. J. Armstrong, Y. Wang, and B. D. Esry, Unitary gauge-like transformations in nuclear laser-interaction hamiltonians, (to be submitted).

[116] F. Anis and B. D. Esry, Role of nuclear rotation in dissociation of H_2^+ in a short laser pulse, Phys. Rev. A **77**, 033416 (2008).

[117] M. Intel, Intel math kernel library, (2013).

[118] I. `MKL`. `PARDISO`, Parallel direct sparse solver interface, 2013.

[119] X. Guan, K. Bartschat, and B. I. Schneider, Breakup of the aligned h_2 molecule by xuv laser pulses: A time-dependent treatment in prolate spheroidal coordinates, Phys. Rev. A **83**, 043403 (2011).

[120] H. Friedrich, *Theoretical Atomic Physics*, volume 3rd Ed., Springer-Verlag Berlin Heidelberg, 2005.

[121] J. Muth-Böhm, A. Becker, and F. H. M. Faisal, Suppressed molecular ionization for a class of diatomics in intense femtosecond laser fields, Phys. Rev. Lett. **85**, 2280 (2000).

[122] P. Colosimo et al., Scaling strong-field interactions towards the classical limit, Nature Physics **4**, 386 (2008).

[123] P. B. Corkum, N. H. Burnett, and F. Brunel, Above-threshold ionization in the long-wavelength limit, Phys. Rev. Lett. **62**, 1259 (1989).

[124] W. Quan, Z. Lin, M. Wu, H. Kang, H. Liu, X. Liu, J. Chen, J. Liu, X. T. He, S. G. Chen, H. Xiong, L. Guo, H. Xu, Y. Fu, Y. Cheng, and Z. Z. Xu, Classical aspects in above-threshold ionization with a midinfrared strong laser field, Phys. Rev. Lett. **103**, 093001 (2009).

[125] T.-M. Yan, S. V. Popruzhenko, M. J. J. Vrakking, and D. Bauer, Low-energy structures in strong field ionization revealed by quantum orbits, Phys. Rev. Lett. **105**, 253002 (2010).

[126] C. Liu and K. Z. Hatsagortsyan, Origin of unexpected low energy structure in photoelectron spectra induced by midinfrared strong laser fields, Phys. Rev. Lett. **105**, 113003 (2010).

[127] S. Woutersen, U. Emmerichs, and H. Bakker, Femtosecond mid-IR pump-probe spectroscopy of liquid water: Evidence for a two-component structure, Science **278**, 658 (1997).

[128] B. Erk et al., Imaging charge transfer in iodomethane upon x-ray photoabsorption, Science **345**, 288 (2014).

[129] H. Ibrahim, B. Wales, S. Beaulieu, B. E. Schmidt, N. Thiré, E. P. Fowe, É. Bisson, C. T. Hebeisen, V. Wanie, M. Giguére, J.-C. Kieffer, M. Spanner, A. D. Bandrauk, J. Sanderson, M. S. Schuurman, and F. Légaré, Tabletop imaging of structural evolutions in chemical reactions demonstrated for the acetylene cation, Nat. Commun. **5**, 4422 (2014).

[130] G. Sansone et al., Electron localization following attosecond molecular photoionization, Nature **465**, 763 (2010).

[131] Y. Yu, S. Zeng, J. V. Hernández, Y. Wang, and B. D. Esry, Influence of the initial angular distribution on strong-field molecular dissociation, Phys. Rev. A **94**, 023423 (2016).

[132] F. Anis, T. Cackowski, and B. D. Esry, Rotational dynamics of dissociating H_2^+ in a short intense laser pulse, Journal of Physics B: Atomic, Molecular and Optical Physics **42**, 091001 (2009).

[133] M. Zohrabi, *Quantum control of molecular fragmentation in strong laser field*, PhD thesis, Kansas State University, 2014.

[134] R. Heather and H. Metiu, An efficient procedure for calculating the evolution of the wave function by fast fourier transform methods for systems with spatially extended wave function and localized potential, The Journal of Chemical Physics **86**, 5009 (1987).

[135] L. Tao and A. Scrinzi, Photo-electron momentum spectra from minimal volumes: the time-dependent surface flux method, New Journal of Physics **14**, 013021 (2012).

[136] F. Morales, T. Bredtmann, and S. Patchkovskii, isurf: a family of infinite-time surface flux methods, Journal of Physics B: Atomic, Molecular and Optical Physics **49**, 245001 (2016).

[137] R. Kosloff and D. Kosloff, Absorbing boundaries for wave propagation problems, Journal of Computational Physics **63**, 363 (1986).

[138] A. Vibok and G. G. Balint-Kurti, Reflection and transmission of waves by a complex potentiala semiclassical jeffreyswentzelkramersbrillouin treatment, The Journal of Chemical Physics **96**, 7615 (1992).

[139] A. Vibok and G. G. Balint-Kurti, Parametrization of complex absorbing potentials for time-dependent quantum dynamics, The Journal of Physical Chemistry **96**, 8712 (1992).

[140] D. Macias, S. Brouard, and J. Muga, Optimization of absorbing potentials, Chemical Physics Letters **228**, 672 (1994).

[141] U. V. Riss and H. Meyer, Investigation on the reflection and transmission properties of complex absorbing potentials, The Journal of Chemical Physics **105**, 1409 (1996).

[142] J.-Y. Ge and J. Z. H. Zhang, Use of negative complex potential as absorbing potential, The Journal of Chemical Physics **108**, 1429 (1998).

[143] A. N. Hussain and G. Roberts, Procedure for absorbing time-dependent wave functions at low kinetic energies and large bandwidths, Phys. Rev. A **63**, 012703 (2000).

[144] D. E. Manolopoulos, Derivation and reflection properties of a transmission-free absorbing potential, The Journal of Chemical Physics **117**, 9552 (2002).

[145] B. Poirier and T. Carrington, Semiclassically optimized complex absorbing potentials of polynomial form. ii. complex case, The Journal of Chemical Physics **119**, 77 (2003).

[146] J. Muga, J. Palao, B. Navarro, and I. Egusquiza, Complex absorbing potentials, Physics Reports **395**, 357 (2004).

[147] M. Tarana and C. H. Greene, Femtosecond transparency in the extreme-ultraviolet region, Phys. Rev. A **85**, 013411 (2012).

[148] V. V. Strelkov, M. A. Khokhlova, A. A. Gonoskov, I. A. Gonoskov, and M. Y. Ryabikin, High-order harmonic generation by atoms in an elliptically polarized laser field: Harmonic polarization properties and laser threshold ellipticity, Phys. Rev. A **86**, 013404 (2012).

[149] L. Yue and L. B. Madsen, Dissociation and dissociative ionization of $h_2{}^+$ using the time-dependent surface flux method, Phys. Rev. A **88**, 063420 (2013).

[150] P. Krause, J. A. Sonk, and H. B. Schlegel, Strong field ionization rates simulated with time-dependent configuration interaction and an absorbing potential, The Journal of Chemical Physics **140** (2014).

[151] J. L. Krause, K. J. Schafer, and K. C. Kulander, Calculation of photoemission from atoms subject to intense laser fields, Phys. Rev. A **45**, 4998 (1992).

[152] T. N. Rescigno, M. Baertschy, W. A. Isaacs, and C. W. McCurdy, Collisional breakup in a quantum system of three charged particles, Science **286**, 2474 (1999).

[153] T. N. Rescigno and C. W. McCurdy, Numerical grid methods for quantum-mechanical scattering problems, Phys. Rev. A **62**, 032706 (2000).

[154] F. He, C. Ruiz, and A. Becker, Absorbing boundaries in numerical solutions of the time-dependent schrödinger equation on a grid using exterior complex scaling, Phys. Rev. A **75**, 053407 (2007).

[155] L. Tao, W. Vanroose, B. Reps, T. N. Rescigno, and C. W. McCurdy, Long-time solution of the time-dependent schrödinger equation for an atom in an electromagnetic field using complex coordinate contours, Phys. Rev. A **80**, 063419 (2009).

[156] A. Scrinzi, Infinite-range exterior complex scaling as a perfect absorber in time-dependent problems, Phys. Rev. A **81**, 053845 (2010).

[157] E. Y. Sidky and B. D. Esry, Boundary-free propagation with the time-dependent schrödinger equation, Phys. Rev. Lett. **85**, 5086 (2000).

[158] A. Hamido, J. Eiglsperger, J. Madroñero, F. Mota-Furtado, P. O'Mahony, A. L. Frapiccini, and B. Piraux, Time scaling with efficient time-propagation techniques for atoms and molecules in pulsed radiation fields, Phys. Rev. A **84**, 013422 (2011).

[159] H. Miyagi and L. B. Madsen, Exterior time scaling with the stiffness-free lanczos time propagator: Formulation and application to atoms interacting with strong midinfrared lasers, Phys. Rev. A **93**, 033420 (2016).

[160] J. Z. H. Zhang, New method in timedependent quantum scattering theory: Integrating the wave function in the interaction picture, The Journal of Chemical Physics **92**, 324 (1990).

[161] C. J. Williams, J. Qian, and D. J. Tannor, Dynamics of triatomic photodissociation in the interaction representation. Is. methodology, The Journal of Chemical Physics **95**, 1721 (1991).

[162] G. H. Yao and S. I. Chu, Time-dependent multiphoton dynamics in intense short-pulse laser fields. Interaction-representation approach, Chem. Phys. Lett. **198**, 39 (1992).

[163] S. Yoshida, S. Watanabe, C. O. Reinhold, and J. Burgdörfer, Reflection-free propagation of wave packets, Phys. Rev. A **60**, 1113 (1999).

[164] C. W. McCurdy, D. A. Horner, and T. N. Rescigno, Practical calculation of amplitudes for electron-impact ionization, Phys. Rev. A **63**, 022711 (2001).

[165] B. I. Schneider, L. A. Collins, and S. X. Hu, Parallel solver for the time-dependent linear and nonlinear schrödinger equation, Phys. Rev. E **73**, 036708 (2006).

[166] G. Pöschl and E. Teller, Bemerkungen zur Quantenmechanik des anharmonischen Oszillators, Zeitschrift fur Physik **83**, 143 (1933).

[167] L. D. Landau and E. M. Lifshitz, *Quantum Mechanics: None-Relativistic Theory*, Pergamon Press, 1977.

[168] B. I. Schneider, J. Feist, S. Nagele, R. Pazourek, S. Hu, L. A. Collins, and J. Burgdörfer, Recent advances in computational methods for the solution of the time-dependent schrödinger equation for the interaction of short, intense radiation with one and two electron system: application to He and H_2^+, in *Quantum Dynamic Imaging: Theoretical and Numerical Methods*, edited by A. D. Bandrauk and M. Ivanov, Springer Science & Business Media, 2011.

[169] B. D. Esry, *MANY-BODY EFFECTS IN BOSE-EINSTEIN CONDENSATES*, PhD thesis, University of Colorado, 1997.

[170] E. Anderson et al., `LAPACK` *Users' guide*, SIAM, 1999.

[171] C. B. Madsen, *Molecules in intense laser fields: studies of ionization, high-order harmonic generation and alignment*, PhD thesis, University of Aarhus, 2010.

[172] J. P. Boyd, *Chebyshev and Fourier spectral methods*, Courier Corporation, 2001.

[173] M. Abramowitz et al., *Handbook of mathematical functions with formulas, graphs, and mathematical tables*, volume 9, Dover, New York, 1972.

Appendix A

Reflection coefficients

A.1 Reflection coefficient for single-exponential CAP

We start from the Schrödinger equation for the single-exponential CAP:

$$\left[-\frac{\hbar^2}{2m}\frac{d^2}{dx^2} - \frac{\alpha^2\hbar^2}{2m}e^{-x/\beta}\right]\psi = E\psi = \frac{\hbar^2 k^2}{2m}\psi. \tag{A.1}$$

Setting $z = x/\beta$ gives

$$\left[-\frac{d^2}{dz^2} - \lambda^2 e^{-z}\right]\psi = K^2\psi, \tag{A.2}$$

where $\lambda \equiv \alpha\beta$ and $K \equiv k\beta$. We define

$$\xi = 2\lambda e^{-z/2},$$

so that Eq. (A.2) becomes

$$\left[\xi^2\frac{d^2}{d\xi^2} + \xi\frac{d}{d\xi} + \xi^2 + 4K^2\right]\psi = 0. \tag{A.3}$$

This is Bessel's equation; the general solution is thus

$$\psi = CJ_{2iK}(\xi) + DJ_{-2iK}(\xi). \tag{A.4}$$

To obtain the reflection coefficient, we need C and D and we need to analyze the asymptotic behavior of these solutions. Starting with the latter, the $z \to \infty$ ($x \to \infty$) behavior

can be found from the $\xi \to 0$ expansions,

$$J_{2iK}(\xi) \xrightarrow[z \to \infty]{} \frac{\lambda^{2iK}}{\Gamma(1 + 2iK)} e^{-iKz}$$

$$J_{-2iK}(\xi) \xrightarrow[z \to \infty]{} \frac{\lambda^{-2iK}}{\Gamma(1 - 2iK)} e^{iKz}. \tag{A.5}$$

To find C and D, we impose the $x = 0$ boundary condition,

$$\psi(x = 0) = \psi(z = 0) = \psi(\xi = 2\lambda) = 0. \tag{A.6}$$

Thus,

$$D = -\frac{J_{2iK}(2\lambda)}{J_{-2iK}(2\lambda)} C. \tag{A.7}$$

Finally, the asymptotic solution reads

$$\psi \xrightarrow[z \to \infty]{} C \left[\frac{\lambda^{2iK}}{\Gamma(1 + 2iK)} e^{-iKz} - \frac{\lambda^{-2iK}}{\Gamma(1 - 2iK)} \frac{J_{2iK}(2\lambda)}{J_{-2iK}(2\lambda)} e^{iKz} \right]. \tag{A.8}$$

From this expression, the reflection coefficient can be found to be

$$R = e^{4K \arg \lambda^2} \left| \frac{J_{2iK}(2\lambda)}{J_{-2iK}(2\lambda)} \right|^2. \tag{A.9}$$

Note that if λ is real, then $R \equiv 1$ as it should with no absorption.

A.2 Reflection coefficient for double-exponential CAP

As in App. A.1, we start from a unitless Schrödinger equation,

$$\left[-\frac{d^2}{dz^2} - \lambda_1^2 e^{-z/2} - i\lambda_2^2 e^{-z} \right] \psi = K^2 \psi. \tag{A.10}$$

with

$$z = \frac{x}{\beta} \qquad \lambda_1 = \alpha_1 \beta \qquad \lambda_2 = \alpha_2 \beta \qquad K = k\beta. \tag{A.11}$$

We assume both λ_i are real, making the longer-range potential real in accord with the discussion in the text. That is, the real potential accelerates the wave before it encounters the absorbing potential.

Defining

$$\xi = 2\lambda_2 e^{-\frac{z}{2}} \qquad \text{and} \qquad \Lambda = \frac{\lambda_1^2}{\lambda_2}, \tag{A.12}$$

we get

$$\left[\xi^2 \frac{d^2}{d\xi^2} + \xi \frac{d}{d\xi} + 2\Lambda\xi + i\xi^2 + 4K^2\right]\psi = 0 \tag{A.13}$$

This form of the equation makes clear the motivation for our choice of potential: having one potential being the square of the other (in form) produces the polynomial in ξ seen in the equation. Since the polynomial is quadratic, the equation has analytic solutions.

Setting $\gamma = e^{i\pi/4}$ and $\eta = \frac{1}{2} - \gamma\Lambda$, the solution can be written as

$$\psi = e^{\gamma^3\xi + 2iK\ln\xi}\left[C\, U(\eta + 2iK, 1 + 4iK, -2\gamma^3\xi) + D\, L_{-\eta-2iK}^{4iK}(-2\gamma^3\xi)\right], \tag{A.14}$$

where U and L are the confluent hypergeometric and Laguerre functions, respectively.

Analyzing the asymptotic behavior, we have

$$e^{\gamma^3\xi + 2iK\ln\xi}U \xrightarrow[z\to\infty]{} \frac{(2\lambda_2)^{2iK}\Gamma(-4iK)}{\Gamma(\eta - 2iK)}e^{-iKz} + \frac{(2\lambda_2)^{-2iK}2^{-4iK}e^{-\pi K}\Gamma(4iK)}{\Gamma(\eta + 2iK)}e^{iKz}$$

$$e^{\gamma^3\xi + 2iK\ln\xi}L \xrightarrow[z\to\infty]{} (2\lambda_2)^{2iK}L_{-\eta-2iK}^{4iK}(0)e^{-iKz}. \tag{A.15}$$

The boundary condition $\psi(x = 0) = 0$ gives

$$D = -\frac{U(\eta + 2iK, 1 + 4iK, -4\lambda_2\gamma^3)}{L_{-\eta-2iK}^{4iK}(-4\lambda_2\gamma^3)}C. \tag{A.16}$$

The reflection coefficient can now be extracted, and a little algebra applied, to give

$$R = \left|\frac{{}_1F_1(\eta + 2iK, 1 + 4iK, -4\gamma^3\lambda_2)}{{}_1F_1(\eta - 2iK, 1 - 4iK, -4\gamma^3\lambda_2)}\right|^2. \tag{A.17}$$

For a purely real V (*i.e.*, $\lambda_2 \to 0$), we recover $R = 1$ as we should. For $\lambda_1 = 0$, R reduces to the single-exponential expression Eq. (A.9) with λ purely imaginary.

A.3 Reflection coefficient for $-i\alpha_2^2/x^2$ **CAP**

We start from the Schrödinger equation

$$\left[-\frac{\hbar^2}{2m}\frac{d^2}{dx^2} - \frac{\hbar^2}{2m}\frac{ia^2 + \frac{1}{4}}{x^2}\right]\psi = \frac{\hbar^2}{2m}k^2\psi. \tag{A.18}$$

Defining $z = kx$, we must solve

$$\left[-\frac{d^2}{dz^2} - \frac{ia^2 + \frac{1}{4}}{z^2}\right]\psi = \psi. \tag{A.19}$$

The general solution is

$$\psi = \sqrt{z}\left[CJ_{a/\gamma}(z) + DJ_{-a/\gamma}(z)\right] \tag{A.20}$$

with $\gamma = e^{i\pi/4}$ as before. Since we require $\psi(0)=0$, we need the small-z behavior of the Bessel functions

$$J_\nu(z) \xrightarrow[z\to 0]{} \frac{1}{\Gamma(1+\nu)}\left(\frac{z}{2}\right)^\nu. \tag{A.21}$$

For the general case of complex a, $a = a_r + ia_i$, one can show that requiring the real part of the potential to be attractive and the imaginary part to be absorbing leads to

$$a_r > 0 \text{ and } a_i < 0 \text{ with } |a_r| > |a_i|. \tag{A.22}$$

These conditions, together with Eq. (A.21), require us to set $D=0$.

Finally, using the large-z behavior of the Bessel function,

$$\sqrt{z}J_{a/\gamma}(z) \xrightarrow[z\to\infty]{} \sqrt{\frac{2}{\pi}}\cos\left(\frac{\pi}{4} + \frac{a\pi}{2\gamma} - z\right), \tag{A.23}$$

allows us to extract the reflection coefficient,

$$R = e^{-\sqrt{2}\pi(a_r - a_i)}. \tag{A.24}$$

Keeping in mind that $a_i < 0$ under the conditions we have assumed, this equation shows that both the real and imaginary parts of the CAP contribute to decreasing the final absorption. We also see that this equation is identical to Eq. (6.20) once the conversion from a to λ_2 is made.

Effect of truncation

If we are willing to sacrifice the energy independence of R at small energies by truncating the CAP at x_0,

$$V = \begin{cases} -\frac{\hbar^2}{2m}\frac{ia^2 + \frac{1}{4}}{x^2} & x \leqslant x_0 \\ 0 & x > x_0 \end{cases}, \tag{A.25}$$

then one can again obtain an analytic expression for the reflection coefficient.

The wave function is

$$\psi = \begin{cases} AF(z) & z \leqslant z_0 \\ Ce^{-i(z-z_0)} + De^{i(z-z_0)} & z > z_0 \end{cases} \tag{A.26}$$

with $z_0 = kx_0$ and $F(z) = \sqrt{z}J_{a/\gamma}(z)$. The reflection coefficient is thus

$$R = \left|\frac{D}{C}\right|^2 = \left|\frac{F(z_0) - iF'(z_0)}{F(z_0) + iF'(z_0)}\right|^2. \tag{A.27}$$

The notation F' indicates a derivative with respect to z, $F' = dF/dz$, and the log-derivative of F at z_0 is

$$\left.\frac{F'}{F}\right|_{z=z_0} = \frac{1 - 2a/\gamma}{2z_0} + \frac{J_{a/\gamma-1}(z_0)}{J_{a/\gamma}(z_0)}. \tag{A.28}$$

A plot of the reflection coefficient from Eq. (A.27) looks qualitatively like the double-sinh reflection coefficients in Figs. 6.7 and 6.10. However, instead of falling exponentially with k at small k, it falls more slowly—like $1/z_0^4 = 1/(kx_0)^4$. In addition, because of the sharp cutoff in the potential, R oscillates in z_0 with minima separated by π at positions corresponding roughly to $z_0 = kx_0 = n\pi$.

Appendix B

Complex boundary condition

B.1 Zero potential

It is easiest to understand the effect of the complex boundary condition (b is complex)

$$\frac{1}{\psi}\frac{d\psi}{dx} = b \tag{B.1}$$

from the free-particle equation

$$-\frac{d^2}{dz^2}\psi = K^2\psi \tag{B.2}$$

in the same unitless notation as in the previous appendices. In this notation, we must require

$$\frac{1}{\psi}\frac{d\psi}{dz} = B, \tag{B.3}$$

where $B = b\beta$. The solution is, as usual,

$$\psi = Ce^{iKz} + De^{-iKz}. \tag{B.4}$$

When combined with the boundary condition, one finds

$$R = \left|\frac{B + iK}{B - iK}\right|^2. \tag{B.5}$$

As discussed in the text, this R goes to zero at $K = K_0$ when $B = -iK_0$. Physically, this condition corresponds to setting an outgoing-wave boundary condition (on the left boundary) for an incident momentum K_0. The boundary is thus perfectly transparent at this momentum, but imperfectly so at other momenta.

B.2 Effect on bound states

It is natural to ask what effect such a boundary condition might have on the energies of any bound states in the system. One general way to answer this question is to consider an arbitrary potential at $z = 0$ and write

$$\psi = \begin{cases} AF(z) & z \leqslant z_0 \\ Ce^{-\kappa(z-z_0)} + De^{\kappa(z-z_0)} & z > z_0 \end{cases} \tag{B.6}$$

with $\kappa = \beta\sqrt{2m|E|/\hbar^2}$ and $F(z)$ the energy-dependent solution appropriate to the arbitrary potential satisfying the required boundary condition at $z = 0$. Although this specific description assumes a short-range potential, a similar argument can be made for the Coulomb potential.

The wave function in Eq. (B.6) must satisfy the log-derivative boundary condition from Eq. (B.3) at $z = z_1$ — this is why the exponentially-growing solution must be retained. Imposing this boundary condition leads to the following transcendental equation for the energy of the bound state:

$$F'(z_0) + \kappa F(z_0) = \frac{B + \kappa}{B - \kappa}\big[F'(z_0) - \kappa F(z_0)\big]e^{-2\kappa(z_1-z_0)}. \tag{B.7}$$

This equation should be compared with the physical quantization condition

$$F'(z_0) + \kappa F(z_0) = 0, \tag{B.8}$$

to which Eq. (B.7) reduces in the $z_1 \to \infty$ limit as it should.

Since in any practical numerical solution of the TDSE the boundary of the numerical grid must be large compared to the size of the bound state, we will have $z_1 \gg z_0$. Therefore, so long as $B - \kappa \neq 0$, the exponential term on the right-hand-side of Eq. (B.7) will dominate — and thus make Eq. (B.7) a very good approximation to Eq. (B.8) — guaranteeing that the real part of the energy found with the complex boundary condition will be very close to the physical energy. To be sure, it will acquire a small imaginary part reflecting the decay of the ground state due to the complex boundary condition, but it should be completely negligible.

This result for the bound-state energies is completely consistent with the intuitive notion that the effect of the complex boundary condition — indeed the CAPs, too — on the bound states should be negligible so long as the bound-state wave function is vanishingly small at the boundary $z = z_1$ (or in the absorbing region of the CAP).

B.3 Single- and double-exponential CAPs

The reflection coefficient for the single-exponential CAP with a complex boundary condition is still analytical. It is found by imposing Eq. (B.3) on the general solution for the

single-exponential CAP from Eq. (A.4). After a little algebra, one obtains

$$R = e^{4K \arg \lambda^2} \left| \frac{(B + iK) J_{2iK}(2\lambda) - \lambda J_{1+2iK}(2\lambda)}{(B - iK) J_{-2iK}(2\lambda) - \lambda J_{1-2iK}(2\lambda)} \right|^2. \tag{B.9}$$

The same procedure can be carried out for the double-exponential CAP using the general solution from Eq. (A.14) to find

$$R = \left| \frac{(B+iK+\gamma^3\lambda_2)\, _1F_1(\eta+2iK, 1+4iK, -4\gamma^3\lambda_2) - 2\gamma^3\lambda_2(\eta+2iK)\, _1F_1(\eta+2iK+1, 2+4iK, -4\gamma^3\lambda_2)/(1+4iK)}{(B + iK + \gamma^3\lambda_2)\, _1F_1(\eta - 2iK, 1 - 4iK, -4\gamma^3\lambda_2) - 2iK\, _1F_1(\eta - 2iK, -4iK, -4\gamma^3\lambda_2)} \right|^2. \tag{B.10}$$

Note that both Eq. (B.9) and Eq. (B.10) reduce to the reflection coefficient with $\psi = 0$ in the $B \to \infty$ limit as they should.

Appendix C

Spatial representations

C.1 Basis splines representation

Using the B-splines representation to solve the Schrödinger equation has already been detailedly documented previously [111, 169]. Here we will provide a brief summary. The basic idea of the B-splines method is to represent the unknown wave function by a linear combination of locally defined polynomials, the splines. For example, a two-dimensional wave function $\Psi(x, y)$ could be written as

$$\Psi(x, y) = \sum_{i,j} c_{ij} u_i(x) v_j(y) \tag{C.1}$$

where u_i/v_j are the splines. For nth-order splines, the local polynomials are defined such that the function and its derivative up to $n - 1$ orders are continuous. An example of the 5th-order splines are shown in Fig. C.1 on a 11-points grid uniformly distributed for $0 \leqslant x \leqslant 1$. The thick spline in Fig. C.1 is identically zero for $x \leqslant 0.2$ and $x \geqslant 0.8$, and its function and up to 4th-order derivatives are continuous within the range $0.2 \leqslant x \leqslant 0.8$. By applying Eq. (C.1) to the time-dependent Schrödinger equation (TDSE) in Sec.3.1 and projecting out the two-dimensional splines, one derives the Schrödinger equation in B-splines representation. The matrix form of the resulting equation reads like Eq. (3.14).

In B-splines, each spline only interacts with the nearest n (the order) splines. This special property leads to banded matrices for the Hamiltonian and the overlap, making the eigenvalue problem in the time-independent Schrödinger equation or the linear equation in the time-dependent Schrödinger equation readily solvable either using `ARPACK` banded matrix routines [86], or `LAPACK` banded matrix routines [170].

Finally, we need to address the imposition of boundary conditions, which is straightforward in B-splines. We only consider three cases: no boundary, $Psi = 0$, and $Psi' = 0$. First, no boundary condition requires no action, as in Fig. C.1. Second, for zero wave function boundary condition, one simply remove the left-most or the right-most spline. Finally, for zero derivative boundary condition, last two splines on the boundary need to be replaced with one spline—the average of the two.
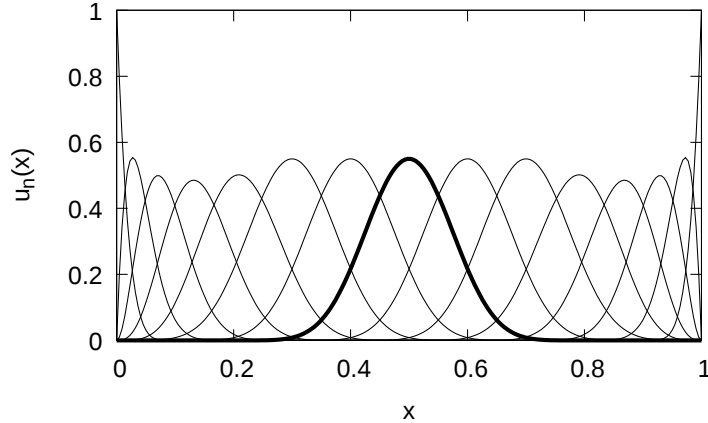
Figure C.1: *The basis splines $u_n(x)$ on a uniform grid. The thick line indicates the spline that is nonzero only for $0.2 < x < 0.8$.*

C.2   Finite-element discrete variable representation

The contents in this section are adapted from a note originally from Brett Esry. One other similar version has appeared in the PhD thesis by Christian Madsen [171].

We want to write down the details of using finite-element discrete variable representation (FEDVR) to solve one-dimensional time-independent Schrödinger equation, as in Sec. 6.2. It's trivial to adapt it to the time-dependent Schrödinger equation. The generalization to higher dimensions using the direct-product form for the wave function is also straightforward.

The idea of FEDVR is to take a domain [a,b] and split it into a number of elements, N_e. Then, within each element, expand the solution on a cardinal function basis giving the discrete variable representation (DVR). The solution will be matched at each boundary between elements, but we will only match the function, not the derivative. The book on spectral elements—the engineering term for FEDVR—by Boyd [172] has many details, but we will give the ones specific to our applications. First, the basis functions, or the cardinal functions are required to have the property

$$u_n(x_i) = \delta_{ni} \tag{C.2}$$

where i runs from 1 to N over the grid points in a given element, and n runs from 1 to N over all elements of basis. For the following discussions, we will assume each element $[x_j, x_{j+1}]$ has been mapped to the logical domain $[-1, +1]$ using

$$x = \frac{x_{j+1} - x_j}{2}y + \frac{x_{j+1} + x_j}{2}, \ y \subseteq [-1, 1]. \tag{C.3}$$

We write our basis function as

$$u_n(y) = \frac{(1-y^2)\phi'_{N-2}(y)}{[(1-y_n^2)\phi_{N-2}(y_n)]'(y-y_n)},$$ (C.4)

where the ϕ_n's are the orthogonal polynomials of the *Gauss-Lobatto* quadrature (see Page 888 of Ref. [173]) with the end points fixed at ± 1. The grid points y_n are chosen as the zeros of one of the ϕ_n's. This connection is what makes this a DVR approach and is also what it ties to Lobatto quadrature.

To solve the Schrödinger equation, we need to expand the wave function as

$$\Psi(x) = \sum_{jn} c_{jn} u_n^j(x)$$ (C.5)

where j is the element label to indicate where the u_n is defined. Note that $\Psi(x_n^j) = c_{jn}$. Continuity of the wave function at element boundaries requires

$$\Psi|_{x=x_{j-}} = \Psi|_{x=x_{j+}}, \text{ thus } c_{jN} = c_{j+1,1}$$ (C.6)

So,

$$\Psi = \sum_{j=2}^{N_e-1} \left[\sum_{n=2}^{N-1} c_{jn} u_n^j + c_{jN}(u_N^j + u_1^{j+1}) \right] + \sum_{n=2}^{N} c_{N_e n} u_n^{N_e} + \sum_{n=1}^{N-1} c_{1n} u_n^1$$ (C.7)

Applying the variational principle for the c's gives

$$\boldsymbol{Hc} = E\boldsymbol{Sc}$$ (C.8)

The overlap matrix is

$$S_{\alpha\beta} = < u_{n'}^{j'}|u_n^j > = \delta_{j'j} < u_{n'}^j|u_n^j >$$
$$= \delta_{j'j} \int_{x_j}^{x_{j+1}} dx u_{n'}^j(x) u_n^j(x) \rho(x) = \delta_{j'j} \frac{x_{j+1}-x_j}{2} w_n \rho_n \delta_{n'n}$$ (C.9)

with ρ as the volume element and w as the weights of the *Gauss-Lobatto* quadrature. This applies to all cases except $n = 1$ or N. In these cases, we need

$$S_{\alpha\beta} = < u_N^{j'} + u_1^{j'+1}|u_n^j > = \delta_{j'j} \frac{x_{j+1}-x_j}{2} w_N \rho_N \delta_{nN} + \delta_{j'+1,j} \frac{x_{j+1}-x_j}{2} w_1 \rho_1 \delta_{n1}$$ (C.10)

and,

$$S_{\alpha\beta} = < u_N^{j'} + u_1^{j'+1}|u_N^j + u_1^{j+1} > = \delta_{j'j} \frac{x_{j+1}-x_j}{2} w_N \rho_N + \delta_{j'j} \frac{x_{j+2}-x_{j+1}}{2} w_1 \rho_1$$ (C.11)

Inspection of these expressions and the form of Ψ shows that the overlap matrix consists

of diagonal $N \times N$ block matrices in one element, and they overlap at the corners due to continuity.

Next, we evaluate the Hamiltonian which consists of the kinetic energy matrix and the potential energy matrix. The kinetic energy matrix elements can be evaluated within each element, then the total matrix constructed as

$$T^j_{n'n} = \; < u_{n'}|T|u_n > \; = -\frac{1}{2\mu} \int_{x'_j}^{x_{j+1}} dx \rho u_{n'}(x) \frac{1}{\rho} \frac{d}{dx} (\rho \frac{d}{dx}) u_n(x) \tag{C.12}$$

$$= -\frac{1}{2\mu} \frac{2}{x_{j+1} - x_j} [\delta_{n'N} \rho(x_{j+1}) u_n(1) - \delta_{n'1} \rho(x_j) u_{n'}(-1)]$$

$$+ \frac{1}{2\mu} \frac{2}{x_{j+1} - x_j} \int_{-1}^{1} \rho dy u'_{n'} u'_n \tag{C.13}$$

The question is whether the surface terms survive when we build the full kinetic energy matrix. To answer this question, the argument generally proceeds as follows: if one integrate the kinetic energy by parts on the whole domain boundaries $[x_1, x_{N_e+1}]$, all bases satisfy $u = 0$ or $u' = 0$ at the domain boundaries (or $\rho = 0$) so the surface terms at x_1 and x_{N_e+1} do vanish. The kinetic energy matrix elements are then simply taken to be the above results minus the surface terms. This is called the weak form of the differential equation, while the second derivative — as in Eq. (C.12) — is the strong form. The weak form is used for basis functions with discontinuous first derivatives. Thus

$$T^j_{n'n} = \frac{1}{2\mu} \frac{2}{x_{j+1} - x_j} \sum_{i=1}^{N} \rho_i w_i u'_{n'}(y_i) u'_n(y_i) \tag{C.14}$$

and the full kinetic energy matrix is composed of these elemental T-matrices. Finally the potential energy is simply

$$< u^{j'}_{n'}|V|u^j_n > \; = \delta_{j'j} \delta_{n'n} \frac{x_{j+1} - x_j}{2} w_n \rho_n V_n, \tag{C.15}$$

like the overlap matrix.

We thus have Eq. C.8 with $\boldsymbol{S}$ diagonal and $\boldsymbol{H}$ banded. We convert this to a standard eigenvalue problem using Cholesky decomposition

$$\boldsymbol{S} = \boldsymbol{L}\boldsymbol{L}^T, \boldsymbol{L} = \boldsymbol{S}^{\frac{1}{2}} \tag{C.16}$$

So,

$$\boldsymbol{H}\boldsymbol{c} = E\boldsymbol{S}\boldsymbol{c} \Rightarrow \boldsymbol{L}^{-1}\boldsymbol{H}\boldsymbol{L}^{-T}\boldsymbol{L}^T\boldsymbol{c} = E\boldsymbol{L}^T\boldsymbol{c} \Rightarrow \tilde{\boldsymbol{H}}\boldsymbol{d} = E\boldsymbol{d} \tag{C.17}$$

with $\tilde{\boldsymbol{H}} = \boldsymbol{L}^{-1}\boldsymbol{H}\boldsymbol{L}^{-T}$ and $\boldsymbol{d} = \boldsymbol{L}^T\boldsymbol{c}$.

One last thing need to be addressed is the boundary conditions. We again consider three cases: $\Psi = 0$, $\Psi' = 0$, and no boundary condition (for $\rho = 0$). To impose $\Psi = 0$, we simply

leave out u_1 in the left-most or u_N in the right-most. For $\Psi' = 0$, we impose no boundary conditions since Lobatto quadrature is used. When $\rho = 0$, we also make no restrictions on Ψ, but use Radau quadrature instead of Lobatto. The reason is that $\rho = 0$ introduces a singularity via $\boldsymbol{S}$, and we don't want a grid point where $\rho = 0$ (Radau includes $y = 1$ but not $y = -1$).

C.3   Comparing B-splines and FEDVR

The B-splines representation and FEDVR are similar in several aspects. They are both grid methods involving high-order local polynomials. In principle, they are both more accurate than low-order methods, such as finite difference. In solving the Schrödinger equation, the Hamiltonian in both representations are banded matrices. Such banded-matrix property makes the numerical scaling in terms of the dimensionality more preferable than dense matrices. Further, for multi-dimensional Schrödinger equation, the Hamiltonian matrix quickly becomes sparse, where one could take advantage of the sparse solvers, such as `PARDISO` [88, 118].

One of the drawback for B-spline is its non-orthogonality for the basis functions, which means the overlap matrix must be evaluated and B-splines typically requires a bit more operations than that in FEDVR. In FEDVR, due to the diagonal potential matrix, it's more convenient to handle the non-separable potentials than that in B-spline. However, due to the non-continuity of the derivatives at each element boundary, the FEDVR could potentially cause some stability issue in practical implementation. Despite of the difference, the overall efficiency comparing these two methods, according to our established experience, is more or less comparable. Both methods work smoothly for the calculations performed in this dissertation.

Appendix D

Time-dependent Schrödinger equation for H_2^+ in length gauge

Starting from Eq. (3.1), the time-dependent Schrödinger equation for H_2^+ is

$$i\frac{\partial}{\partial t}\Psi(\boldsymbol{R};\boldsymbol{r},t) = \left(H_0 + \frac{e}{\mu c}\boldsymbol{\mathcal{A}}\cdot\boldsymbol{p} + \frac{e^2}{2\mu c^2}\boldsymbol{\mathcal{A}}^2\right)\Psi(\boldsymbol{R};\boldsymbol{r},t). \tag{D.1}$$

In the dipole approximation, the electric field is given by

$$\boldsymbol{\mathcal{E}}(t) = -\frac{1}{c}\frac{d\boldsymbol{\mathcal{A}}(t)}{dt}. \tag{D.2}$$

With the transformation $\Psi^L(\boldsymbol{r},t) = e^{\frac{ie}{\hbar}\boldsymbol{\mathcal{A}}(t)\cdot\boldsymbol{r}}\Psi(\boldsymbol{r},t)$, the new time-dependent Schrödinger equation for Ψ_L becomes

$$i\frac{\partial}{\partial t}\Psi^L(\boldsymbol{R};\boldsymbol{r},t) = (H_0 + W)\,\Psi^L(\boldsymbol{R};\boldsymbol{r},t), \tag{D.3}$$

which is said to be in the length gauge since the interaction term $W = e\boldsymbol{\mathcal{E}}(t)\cdot\boldsymbol{r}$ couples the electric field to the position operator. Since the dipole operator is $\boldsymbol{D} = -e\boldsymbol{r}$, the interaction is also written as $W = -\boldsymbol{\mathcal{E}}(t)\cdot\boldsymbol{D}$.

To solve Eq. D.3 in prolate spheroidal coordinates, one should follow the same formalism as in Sec. 3.1.1 except the interaction term in Eq. 3.2 now becomes

$$W = -\boldsymbol{\mathcal{E}}(t)\cdot\boldsymbol{r} = \mathcal{E}(t)z = \mathcal{E}(t)\frac{R}{2}\xi\eta, \tag{D.4}$$

where $\mathcal{E}(t) = \frac{1}{c}\frac{d\mathcal{A}(t)}{dt}$. Thus in B-splines representation, the interaction matrix in Eq. 3.14 is

evaluated as

$$
\begin{aligned}
W_{ij,i'j'} &= \int_1^\infty d\xi \int_{-1}^1 d\eta (\xi^2 - \eta^2) u_i(\xi) v_j(\eta) W u_{i'}(\xi) v_{j'}(\eta) \\
&= \int_1^\infty d\xi \int_{-1}^1 d\eta (\xi^2 - \eta^2) u_i(\xi) v_j(\eta) \mathcal{E}(t) \frac{R}{2} \xi \eta u_{i'}(\xi) v_{j'}(\eta) \\
&= \frac{R\mathcal{E}(t)}{2} \left(\int_1^\infty d\xi \ u_i \xi^3 u_{i'} \int_{-1}^1 d\eta \ v_j \eta v_{j'} - \int_1^\infty d\xi \ u_i \xi u_{i'} \int_{-1}^1 d\eta \ v_j \eta^3 v_{j'} \right) \qquad \text{(D.5)}
\end{aligned}
$$